ABSTRACT

Title of Dissertation:	TARGETING MAGNETIC NANOCARRIERS IN THE HEAD FOR DRUG DELIVERY AND BIOSENSING APPLICATIONS
	Bharath Ramaswamy, Doctorate of Philosophy, 2016
Dissertation directed by:	Professor Benjamin Shapiro, Fischell Department of Bioengineering

Magnetic nanocarriers have proven to be effective vehicles for transporting therapeutic and diagnostic agents in the body. Their main advantage is their ability to be manipulated by external magnets to direct them to specific targets in the body. In this dissertation, I study the transport, safety and efficacy of moving drug coated magnetic nanocarriers in different types of tissue. Movement of magnetic nanocarriers of sizes ranging from 100 nm to 1μm with different biocompatible coatings (Starch, PEG, Lipid and Chitosan) was quantified in different tissue types using an automated cryostat system. The safety of moving magnetic nanocarriers in live rodent brain tissue was assessed using electrophysiology, calcium imaging and immunohistochemistry. Moving magnetic nanocarriers in brain tissue did not significantly affect the firing ability of single neurons, synaptic connectivity and the overall functioning of the neuron network. As part of efficacy studies, steroid-eluting magnetic nanoparticles were targeted using external magnets to the inner ear of mice

to counter hearing loss caused by cisplatin chemotherapeutics. This targeted steroid delivery to the cochlea significantly reduced the change in hearing threshold at 32 KHz caused by cisplatin injections and protected the hair cells from significant damage. Finally, I explore the potential of spin-transfer torque nano-oscillators, which are multi-layered ferromagnetic nanocarriers, as high-resolution in vivo wireless biosensors. These nanocarriers have been shown to detect action potentials from crayfish lateral giant neurons and that the microwave magnetic signals from these devices can be detected wirelessly by near field induction.

TARGETING MAGNETIC NANOCARRIERS IN THE HEAD FOR DRUG DELIVERY AND BIOSENSING APPLICATIONS

by

Bharath Ramaswamy

Dissertation submitted to the Faculty of the Graduate School of the
University of Maryland, College Park, in partial fulfillment
of the requirements for the degree of
Doctorate of Philosophy
2016

Advisory Committee:
Professor Benjamin Shapiro, Chair
Dr. Didier Depireux
Dr. Ricardo Araneda
Dr. Yu Chen
Dr. Irving Weinberg

Dedication

அறியேன் அறிவியல் அறமொன்றும் நானறியேன்

பிரியேன் பிறைசூடி மறைமூலன் திருப்பதமே

I dedicate this work to the Jagadgurus of Kanchi and seek their blessings

Acknowledgements

This little effort of mine owes a lot to the immense support I received from both my professional and personal domains. I wholeheartedly thank my advisor, Dr.Benjamin Shapiro, for giving me this opportunity and the freedom to diversify my skills to solve multi-dimensional problems. I also acknowledge his patient guidance in shaping my perspectives on presenting data effectively. I thank… Dr.Didier Depireux for the countless discussions on the scientific impact of my work and hands-on experiment insights. There have been very few days when I haven't knocked on his door for sharing ideas or seeking help and I have always left his office with more clarity, hope and coffee. Dr.Ricardo Araneda for his valuable collaboration. He and his students (Pablo, Richard and Christian) shared so much of their time and resources and introduced me to the exciting world of neuroscience. Dr.Irving Weinberg for all the interactions and brilliant questions that ensured the depth of this work. Dr.Yu Chen for his excellent class and friendly advice throughout my time here. Dr.Edo Waks for mentoring me on the STNO project. His weekly meetings and thought provoking ideas added a whole new dimension to my thesis research. Dr.Jens Herberholz and his students (Matthew and Lucy) for their collaboration and helping me integrate two different fields of research. Dr.Ilya Krivorotov and Dr.Yu-jin Chen (University of California, Irvine) for providing the STNO devices and training me on using the devices. Dr.Andrea Apolo (NCI) for her valuable guidance and advice as part of the NCI-UMD partnership for integrative cancer research. I acknowledge the support of the lab alumni and my current lab-mates who helped with these projects:

Sandip Kulkarni, Alek Nacev, Ryan Hilaman, Pulkit Malik, Mika Shimoji, Mohammed Shukoor and Jose Algarin.

I acknowledge the financial support from NCI-UMD partnership for integrative cancer research, NSF BRAIN EAGER grant (#1450921) and Action on Hearing Loss in the United Kingdom grant.

Any effort or achievement of mine becomes insignificant before the sacrifice and patience of my parents: K Ramaswamy and R.Vijayalakshmi and grandparents: R.Krishnamoorthy and K.Pattammal. My younger sister, Vidhya, is a friend, co-researcher, cheerleader and entertainer all rolled into one and I am grateful to her belief in me more than mine. I acknowledge my cousin Sumathy for all the inspiration through her hard work and relentless balanced pursuit of ambition.

I am indebted to my friend and confidant Zachary Cummins whose perennial and creative solutions made all my problems surmountable. It is the divine will for me to cross paths with my friend and room-mate Badri Narayanan. His moral and spiritual support enabled me to overcome many personal and professional setbacks. Finally, I thank my friends: Ananth, Reza, Prateek, Vaishnavi, Bharath, Arvind, Adith, Ganesh and Harish for all the encouragement and laughter.

Table of Contents

Dedication ii
Acknowledgements iii
List of Tables vii
List of Figures viii
Chapter 1: Introduction 1
1.1 Targeted delivery systems 1
1.2 Targeted delivery to the brain: current methods and challenges 2
1.3 Targeted delivery to the inner ear: current methods and challenges 5
1.4 Magnetic targeted delivery systems 8
1.5 Controlled magnetic targeting : current approach and challenges 10
1.6 Outline for rest of this dissertation 11
Chapter 2: Quantifying magnetic nanoparticle motion in different tissues 13
2.1 Background 13
2.2 Schematic of the overall experiment 16
2.3 Experimental methods 17
2.3.1 Tissue preparation 17
2.3.2 Magnetic nanoparticles and external magnet 18
2.4 Magnetic field and force calculations 20
2.5 Properties of tested magnetic nanoparticles (MNPs) 23
2.5.1 Magnetic properties of MNPs 23
2.5.2 Size measurements of MNPs 24
2.5.3 Zeta Potential of MNP Coatings 26
2.6 Experimental Procedure 27
2.7 Post-Processing of Images 28
2.8 Results 33
2.9 Conclusions 40
Chapter 3: Movement of magnetic nanoparticles in brain tissue: mechanisms and safety 42
3.1 Background 42
3.2 Experimental methods 44
3.2.1 Characterization of magnetic nanoparticles 44
3.2.2 Uniform magnetic field using a two magnet setup 45
3.2.3 Motion experiments of MNPs in the brain tissue 46
3.2.4 Electrophysiological recordings 47
3.2.5 Calcium imaging 49
3.2.6 Immunohistochemistry 50
3.3 Results 50
3.4 Conclusions 61
Chapter 4: Magnetic steroid targeting to the inner ear to reduce cisplatin induced ototoxicity 65
4.1 Background 65
4.2 Methods 67
4.2.1 Animals 67
4.2.2 Anesthesia 68

4.2.3 Study design 68
4.2.4 Auditory brainstem response 70
4.2.5 Cytocochleogram 71
4.3 Results 72
4.4 Discussion 77
Chapter 5: Spintronic devices for potential single neuron sensing and activation 79
5.1 Wireless sensing of local currents 79
5.2 Spin transfer torque nano-oscillators for wireless local current sensing 80
5.3 Materials and methods 82
5.4 Wireless measurement of Spin transfer torque nano-oscillators 85
5.5 Powering the nano-oscillators using crayfish neurons 94
5.6 Nano-oscillators as wireless microwave rectifiers 98
Chapter 6: Conclusions 102
Intellectual contributions 107
Bibliography 109

List of Tables

Table 1: Approximate *k* values, for particles of various size, listed in units of $N/(A^2/m^3)$. The coefficient *k* relates the quantity $\| M\nabla\vec{H} \|$ shown above in Figure 3 with the actual magnetic force on the particle by $\|F| = k \| M\nabla\vec{H} \|$. 22

Table 2: Measured saturation magnetization values for the particles tested. For each particle size, the top entries are the measured value for the entire 4 µl volume sample in memu (milli-electromagnetic units), the bottom entries are the estimated per particle values. N/A (not available) is for particles types that could not be synthesized by Chemicell. 24

Table 3 : Measurements of the hydrodynamic radius of Chemicell MNPs using the DLS (dynamic light scattering) system from Photocor Instruments shows that most particles comply with the particle sizes specified by Chemicell. However, the PEG/P and lipid particles were found to have poly-dispersity and agglomeration.....26

Table 4: Zeta potential values for each particle type and coating in mV.....27

Table 5 : Tissue penetration after 45 minutes of pulling by a 0.4 Tesla magnet for various particle sizes (100 nm – 1 µm diameter), coating (chitosan, starch, lipid and PEG/P), and tissue types (rat brain, liver and kidney). Colors denote degree of penetration into the tissue, from red (low penetration) to green (high), as noted in the legend at the bottom.....35

Table 6: Tissue penetration after 45 minutes of passive transport for various particle sizes (100 nm – 1 µm diameter), coating (chitosan, starch, lipid and PEG/P), and tissue types (rat brain, liver and kidney) is shown above. Colors denote degree of penetration into the tissue, from red (low penetration) to green (high), as noted in the legend at the bottom.....35

Table 7: Coefficient of variation for N=3 experiments showing dispersion in tissue penetration after 45 minutes of pulling by a 0.4 Tesla magnet for various particle sizes (100 nm – 1 µm diameter), coating (chitosan, starch, lipid and PEG/P), and tissue types (rat brain, liver and kidney). Colors denote amount of coefficient of variation of penetration into the tissue, from red (low) to green (high), as noted in the legend at the bottom. On an average the coefficient of variation was 0.25 with a maximum of 0.78 and minimum of 0.038. 35

Table 8: Coefficient of variation for N=3 experiments showing dispersion in tissue penetration after 45 minutes of passive transport for various particle sizes (100 nm – 1 µm diameter), coating (chitosan, starch, lipid and PEG/P), and tissue types (rat brain, liver and kidney). Colors denote amount of coefficient of variation of penetration into the tissue, from red (low) to green (high), as noted in the legend at the bottom. On an average the coefficient of variation was 0.27 with a maximum of 0.5 and a minimum of 0.07. 36

Table 9 : Average chain length after 10 minutes for different applied magnetic field intensity and MNP concentration combinations in rat brain tissue.....55

Table 10 : Animal groups and schedule for our cisplatin and ear treatment study. 69

Table 11: Comparison of outer hair cell density for cochleas in naïve mice (N = 6), versus in mice that received the 3 ear treatment types (N = 6 for each group). The second row lists the percent decrease in hair cell density compared to the no cisplatin naïve group. In the magnetically treated group C, hair cell density decreased by just 9% compared to substantially greater hair loss in all the other groups. ..77

List of Figures

Figure 1: A schematic of the experimental procedure. A) Excision of an organ from a rat. B) Excised tissue. C) Magnetic nanoparticles (MNPs) were placed on top of the tissue sample in solution (as a ferrofluid). The permanent magnet was then applied at a prescribed distance below the tissue sample to create a calibrated magnetic force on the particles (see placement calibration illustrated in Figure 3). D) Resulting distribution of particles in tissue sample after 45 minutes. E) The tissue was fixed in OCT (optimal cutting temperature fluid) and then sliced and imaged using an automated cryostat and a fluorescence camera. The penetration depth of the ferrofluid was then measured and quantified by a standardized metric. 17

Figure 2: Illustration of the structure of the Chemicell particles employed in this study. A) NanoscreenMag particles contain two red fluorescent layers around the iron core but inside the particle coating. B) In the ScreenMag particles, the fluorescent dye is incorporated into a silica shell and the particle coating is outside this shell. In both cases, the fluorescent dye enabled visualization of the particle distribution inside tissue samples but is not in direct contact with the tissue. 19

Figure 3 : Measured and calculated variation of the magnetic motive force on the magnetic particles as they moved through the tissue samples. The strength of the magnetic motive force is proportional to $\| M\nabla\vec{H} \|$, which is plotted above versus particle distance from the magnet (in units A^2/m^3). The red line indicates the estimated maximum, the black is the estimated minimum, and the blue line is the average value. Based on this data, we chose the magnet size in order to, as much as possible, apply a fairly uniform motive force across the entire tissue sample. As shown, the motive force increases by at most a factor of two from the top of the tissue (6 mm away from the top of the magnet) to the bottom of the tissue (right above the magnet surface). 22

Figure 4: Particle distribution plots showing intensity vs particle hydrodynamic radius, based on DLS measurements using Photocor Instruments are shown above. The hydrodynamic radius of MNPs matches closely with the specified radius from Chemicell. Note that 300 nm Lipid and 100 nm PEG/P particles had larger size according to DLS measurements, possibly due to agglomeration. 25

Figure 5 : Particle distribution plots showing intensity vs particle hydrodynamic radius for NIST polymer particles of size 100 nm and 300 nm diameters, based on DLS measurements using Photocor Instruments are shown above. 26

Figure 6: Image processing steps: (A) A bad image resulting from random capture of an image due to noise or overlapping of a previous slice is removed. This was a rare event, but such images were removed to clean the database. On the right, a good image that is retained is shown. In the good image, the tissue region has pixel values close to zero (dark) and OCT region has pixel values up to 216 (close to white). (B) Tissue images were sometimes not correctly aligned. A typical misalignment was 20° and usually occurred due to tissue placement error (tissues had to be placed on the cryostat quickly in order to minimize temperature changes). All images were rotated until the top surface appeared horizontal. (C) Dark background was cropped until only white OCT background and dark tissue background was visible, this was done in order to facilitate image processing. (D) The image was thresholded and the bright OCT region was assigned a complete white intensity (255) so that only tissue region was considered for particle measurement. (E) In this coloring, fluorescent particles with high intensities can be seen (red corresponds to a pixel value of 216, blue corresponds to a pixel value of zero). The sum of all intensities across a single row represents the total number of particles at that depth. The resulting pink curve shows the distribution of particles with depth. The centroid of this pink curve quantifies the depth of penetration of particles into the tissue sample. 32

Figure 7 : Magnetic transport of particles versus diffusion alone. The images show fluorescence distribution in three types of particle-tissue pairs for passive and magnetic transport. In each case, dc is

centroidal distance that particles penetrate in tissue (dc is defined in Sec. 0, step H). Chitosan 100 nm particles (A) passively diffusing through liver tissue demonstrated limited movement (dc = 2.6 mm) versus (B) moved substantially when pulled with a magnet (dc = 5.3 mm). PEG/P 100 nm particles (C) passively diffused through a section of kidney showing some spreading and diffusion (dc= 2.6 mm) versus (D) showed some small additional movement when pulled with a magnet (dc = 3.0 mm). Lipid 300 nm particles (E) showed limited diffusion in brain tissue (dc = 2.5 mm) versus (F) substantial magnetic drift (dc = 5 mm).....34

Figure 8 : Tissue penetration after 45 minutes of pulling by a 0.4 Tesla magnet for various particle sizes (100 nm to 1 μm diameter), with various coating (chitosan, starch, lipid and PEG/P), in different tissue types (rat brain, liver and kidney). Colors denote the type of coating, the shape of the prism denotes the tissue type, and the height of prisms shows the degree of penetration into that tissue. The vertical bar with black disk above it denotes the standard deviation of the measurement. Particles types that were not available from Chemicell are marked by the crossed-out symbols.....36

Figure 9: Tissue penetration after 45 minutes of passive diffusion and pulling by a 0.4 T magnet for all tested particle sizes (100 nm, 300 nm, 500 nm and 1 μm) and all available coatings (starch represented as blue, chitosan as green, lipid as yellow and PEG/P as red prisms). Penetration depth is represented by the height of each prism. The shape of the prisms represents movement through specific tissue type: square prisms denote movement through liver, triangular prisms denote kidney and cylinders denote brain. The color of the substrate (the base on which the prisms lie) denotes the presence of a pulling magnet (dark gray substrate) versus the absence of a magnet (diffusion only, light substrate).....38

Figure 10 : (A) The distribution of hydrodynamic diameter of the MNPs measured using dynamic light scattering. (B) The magnetization versus magnetic field intensity profile of MNPs measured using vibrating sample magnetometry. 51

Figure 11: The deviation of magnetic field intensity from the mean value in the region between the two magnets. The two magnet-system produces a uniform field with less than 1.0% variation in the region occupied by the tissue (represented by yellow dotted lines). 52

Figure 12: (A) The diagram of two-magnet setup used to study movement of MNPs in brain tissue. The tissue loaded with MNPs was mounted and visualized under a fluorescent microscope after exposing it to the uniform magnetic field (B) An illustration of how MNPs behave in brain tissue with and without an applied uniform magnetic field. The MNPs diffuse in different directions (blue arrows) in the absence of a uniform magnetic field (left, top). After the introduction of the magnetic field, the MNPs move towards each other due to an overlap of induced magnetic fields of influence (green circles). As a result, the MNPs form chains as they move towards each other and longer chains have a larger field of influence which recruits additional particles to the chain (bottom). (C) Chaining of MNPs experimentally observed in mouse brain tissue (pre-frontal cortex region) in the presence of a uniform magnetic field. The MNP chains (orange) and single MNPs are enclosed by white ovals and white dotted circles respectively. The dendrites (green) in the tissue are indicated by white arrows. ...54

Figure 13: Functional health of brain tissue after MNP motion. (A) Recording from a mitral cell in the olfactory bulb after the slices treated with MNPs were subjected to a magnetic field. The recording electrode contained the fluorescent dye Alexa-488 (green), which diffuses into the neuron during the recording. The MNPs contained a fluorophore Texas-Red (red). Note this is a total summed two wavelength images (B). Current-clamp recordings in mitral cells before (red) and after magnet induced MNP movement (blue). Increasing depolarizing current pulses (not shown) elicited action potentials in both control and treated neurons. (C) In the range of depolarizing current used, the frequency of neuronal firing increased linearly and it was comparable for different constant current stimuli before (black) and after MNP motion (red).....56

Figure 14: Synaptic connectivity in the olfactory bulb after MNP motion (A) Recording from a mitral cell showing the spontaneous occurrence of GABA IPSCs after MNP motion in brain slices. Top, application of noradrenaline (NA, 10 µM, 3 min) produced a long lasting increase in sIPSC frequency in this cell. Bottom, select traces from above, in an expanded time scale, showing sIPSC before (left) and after NA (right). (B) NA significantly increased the sIPSC frequency; baseline, 2.56 ± 0.82 Hz, NA, 7.39 ± 2.34 Hz (*, $p<0.003$; $n = 5$). The observed increase in sIPSC frequency caused by NA after MNP motion is similar to the trend observed previously by Zimnik et al. [190] 57

Figure 15: Calcium imaging recording in brain slices after MNP motion. (A) Experimental setup used for the calcium imaging experiments. After loading the calcium dye, MNPs are placed on the slice and subjected to a magnetic field. (B) Fluorescence image showing a network of functionally active neurons in a brain slice loaded with the calcium dye Fluo-4 AM (white) and MNPs (red), after exposing the slice loaded with MNPs to a uniform magnetic field. Dotted colored circles represent the neurons used for quantification of fluorescence changes shown on the right. (C) Optical fluorescence recordings of the selected cells shown in B. Images were taken at a rate of 1 Hz FPS. Application of the excitatory neurotransmitter, glutamate (100 µM, 45 seconds) resulted in a large, and reversible, increase in intracellular calcium levels. The color of each plot corresponds to cells indicated by the colored dotted circles in (B). 59

Figure 16: Confocal microscopy images of the granular cell layer in the main olfactory bulb from ChAT-Tau-GFP mice, after immunostaining for GFP. In control conditions (left) the slices show abundant distribution of GFP labelled fibers, corresponding to the axonal processes of cholinergic neurons. The pattern of distribution of axonal fibers was not affected in slices treated with MNPs without application of the magnetic field (middle) or after the MNPs exhibited motion into chains under an applied uniform magnetic field (right).....60

Figure 17: Comparison of hearing loss between the three animal groups for the injected left ears and corresponding untreated right ears ($N = 6$ for each group). Percent hearing loss at each frequency, per group, is shown. A) Treated ears that received magnetic nanoparticles showed significantly less hearing loss (group A bars) compared to the intra-tympanic methyl-prednisolone group (group B bars, $p^{**} < 0.05$) and the saline control group (group C bars, $p^{**} < 0.05$), especially at high frequency of 32 KHz. Hearing loss remained similar at high frequency across all groups for untreated ears. B) A sample ABR trace containing the waves I and II (dotted black box) at 16 KHz has been shown to demonstrate threshold measurement (note that positive voltage is up, the convention for animal ABRs). The threshold for this animal is at 34 dB beyond which the waves I and II are completely attenuated. 74

Figure 18: Sample cytocochleograms of the basal cochlear region of different groups. The outer hair cells were stained for actin with Alexa Fluor 488 Phalloidin (green) and the various cell nuclei were stained using DAPI counterstain (blue). A) Left ear from a naïve animal that did not receive any cisplatin treatment or otoprotection. For animals that were administered cisplatin: B) Left ear that received saline; C) Left ear that received intra-tympanic methyl-prednisolone; and D) Left ear that received magnetic steroid delivery. The images of the DAPI stained nuclei for all the groups have been shown in the image insets of A), B), C) and D) correspondingly.....76

Figure 19: A) Schematic of the nanopillar spin torque oscillator device. The numbers in parentheses are the layer thicknesses in units of nanometers. B) A schematic of the microwave circuit used for direct electrical measurement from the device and wireless measurement of the microwave signal emission from spin transfer torque nano-oscillator. C) The microprobe and the connection pads along with the spin torque nano-oscillator forming an effective inductive coupler. D) The micro-fabricated receiving coil patterned on SiO_2 substrate.....85

Figure 20: A) The power spectral density of the direct electrical signal measured from the spin transfer torque nano-oscillator at 0.15 T. B) The power spectral density of the wireless signal measured from the receiving coil at 0.15 T. The transmission coefficient measured between the device and coil using a

network analyzer for the same frequency range (inset) C) The integrated power obtained in measurements versus bias current A) and B). 89

Figure 21: The wireless signal received from the spin transfer torque nano oscillator as a function of distance between the STNO and the receiving coil for a detection current I_{DC} = 700μA.....90

Figure 22: The schematic diagram for powering the spin transfer torque nano-oscillators using the neuronal action potentials from a crayfish neuron. 95

Figure 23: A) The recordings from the crayfish neurons with the application of a voltage stimulus (black) and without a stimulus (red). The neuronal action potential peaks can be observed in the recordings with stimulus. B) The response of the spin transfer torque nano-oscillators for the neuronal current input. The nano-oscillator responded to the action potential spikes with its corresponding power spikes at its working frequency. 97

Figure 24: The schematic diagram of the circuit used for wireless alternate current stimulation of the spin transfer torque nano-oscillator and measuring the rectified DC voltage produced in it.....99

Figure 25: A) Dc voltage produced in the spin transfer torque nano-oscillator for different wirelessly transmitted input ac signals. The nano-oscillator produced DC voltage peaks for specific input frequencies (for e.g. 3.8 GHz) which can be modulated using the external magnetic field. B) The DC voltage produced for different distances between the transmission coil and the spin transfer torque nano-oscillator at an input AC frequency of 3.8 GHz. 101

Chapter 1: Introduction

1.1 Targeted delivery systems

Targeted delivery systems can be used to improve delivery of therapeutics or contrast agents to achieve a two-fold benefit: increased concentration of drugs in the disease locations and reduced release to non-specific locations, thereby reducing the associated side effects[1]. A typical targeted delivery system consists of an active carrier attached to or encapsulating the therapeutic or diagnostic payload. The carriers include liposomes[2,3], nanoparticles[4,5], micro-organisms[6], polymer beads[5,7,8], peptides[9] and other ligands[10]. The therapeutics delivered using these carriers includes steroids [11–13], proteins[14–17], chemotherapy[18–20], stem cells[21–23] and genes [24–26]. The mechanism for delivery can be passive diffusion aided by the flow of body fluids [2,3,11,24,25] or through active methods involving electromagnetic[27–31] or acoustic fields[15,32–34]. The combination of carrier, drug and delivery mechanism is chosen based on depth of targeting required, time profile of drug release, physiological factors, the therapeutic-carrier binding chemistry and safety. This thesis focuses on different aspects of targeting and utilizing magnetic nanocarriers using external magnetic fields for drug delivery and biosensing applications in the brain and the inner ear.

1.2 Targeted delivery to the brain: current methods and challenges

Conventional therapeutics in the brain is limited by two main anatomical barriers: blood brain barrier and the extracellular space[35,36]. The blood brain barrier consists of a layer of endothelial cells forming tight junctions supported by interactions with brain pericytes, astrocytes and neurons[37]. It regulates the transport of substances between the blood stream and the central nervous system and helps in maintenance of neuronal microenvironment, tissue homeostasis, blood cell activation and migration and vascularization of normal neoplastic tissues[36,38]. These tight junctions physically restrict the movement of microbial, cellular or metabolic substances from the blood stream to the central nervous system. Many studies showed that more than 90% of small molecules and almost all large molecules are unable to cross the blood brain barrier without external force[35,38–40]. A detailed study of about 7000 common pharmaceuticals revealed that very few had the ability to cross the blood brain barrier[39]. In addition to the size restrictions imposed, there are active transporters in the blood brain barrier that increase or reduce the transport of permissible substances thereby adding an additional layer of complexity[41]. The barrier is altered during disease processes such as tumors, inflammation and infection which results in it allowing some substances to be transported through[42–44]. In spite of the blood brain barrier being compromised during such processes, the permeability of the blood brain barrier changes heterogeneously and makes it difficult for systemic injections of therapeutics to reach the required locations uniformly.

While the blood brain barrier is thought of one the most prominent barriers to targeted delivery, extracellular space where most of the therapeutic and diagnostic substances travel in brain tissue after extravasation, has posed similar challenges of poor distribution. The extracellular space in the brain consists of lipids, polysaccharides and proteins resulting in regions of different electrostatic and surface properties. The two main modes of transport of substances in the extracellular space are diffusion and convection. Diffusion is the random movement of substances due to a concentration gradient. Convection is a directional movement of substances caused due to pressure gradients induced by external or internal sources[45,46]. Similar to the blood brain barrier, the properties of the extracellular space such volume and tortuosity are also affected by diseases such as tumors in the brain [47]. These physical changes result in anisotropies in their structure affecting the reachability of therapeutic substances in the brain. In addition, diseases such as tumors in the brain also alter the interstitial pressure gradients in the tissue and affect convectional transport [47]. This adds specific constraints to the charge, hydrophobicity and size of the substances used for cell specific targeting in the brain. The complex properties of the extracellular space necessitate the use of active targeting methods to move therapeutic agents from one region to another. Therefore, an effective combination of therapeutic agents and targeting mechanism should aid penetration of the blood brain barrier and also produce a sufficient distribution in the brain tissue through the extracellular space.

Nanoparticles of various sizes and coatings have proven effective for delivering therapeutic and diagnostic agents for local and system delivery in the brain [48–52].

Drugs or contrast agents can be either chemically bound or adsorbed to these nanoparticles. These nanoparticle based delivery systems provide sufficient flexibility in engineering appropriate physical and surface properties, drug loading and release kinetics to match the disease progress in the target locations[36,48].These delivery systems also open up the possibility of combining multiple therapeutic agents or therapeutic agents with imaging agents to perform image guided therapeutics. Several drug delivery systems involving lipid [48], chitosan [53,54], and iron oxide nanoparticles [49,55,56] have been shown effective in the brain. The uptake of these nanoparticles is influenced by various physicochemical properties such as particle size, shape and surface charge. The main challenges faced by these nanoparticle based systems in the brain are rapid clearance by the reticuloendothelial system especially when used systemically. In spite of using surface coatings that improve endocytosis of these drug-nanoparticle combinations to the brain, they require high volume of injections to improve bioavailability. This emphasizes the use of an effective targeting mechanism to improve the efficiency of these nanoparticle based delivery systems.

Systemic delivery in the brain is commonly divided into two main categories: Intravenous and Intra-arterial delivery. Intravenous or Intra-arterial route of drug administration are used commonly and has the advantage of direct delivery to the circulation [57–59]. In spite of good access to most parts of the brain, these delivery methods faces the challenges of low retention time due to rapid clearance, non-specific binding to the plasma proteins and inability to cross the blood brain barrier.

New approaches to delivery have been investigated to directly deliver drugs or imaging agents into cerebrospinal fluid or the parenchymal space thereby reducing the drug concentration in regions unrelated to the target. These approaches include intracerebral delivery using catheters or intracerebral implants directly into parenchymal space [60], intraventricular or transcranial delivery into cerebral ventricle or intrathecal delivery [61] into cisterna magna of brain. In spite of their advantages they require an active targeting method to redistribute the concentration of carriers in the target tissue to avoid harmful effects such as astrogliatic reaction[62] and ensure sustained drug release in the parenchyma. Intranasal delivery[40,63,64] of drug loaded nanocarriers has been used to directly reach the central nervous system via olfactory neurons. Though this method is a viable alternative to crossing the blood brain barrier, it requires an external active targeting mechanism to translate it for larger regions in the brain.

1.3 Targeted delivery to the inner ear: current methods and challenges

Inner ear diseases such as sudden sensorineural hearing loss (SSNHL), tinnitus (ringing in the ears) and Ménière's diseases affect 5000-20,000 [65], 15 million [66] and 615,000 [67] patients annually. The conventional method of treating these inner ear disorders have been through oral or intravenous administration of drugs. For example, high dose oral and intravenous administrations of steroids have been used for SSNHL to reduce inflammation in the inner ear that is thought to be the cause of SSNHL[68]. These treatments have produced unreliable outcomes because of many challenges. Only 10^{-6} of general blood perfused passes through the inner ear because the cochlea,

similar to the brain, is behind a blood-labyrinth barrier characterized by the vessels that bring blood to the inner ear with walls that are largely impermeable to drugs [69]. In addition, the high dose of oral or intravenous steroids is known to cause substantial side effects in patients[70,71]. Thus there is a need for a topical delivery mechanism to reach the inner ear (especially cochlea) from the middle ear to improve the treatment of diseases such as SSNHL.

Among the topical delivery methods available for the inner ear diseases, there are no minimally invasive techniques. Although the middle ear is reachable by injections through the ear canal to topically target drugs to the cochlea, it requires facial-recess surgery under anesthesia[72]. To instead directly reach the inner ear via ear canal injections, it would require the injections to first cross the tympanic membrane and then the round window or oval window membranes. However, there is no line of sight from the ear canal to the window membranes for these injections in human patients. Moreover, the oval window membrane is covered by the third ossicle and reduces the access. These factors make any topical injections straight through the window membranes exposed to the risk of acoustic or vestibular traumas.

The standard of care for sudden sensorineural hearing loss involves injecting s large dose of drugs into the middle ear and waiting for the drugs to passively diffuse into the cochlea through the window membranes, mainly the round window membrane. These trans-tympanic injections can be performed using a syringe, through a tube (tympanostomy) or via a microcatheter[73] and the tympanic membrane heals after

these procedures [74]. Subsequent diffusion of the drugs from the middle ear to the cochlea is limited by two factors: the size of the window membranes and the presence of the eustachian tube which drains out the drugs in the middle ear every time the patient swallows[75,76]. This results in a steep drug concentration gradient inside the cochlea with too high concentrations at the base of the cochlea and too-low concentrations in the other cochlear turns[77]. Anatomical variations caused due to extraneous or false membranes, fibrous tissues and fatty plugs alter the pathway of drugs from the delivery site to the round window membrane[78]. Despite the lack of consistent success in treating inner ear disorders, intratympanic drug administration is common.

Many approaches have been used previously to prolong the exposure of the round window membrane to high drug concentrations, to increase delivery to the inner ear. These include use of microcatheters [73], gels [79,80] and nanoparticle formulations[81]. A 1mm x 9 mm polyvinyl acetate wick was applied through a tube in the tympanic membrane, facing the round window membrane to treat sudden sensorineural hearing loss[79]. It was removed from the market due to potential long term hearing loss and technical administration difficulties[82,83]. Delivery of medications to the cochlea using a microcatheter placed on the round window membrane was used to treat tinnitus associated with Ménière's disease [73]. This method resulted in catheter dislocations, granuloma formation in the middle ear and permanent tympanic membrane perforations [84]. A hydrogel system has been used for controlled release of drugs to the inner ear through the use of triggering mechanisms such as temperature, pressure or

pH [79,85,86] .This system is easy to formulate since it is a dissolvable matrix that can be combined with different drugs but requires an accurate placement on the round window niche to be effective and has the danger of overfilling the middle ear (which can lead to loss of hearing) [79]. Osmotic pumps have been used to treat hearing loss from noise trauma and cisplatin chemotherapy by delivering steroids, growth factors and compounds such as D-JNKI-1, a peptide inhibitor of the apoptotic pathway and BN82270, a peroxidation inhibitor to reduce free radicals in the cochlea. These pumps help in accurately control the dosage but require risky surgery to implant them in the cochlea [78].

1.4 Magnetic targeted delivery systems

Magnetic targeted delivery offers a minimally invasive potential solution to focus therapeutics and diagnostic agents in different regions in the body. In these delivery systems, magnetic nanocarriers (typically iron oxide nanoparticles) are attached to the therapeutic agents and can be directed using external magnetic fields. This physical focusing of nanocarriers loaded with therapeutics improves the efficacy of treatments by placing the drug precisely in disease locations with extended release, reducing the systemic concentration of drugs and limiting the associated side effects and preventing rapid clearance of therapeutics by the body before its protective action in the disease locations.

Magnetic targeting systems are desirable when compared to ultrasound, optical or electrical fields because they can penetrate deep into the body without causing any

physiological side effects [87]. In magnetic resonance imaging (MRI), which is very commonly used, very high magnetic fields are used in the body and have been shown to be safe. Magnetic core of the nanocarriers used in these targeting systems typically consists of either magnetite (Fe_3O_4) or maghemite (Fe_2O_3) embedded in a polymer and coated with a biocompatible coating such as chitosan, starch or polyethylene glycol (PEG). These nanocarriers can be controlled in size and are usually injected into an animal or a patient in the form of emulsions in water. Apart from drugs such as chemotherapy and steroids [88,89], these magnetic nanocarriers have been used to deliver immune cells [90], stem cells [91], peptides [92] and genes [93] for different applications in various organ systems . An alternate mode of application with these magnetic nanocarriers which involves producing heat by exposing them to a time varying magnetic field has been proposed as a mechanism to destroy tumor cells [94].

The magnetic field gradients that have been typically used in drug delivery experiments vary from 0.03 T/m to 100 T/m based on ease of use and desired depth of targeting [95,96]. Neodymium-iron-boron ($Nd_{12}Fe_{14}B$) permanent magnets can be commonly found up to field strengths of about 1.5 T compared to huge MRI electromagnets of field strengths 1-4.7 T [97,98]. In one of the first human clinical trials, Lubbe et al injected ferrofluid containing 100 nm particles coated with doxorubicin and concentrated them in an inoperable shallow facial tumor using 0.2-0.8 T permanent magnets [99]. Similar experiments in different animal models have produced a targeting depth of close to 12 cm using 500 nm – 5 μm nanoparticles and 0.5 T permanent magnets [100]. Since the human body is a complex environment with various physical and chemical factors varying from person to person, the appropriate size of

magnetic nanocarriers to be used and the corresponding magnetic force required to direct them varies for different cases. Thus there is a need for controlled targeting of magnetic nanocarriers through dynamic shaping of magnetic field gradients as they move through the physiological barriers in the body.

1.5 Controlled magnetic targeting : current approach and challenges

Precise control of magnetic objects using external fields has been demonstrated in animals and humans [101,102]. Magnetic control to guide catheters with magnetic tips has been used to treat cardiac arrhythmias and perform other cardiovascular procedures [103]. Systems to magnetically manipulate microrobots and other devices for eye, gut, cardiovascular and lung surgery have been tested in pigs and chicken embryos[104–106]. Conventional MRI machines have been thought of as actuation systems for precise manipulation of magnetic objects[107] . But the MRI machines produce a uniform magnetic field and need to be substantially modified to produce a magnetic field gradient which is required to produce magnetic force. The control algorithms used in manipulating single magnetic objects include simple proportional-integral-differential (PID) control [108], point wise optimal control [109], least-squares inversion [110] and model predictive control [111]. Manipulation of a fluid of nanoparticles is more difficult than controlling a single object due to additional constraints caused by fluid flow, particle-particle interaction and surface tension. In order to implement a closed loop controlled targeting of magnetic nanocarriers in the body, there is a need for minimum models that can predict their motion in different physical regions in the body (blood vessels, soft tissues, connective tissue, muscles). These models can help

determine the right parameters that can be varied over a range of physiological conditions and in turn help in designing the optimal nanocarriers and magnet systems. Our group has previously studied the movement of ferromagnetic nanoparticles in and around the major blood vessels. This in-silico study has categorized the motion of magnetic nanoparticles after intravascular injections for all physiological conditions – from small to large blood vessels and across all particle sizes and magnet strengths [112]. These studies have to be extended to different tissues into which the nanocarriers extravasate and travel to reach disease targets. Another important challenge in closed loop implementation of magnetic targeted delivery is high resolution imaging to provide accurate feedback in complex environments. Many groups have investigated the use of fluorescent tags attached to the nanocarriers to track them optically. These cannot be visualized in-vivo due to absorption by various tissues in the body. Imaging iron oxide and gadolinium based nanoparticles have been shown using MRI systems [50,113]. Since these particles produce a negative contrast in MRI, these images are not of high resolution. Moreover the speed of MRI also poses a challenge to dynamically manipulate magnetic nanocarriers effectively in the body. This dissertation aims to address these challenges in high resolution imaging of magnetic nanoparticles and developing reliable and safe nanoparticle transport models in different tissue targets.

1.6 Outline for rest of this dissertation

The rest of this dissertation discusses the implementation and impact of targeting and sensing two different types of magnetic nanocarriers: drug coated magnetic nanoparticles and spin transfer torque nano-oscillators for applications in drug

delivery in the brain and inner ear and sensing currents from a single neuron respectively. Chapter 2 details the implementation of a method to quantify the motion of magnetic nanoparticles in different tissues and determines the influence of physicochemical properties of the nanoparticles and the tissues in nanoparticle motion. Chapter 3 studies the mechanism of magnetic nanoparticle motion in brain tissue and assesses the safety of moving magnetic nanocarriers in the brain using electrophysiological recordings, calcium imaging and immunohistochemistry. Chapter 4 focuses on applying the magnetic drug delivery method to deliver steroids to the inner ear in mice models. This minimally invasive steroid delivery method has been shown to reduce cisplatin induced hearing loss in mice. The impact of the treatment has been analyzed using auditory brainstem response assays and post-mortem cytocochleograms. Chapter 5 proposes the use of spin transfer nano-oscillators, which are multilayered ferromagnetic nano-devices, to sense local currents in the brain and transmit them wirelessly with a potential for functional neuroimaging with a single cell resolution. The chapter covers the experimental details of wireless measurement from the nano-devices and triggering them using neuronal action potentials from crayfish lateral giant neurons. Chapter 6 summarizes the conclusions presented in this dissertation, discusses their importance, and proposes future scope of these projects. Finally, the intellectual contributions of the author are provided relative to the group of collaborators.

Chapter 2: Quantifying magnetic nanoparticle motion in different tissues

This work originally appeared in [114]

2.1 Background

In the fields of magnetic drug targeting[28], hyperthermia[94], and magnetic resonance imaging [115,116] there is a need to be able to transport magnetic nanoparticles (MNPs) to desired tissue locations. How MNPs move *in-vivo* depends on their properties, the properties of the surrounding biological milieu, and on the strength of the applied magnetic field gradient. In prior work, we analyzed how the transport of MNPs in blood vessels depends on particle constitution, size, the velocity and profile of blood flow in vessels, and the strength of the applied magnetic field gradient[112,117]. In this article, we begin to address the second half of the question: how MNPs move through the tissue between blood vessels. By measuring how particle motion in freshly excised tissue depends on particle size, coating, tissue type, and the applied magnetic field gradient, we hope to provide researchers with tools for better understanding that motion in order to help select MNP designs to improve therapy[27–29,87,118–121] and diagnosis[27,116,122–125].

Substantial evidence indicates that particle characteristics (size, surface chemistry, volume of magnetic content) influence their motion through biological media such as mucus[126], liquids and gels[127], and brain tissue[10,11]. In mucus[126], modifying particle size and coating led to 10 fold and 10,000 fold changes in diffusion respectively. In liquids and gels[127], among a set of particles (10 nm and 50 nm size, uncoated,

polystyrene coated and dextran coated), only 50 nm dextran coated particles moved, and movement in glycerol was 20 times faster than in collagen gel. In brain tissue, the width of extracellular spaces (30-64 nm) precludes liposomes above 100 nm from penetrating the brain during convection enhanced delivery[128–130]. Particle steric coating (e.g. polyethylene glycol or PEG) and charge also influence binding to cells and thereby limit or improve diffusion in brain tissue[128,129,131].

To our best knowledge, as yet there have been no experimental studies that have quantified the ability of magnetic forces to transport different types of MNPs through different tissue types. Prior research has included the study of MNP motion in liquids[30,127]and gels[127] and indicated that MNP penetration depends strongly on the characteristics of the particles and the surrounding medium. Motion of magnetic beads within *in vitro* cultured cells (fibroblasts and actins) has been studied for measurement of cytoplasmic viscosity and motility [132]; however, the focus was on rheology within cells rather than passage of MNPs through tissue. Motion of particles in cells was also studied in Zhang et al.[133] to create rotation and apoptosis of cells. MNP penetration in ex-vivo human skin was studied qualitatively in Baroli et al.[134] but the study employed passive diffusion for transport.

Several forces are thought to influence the motion of MNPs in tissue[135]. The magnetic force (F_{MAG}) is the force applied by the external magnet on the particles. Inter-particle interaction forces[136] act on magnetized particles and can lead to their agglomeration[136–138]. Tissue resistance (F_{TR}) is likely composed of a viscous drag

force (F_D) and the binding force (F_S) due to the adhesion between particle surface coatings and the tissue microenvironment[139–144]. The contribution of these component forces and the interplay between them is complex and has been a challenge to address. As far as we know, there are no accepted mathematical theories available for adequately capturing these complexities. Hence, in this article we focus on experimentally measuring particle movement in tissue samples.

We present a simple experimental technique to quantify the motion of magnetic particles through tissue. To arrive at these first results to understand and quantify particle motion in tissue under the influence of magnetic fields, we used freshly excised tissue (ex-vivo experiments). Even though we took sensible precautions to ensure that our excised tissue samples remained as close in their properties to living tissue as possible (excision time was less than two hours, tissue was preserved in a cool environment and was stored in phosphate buffer solution), we note that our collected results may still differ from in-vivo particle behavior because even with optimal procedures excised tissue is known to differ from live tissue[145–147]. In our approach, fluorescent MNPs were placed on top of freshly excised tissue samples and a magnetic field was applied by placing a magnet under the tissue. After a set time, the tissue was fixed (flash-frozen), sliced, imaged using a fluorescent microscope and particle movement was then quantified by processing the three-dimensional volume of particles from stacked images using standardized quantitative metrics. Experiments conducted with and without a magnetic field distinguished the effect of diffusion versus magnetic drift. Our results indicate how particle properties and tissue types can affect particle motion, under what circumstances the magnetic field is most effective

at moving particles in tissue, and which particle types among those tested should be selected for efficient magnetic transport.

2.2 Schematic of the overall experiment

We developed and implemented a methodology to measure the rate of MNP movement in fresh tissue. To do so, we placed fluorescent MNPs on top of freshly excised rat tissue and applied a high magnetic field gradient by placing a permanent magnet at a precise distance underneath the MNPs below the tissue. This magnet moved the MNPs into and partway through the tissue. The tissue was then fixed and a 3-dimensional cryostat imaging system similar to Shen et al[148] sliced the tissues and imaged the distribution of particles in the tissue samples. The acquired imaged data was pruned and the images were stacked into a 3-dimensional volume. Standardized metrics representing the degree of particle penetration into tissue samples were used to quantitatively assess the depth of particle penetration into the tissue. Then penetration depth was tabulated to compare the effects of particle size (hydrodynamic diameter), surface coating, tissue type (brain, liver, kidney), and magnetic field gradient on MNP motion in tissue. A flow diagram of this process is shown in Figure 1 below.

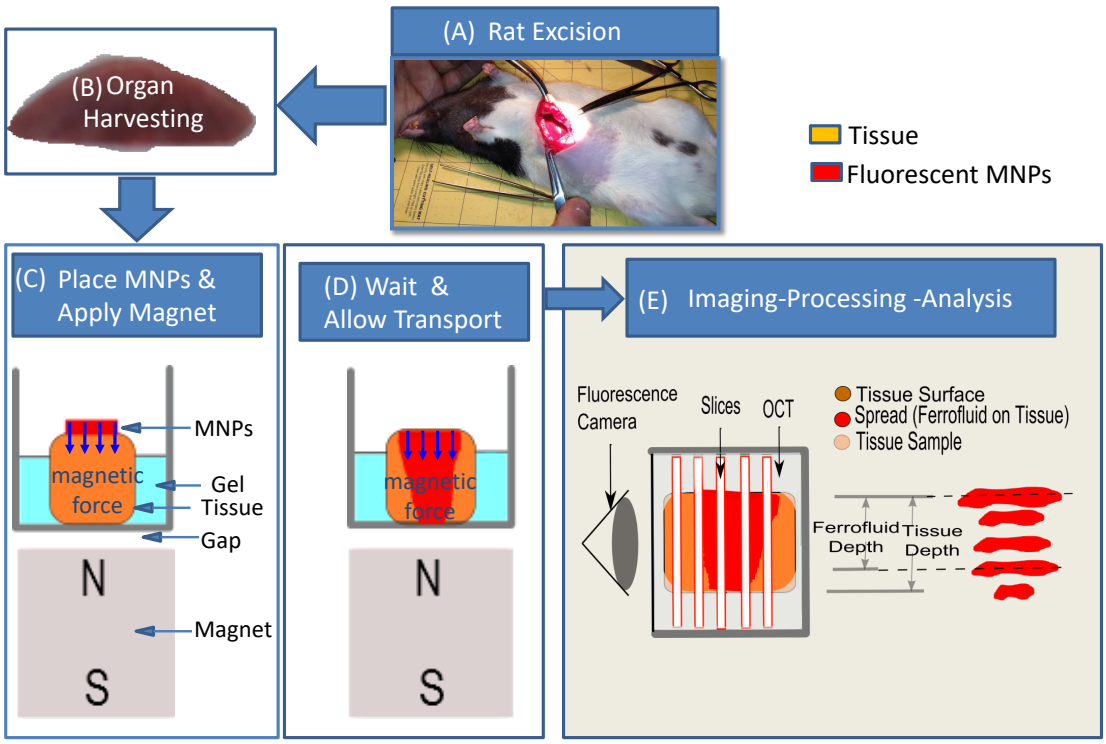

Figure 1: A schematic of the experimental procedure. A) Excision of an organ from a rat. B) Excised tissue. C) Magnetic nanoparticles (MNPs) were placed on top of the tissue sample in solution (as a ferrofluid). The permanent magnet was then applied at a prescribed distance below the tissue sample to create a calibrated magnetic force on the particles (see placement calibration illustrated in Figure 3). D) Resulting distribution of particles in tissue sample after 45 minutes. E) The tissue was fixed in OCT (optimal cutting temperature fluid) and then sliced and imaged using an automated cryostat and a fluorescence camera. The penetration depth of the ferrofluid was then measured and quantified by a standardized metric.

2.3 Experimental methods

2.3.1 Tissue preparation

Long Evans Rats (obtained from Charles River) were used to obtain the tissue samples. The rats were anesthetized using Isofluorane gas and then sacrificed. All surgical and experimental procedures were approved by the University of Maryland Animal Care and Use Committee and were in accordance with NIH Guidelines on the care and use of laboratory animals.

Freshly excised organs were stored in phosphate buffer (PBS) at 4°C for about 1-2 hours until the experiments. Tissue sections of 4-6 mm thickness were prepared, embedded in liquefied gelatin in a 10 mm petri dish, and then cooled at 4 degrees until the tissue was immobilized.

2.3.2 Magnetic nanoparticles and external magnet

A variety of fluorescent magnetic nanoparticles (MNPs) purchased from Chemicell GmbH were used for our experiments. In this first study, we elected to use particles from Chemicell because we have used Chemicell particles for many years, and are familiar with the handling, properties and behaviors of these particles. Four available sizes (100 nm, 300 nm, 500 nm and 1 μm) and four coatings (Chitosan, Starch, Lipid and PEG/P) were selected. Chemicell GmbH provided us with two types of particles. A) NanoscreenMag particles with hydrodynamic size < 300 nm and with the fluorescent dye outside the iron core beneath the external coating; B) ScreenMag (or SiMag) particles with hydrodynamic size between 500 nm - 1 μm where the fluorescent dye is incorporated in a silica shell around the core and the particle coating is around the silica shell. All particles contained a fluorescent red dye (lipophilic fluorescence dye Lumigen-Red for nanoscreenMAG and nil-blue for screenMAG) for easy visualization of the distribution of the particles in tissue. These two types of particles are illustrated in Figure 2. In our experiments, the dye was excited at 578 nm and emission was measured at 613 nm to quantify the distribution of particles in the tissue samples. Chemicell was unable to synthesize starch particles > 500 nm, lipid particles > 300 nm and PEG/P particles > 200 nm due to their higher

molecular weight (these particles did not remain stable at the larger sizes). Our tissue experiments were conducted for those fluorescent particles that were available from Chemicell.

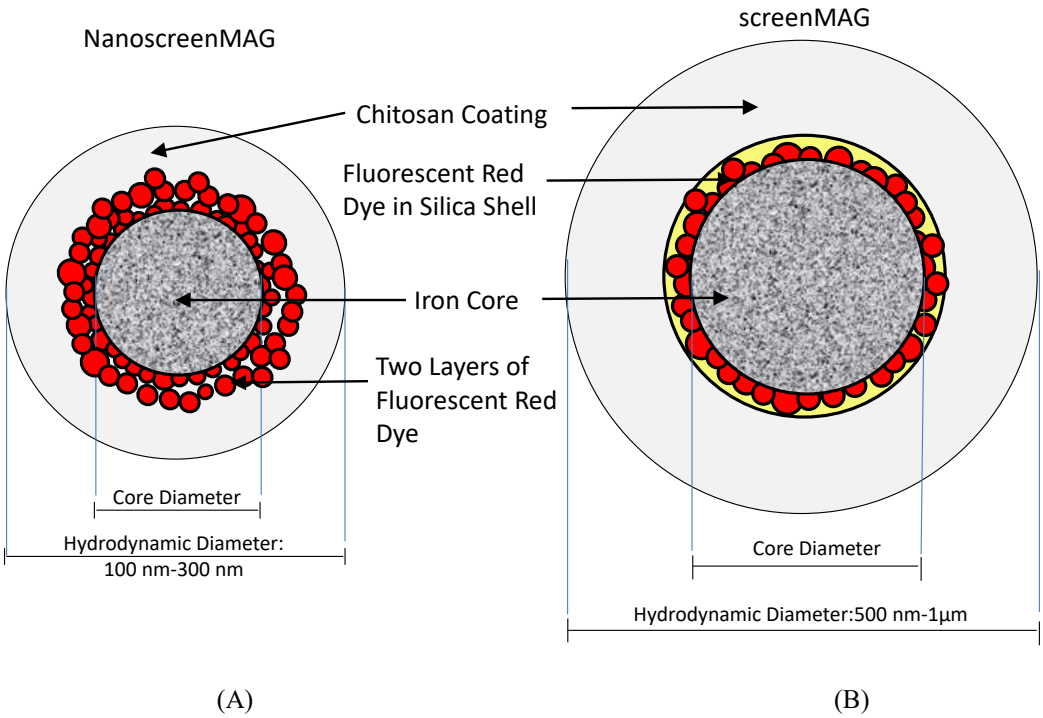

Figure 2: Illustration of the structure of the Chemicell particles employed in this study. A) NanoscreenMag particles contain two red fluorescent layers around the iron core but inside the particle coating. B) In the ScreenMag particles, the fluorescent dye is incorporated into a silica shell and the particle coating is outside this shell. In both cases, the fluorescent dye enabled visualization of the particle distribution inside tissue samples but is not in direct contact with the tissue.

To keep the experimental setup simple and compact, we employed small NdFeB, grade N42, permanent bar magnets with Nickel-Copper-Nickel triple layer coated, size 1" x 1" x 2", magnetized through the 2 inch length with poles on 1 x1 inch surfaces (from Applied Magnets Inc.). These magnets had a high field strength (surface field strength of ~0.4 T and core strength of 1.5 T), which created a strong

maximum magnetic field gradient (~ 30 T/m). The magnets were placed below the tissue blocks as shown in Figure 1 in order to effectively pull particles towards the magnet. We found that these magnets applied a sufficient magnetic field gradient to effectively move the different types of MNPs through the tissue samples. The magnets were small enough to permit a convenient experimental setup but big enough to enable careful calibration of the magnetic forces applied to the particles (discussed next).

2.4 Magnetic field and force calculations

The magnetic force we applied on the MNPs was calibrated by measuring the magnetic field and gradient around each permanent magnet. A single ferromagnetic particle will experience a magnetic force $\vec{F} = k\,M\,[D\vec{H} / D\vec{x}] = k\,\vec{M}\,\nabla\vec{H}$ [31,87,112,149,150] where $\vec{H}$ is the applied magnetic field, $\vec{M}$ is the resulting magnetization of the particle, $[D\vec{H} / D\vec{x}]$ is the Jacobian spatial derivatives matrix, ∇ is the spatial gradient, and k is a constant that depends on particle properties. Here the first and second expressions are equivalent by the chain rule and it can be seen that the force on a MNP depends on both the particle magnetization $\vec{M}$ and the applied magnetic field gradient $\nabla\vec{H}$. In our experiments, the applied magnetic field was strong enough to saturate the particles hence $\|\vec{M}\|$ achieved its maximal strength of approximately 3.2 emu/g. Each magnet was placed underneath the tissue samples at a location, which produced a roughly constant magnetic motive force on the particles as they moved through the tissue, samples (please see Figure 3).

First, the magnetic field surrounding the bar magnets was measured using a Lakeshore 460-3 Channel Gaussmeter with a measurement range from 0.03 mT to 30 T. The device has a Hall probe (MMZ-2518-UH) encased in a protective brass sleeve attached to three orthogonal unislide components (from Velmex) forming a 3-D stage. The stepper motors controlling the stages have an internal step monitor for relaying signals via serial connection to a computer. The stepper motors have a resolution of 400 steps per revolution, with a single step corresponding to a displacement of 6.34 μm along any of the three axes (orthogonal directions). The 3-D stage can be controlled and sensed using a GPIB IEEE488 and RS232 connections to LabVIEW interface. The magnetic field around each permanent magnet was measured using this system.

Second, the above measurements allowed accurate calculation of the $\nabla\vec{H}$ value at each location around the magnet, and hence a good estimate of the strength of $\vec{M}\nabla\vec{H}$ that would be applied to particles at that location. The magnetic saturation value $||\vec{M}||$ was measured by vibrating sample magnetometry (VSM) as detailed in Sec.2.5.1. The resulting calculated spatial variation of $||\vec{M}\nabla\vec{H}||$ around the bar magnets is shown in Figure 3 below. Based on this data, in all experiments the top face of the bar magnet was placed ~ 6 mm below the MNPs to ensure that all particles experienced a starting motive force proportional to $||\vec{M}\nabla\vec{H}|| = 3.9 \pm 2 \times 10^8$ A^2/m^3. As the MNPs moved through the ~ 6 mm width of the tissue samples, $||\vec{M}\nabla\vec{H}||$ could potentially increase up to $||\vec{M}\nabla\vec{H}|| = 8 \pm 4.1 \times 10^8$ A^2/m^3, thus the applied magnetic motive force varied by at most a factor of two as the MNPs moved through the tissue samples. In Table 1,

the coefficient k varies with particle sizes and was determined experimentally using the radius and susceptibility measurements as explained in the section below. Magnetic force can be calculated as product of k and $\| \vec{M} \nabla \vec{H} \|$.

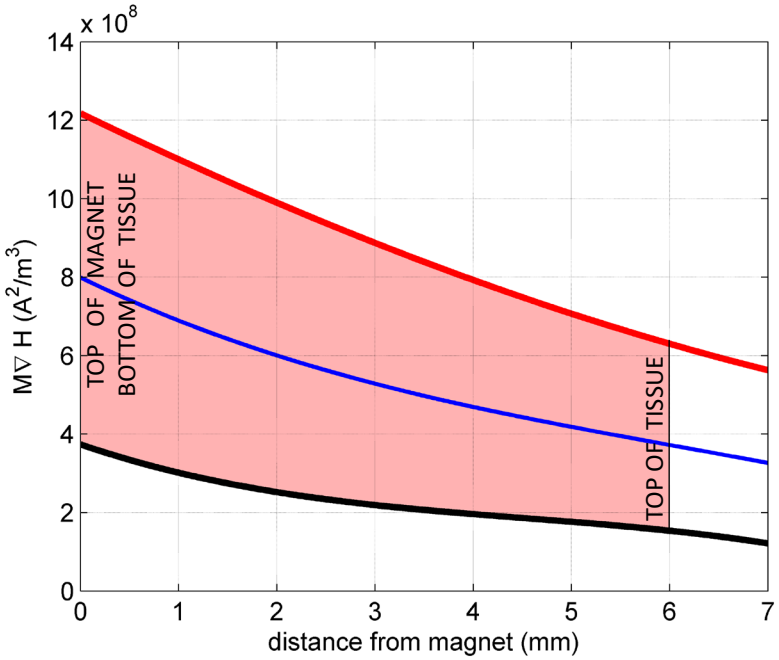

Figure 3 : Measured and calculated variation of the magnetic motive force on the magnetic particles as they moved through the tissue samples. The strength of the magnetic motive force is proportional to $\| \boldsymbol{M} \nabla \vec{\boldsymbol{H}} \|$, which is plotted above versus particle distance from the magnet (in units A^2/m^3). The red line indicates the estimated maximum, the black is the estimated minimum, and the blue line is the average value. Based on this data, we chose the magnet size in order to, as much as possible, apply a fairly uniform motive force across the entire tissue sample. As shown, the motive force increases by at most a factor of two from the top of the tissue (6 mm away from the top of the magnet) to the bottom of the tissue (right above the magnet surface).

	Particle Type (Size)			
	100 nm	300 nm	500 nm	1000 nm
k	$\approx 0.0007 \times 10^{-24}$ $N/(A^2/m^3)$	$\approx 0.0178 \times 10^{-24}$ $N/(A^2/m^3)$	$\approx 0.082 \times 10^{-24}$ $N/(A^2/m^3)$	$\approx 0.658 \times 10^{-24}$ $N/(A^2/m^3)$

Table 1: Approximate *k* values, for particles of various size, listed in units of $N/(A^2/m^3)$. The coefficient *k* relates the quantity $\| \boldsymbol{M} \nabla \vec{\boldsymbol{H}} \|$ shown above in Figure 3 with the actual magnetic force on the particle by $\|F| = k \| \boldsymbol{M} \nabla \vec{\boldsymbol{H}} \|$.

2.5 Properties of tested magnetic nanoparticles (MNPs)

Motion of MNPs through tissue depends upon their properties, such as their saturation magnetization, size, and surface charge. Before measuring the motion of particles through tissue samples, we first characterized the properties of each particle type using available measurement techniques. We used vibrating sample magnetometry (VSM) to measure saturation magnetization of particles, dynamic light scattering (DLS) to measure the size of the particles, and we further classified particles based on zeta potential measurements from Chemicell GmbH.

2.5.1 Magnetic properties of MNPs

The magnetic force on particles is proportional to the saturation magnetization of the particles and the gradient of the applied magnetic field intensity[31,87,112,135,149–153]. We measured the saturation magnetization for each particle type using a vibrating sample magnetometer (VSM)[154]. Table 2 shows magnetization values for each particle type, for the entire volume used (4 µl) in milli-electromagnetic units (memu) and also estimated per particle (as in the specification sheets from Chemicell, we divided the sample volume by the number of particles per volume to arrive at a per particle value). As expected, the per particle magnetization increases with particle size.

Size (nm)		Chitosan	PEG	Lipid	Starch	Mean + Standard Deviation
100	memu per 4µl	11.2	13.3	11.7	14.3	12.6+1.4
	memu per particle	6.2×10^{-11}	7.41×10^{-11}	6.5×10^{-11}	8×10^{-11}	$7 \times 10^{-11} + 8 \times 10^{-12}$
300	memu per 4µl	10	N/A	8	4.33	7.4+2.8
	memu per particle	1.5×10^{-09}	N/A	1.22×10^{-09}	6.6×10^{-10}	$1 \times 10^{-09}, +4 \times 10^{-10}$
500	memu per 4µl	7.9	N/A	N/A	7.3	7.6+0.4
	memu per particle	5.2×10^{-09}	N/A	N/A	4.9×10^{-09}	$5.1 \times 10^{-09} + 2.5 \times 10^{-10}$
1000	memu per 4µl	6	N/A	N/A	N/A	N/A
	memu per particle	3.3×10^{-08}	N/A	N/A	N/A	N/A

Table 2: Measured saturation magnetization values for the particles tested. For each particle size, the top entries are the measured value for the entire 4 µl volume sample in memu (milli-electromagnetic units), the bottom entries are the estimated per particle values. N/A (not available) is for particles types that could not be synthesized by Chemicell.

2.5.2 Size measurements of MNPs

The hydrodynamic diameter of the MNPs was measured by dynamic light scattering, as employed previously in Murdock et al [155–157]. We used a dynamic light scattering system from Photocor Instruments and found that the measured mean hydrodynamic measurements closely matched the specification provided by Chemicell GMBH. In most cases, we found that the peak of size distributions were within ± 50 nm of the radius of values listed in the particle specification sheets. However, it was found that some particles were highly polydispersed, i.e. more than one peak for the particle size distribution (e.g. for 100 nm PEG/P particles). The poly-dispersity and agglomeration of 100 nm PEG/P and 300 nm lipid particles led to a higher measurement of hydrodynamic radius. Detailed size distribution plots are further provided in Figure 4.

The instrument was calibrated using the particle size distribution plots for two NIST standard polymer particles of 100 and 300 nm respectively. The distribution plots for these particles are shown in Figure 5. All other particles were tightly distributed around the specified values as can be seen from Table 3 below.

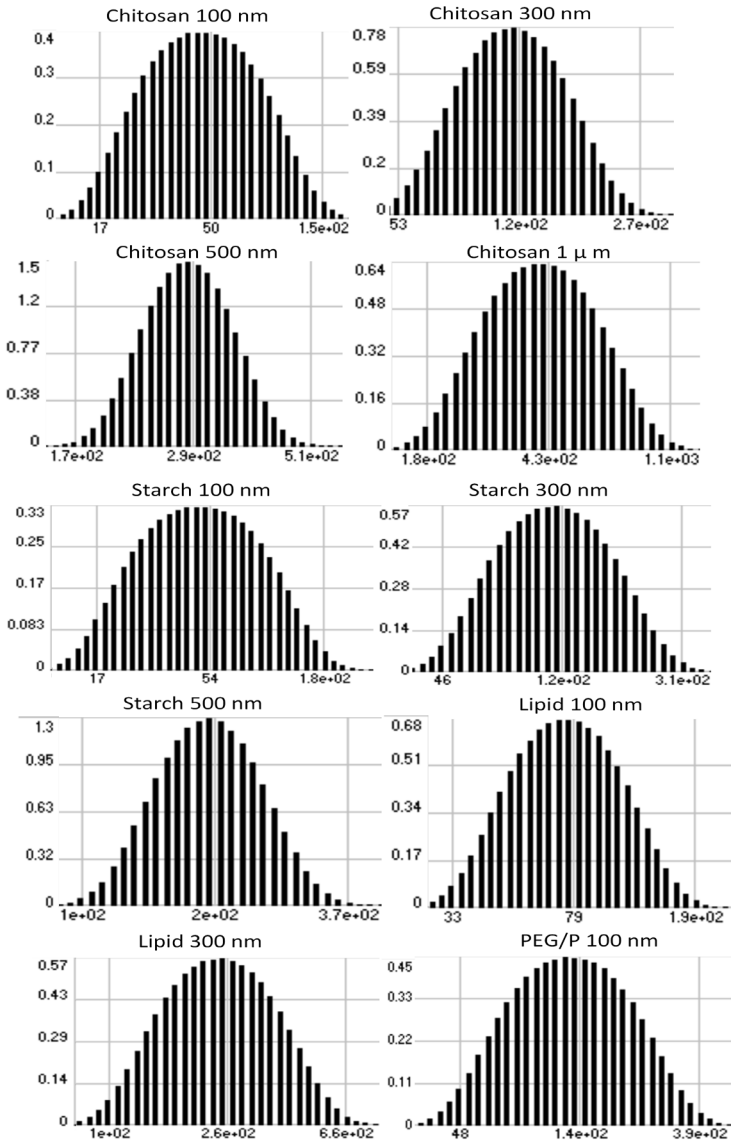

Figure 4: Particle distribution plots showing intensity vs particle hydrodynamic radius, based on DLS measurements using Photocor Instruments are shown above. The hydrodynamic radius of MNPs matches closely with the specified radius from Chemicell. Note that 300 nm Lipid and 100 nm PEG/P particles had larger size according to DLS measurements, possibly due to agglomeration.

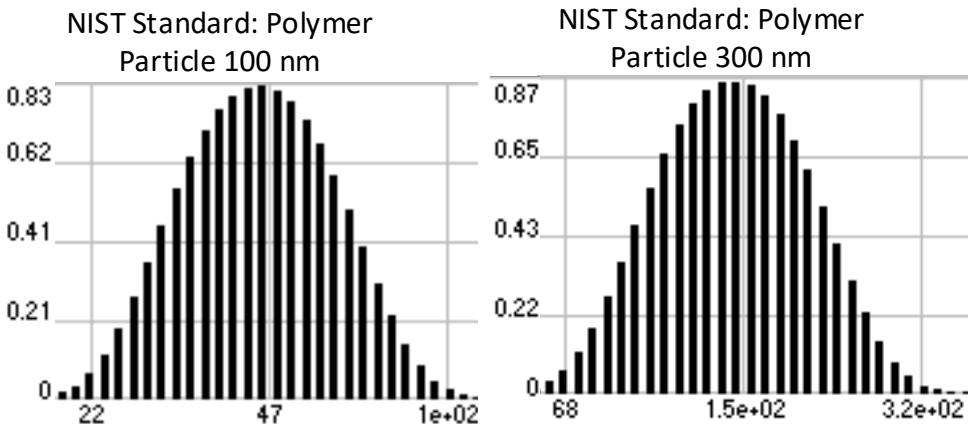

Figure 5 : Particle distribution plots showing intensity vs particle hydrodynamic radius for NIST polymer particles of size 100 nm and 300 nm diameters, based on DLS measurements using Photocor Instruments are shown above.

	100 nm		300 nm		500 nm		1μm	
	Mean	Polydispersity	Mean	Polydispersity	Mean	Polydispersity	Mean	Polydispersity
Chitosan	49.9	0.99	119	0.528	267	0	524	1.08
Starch	45	1.34	116	0.77	254	0		
Lipid	78	0.06	257	0.67				
PEG/P	131	0.8						

Table 3 : Measurements of the hydrodynamic radius of Chemicell MNPs using the DLS (dynamic light scattering) system from Photocor Instruments shows that most particles comply with the particle sizes specified by Chemicell. However, the PEG/P and lipid particles were found to have poly-dispersity and agglomeration.

2.5.3 Zeta Potential of MNP Coatings

The ability of the MNPs to repel each other and remain dispersed in solvent is determined by their zeta potential[158–160]. Zeta potential is the charge on the outer liquid layer of the particle. Stronger charges (positive or negative) keep the particles more dispersed. Hence the zeta potential determines the initial state of the particles and can alter the rate of aggregation of particles and hence potentially their ability to move through tissue. For the experiments in this paper, we consider four types of

particle coatings: chitosan, polyethylene glycol (with a phosphate group that led to negative charge), lipid and starch. The stated zeta potential of each type of coating is provided in Table 4. These values were obtained from Chemicell GmbH.

	Chitosan	PEG	Lipid	Starch
Charge Potential	+34	-20	-19	-8

Table 4: Zeta potential values for each particle type and coating in mV.

2.6 Experimental Procedure

For each experiment, a known volume of fluorescent MNPs (a 4 microliter droplet that stayed within the profile area of the tissue) was placed on top of a tissue surface. The tissue had been immobilized using gelatin in a petri-dish. The petri dish was then immediately placed on top of a permanent magnet, for 45 minutes. The tissue was placed directly above the magnet so that the maximum magnetic field was acting on the particles. As described earlier, the magnet size had been selected so that this motive force would not change too greatly as the particles traversed the tissue samples. After magnet application, the tissue was immediately fixed by flash-freezing in liquid nitrogen. The frozen tissue was then stored at -80° C. The fixed tissue samples were then embedded in optimal cutting temperature (OCT) fluid from Tissue-Tek Inc., for simultaneous slicing and imaging using an automated cryostat imaging system previously described in Shen et al.[148]. The automated cryostat has a single fluorescent camera with a resolution of 35 μm per pixel that captures bright field and fluorescent images of each tissue slice and the fluorescence distribution of

particles within that slice. The complete stack of images of all tissue slices provided the entire three-dimensional distribution of fluorescent MNPs in that tissue sample. The slicing plane for the imaging was chosen to be parallel to the planes in which the particles moved from the top of the tissue towards the magnet at the bottom (see Figure 1). The collected images provided quantitative information on the depth of penetration of the MNPs, as discussed next.

2.7 Post-Processing of Images

In order to assess the depth of MNP penetration into tissues, we analyzed the images acquired by the automated cryostat. For each slice of tissue, the fluorescent camera captures two images: one bright field image showing tissue and background and one fluorescent image showing only particles. Each image captured by the camera is stored as a matrix of pixels in unsigned integer 16 format. In case of bright field images, a zero value of the pixel represents a black color and the maximum value of 2^{16} represents a white color. Similarly, in the case of fluorescent field images, a maximum pixel value represents bright fluorescence while 0 represents the absence of fluorescence and particles. The images acquired by the fluorescent camera of the automated cryostat required substantial processing in order to reliably extract a distance metric. The processing of images involved the following steps:

A. Data Cleaning**:** The automated cryostat slicing generated some random images along with useful images, due to electrical noise and sometimes due to overlapping of a previous slice with the current slice. To remove all spurious images, we stacked all image data for all slices and formed a vector whose

every element was the total intensity of each slice/image. Since good images have tissue and OCT region, and since OCT is white (white represents high grayscale intensity values close to 2^16) while tissue is dark gray (black represents low grayscale intensity values close to zero), we could easily filter out bad images using a median filter. Example good and bad images are shown in Figure 6A.

B. Image Alignment**:** The tissue-OCT sample was sometimes not exactly aligned in the desired top-to-bottom orientation due to error in placing the sample on the cryostat slicer. All tissue images were rotated until the top surface (indicated as a red line in Figure 6B) was horizontal to within ± 1 degree.

C. Cropping for Image Processing**:** We then cropped the first image of each sample until only the dark gray tissue region and some surrounding white OCT regions were visible in the image. This cropped region was used for all slices of the corresponding sample. This enabled further image processing.

D. Image Thresholding**:** Based on bright field images and their pixel intensities, an image intensity histogram was plotted and a threshold of intensity was selected such that the dark and bright regions could be clearly demarcated. Then, every region other than the tissue region was masked by assigning pixel values of zero.

E. Assigning Regions of Interest**:** Since the fluorescent image and bright field image are spatially co-registered, we masked the same region in the fluorescent image that was outside the tissue region (as in step D above) by

assigning pixel values of zero. As a result, only regions inside tissue have non-zero pixel intensities. This was done for all slices to ensure that only the tissue region was considered for each particle depth measurement.

F. Total Fluorescence Intensity Vector along Tissue Depth**:** Each vertical tissue image (slice) is represented by a matrix of pixel intensities with each pixel corresponding to a 35 μm x 35 μm area. The degree of fluorescence is correlated to the amount of particles in that pixel. To reduce computational burden, the intensities of particle concentrations along each horizontal row of this matrix were summed up. These sums were collected into a single vertical vector $\vec{i} = [i_1, i_2, ..., i_n]$ each of whose elements is the net particle intensity at that tissue depth for this single vertical slice. Plotting this vector illustrates the profile of total fluorescence intensity with tissue depth, as shown in step E. Each single vector thus formed represents total fluorescence intensity distributed along the depth for a single slice. Summing all such vectors (so summing over all vertical slices) yields a total fluorescence intensity distributed along depth for the whole tissue block: $\bar{I} = \sum_{all-slices} \vec{i}$.

G. Auto-Fluorescence Removal**:** In order to account for auto-fluorescence in tissue, steps A-E were performed on control samples without particles. The average of all pixel intensities from control samples was used as the auto-fluorescence intensity in that tissue type e.g. in liver, kidney or brain. This average pixel intensity of auto-fluorescence was then subtracted from the fluorescence intensity computed in step F.

H. Depth Metric: In order to quantify the distance traveled by the particles in each tissue sample, we computed the centroid of the particle vertical distribution. Let I_i represent the total fluorescent intensity at a depth d_i (representing the i^{th} element of the column vector in F above). That value was normalized with respect to the maximum intensity at depth d_i from the top of tissue, and then the centroidal distance that the particles moved was computed as $\boldsymbol{d}_c = \sum_{i=1}^{n}(\boldsymbol{d}_i \cdot \boldsymbol{I}_i) \Big/ \sum_{i=1}^{n} \boldsymbol{I}_i$. This distance metric was used for quantifying the movement of the tested particle types in the various tissues.

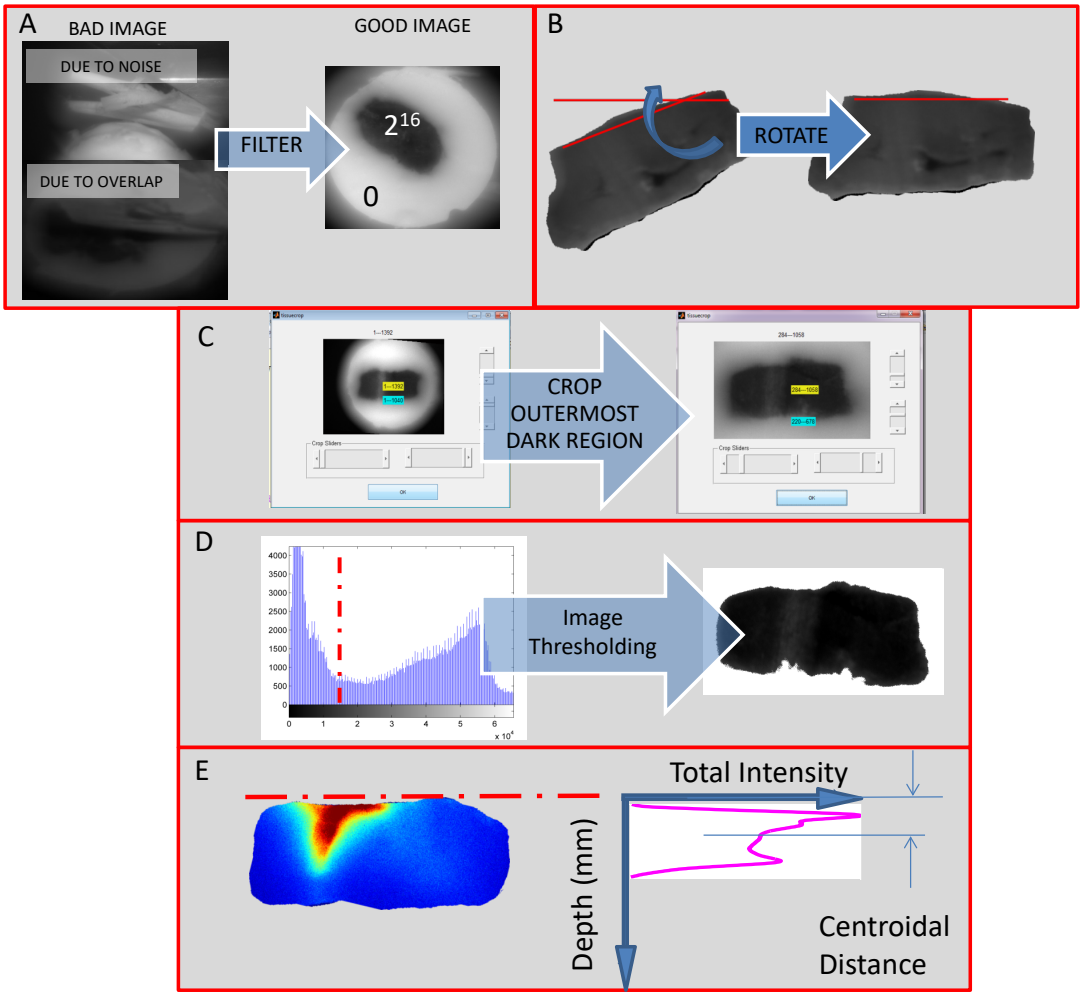

Figure 6: Image processing steps: (A) A bad image resulting from random capture of an image due to noise or overlapping of a previous slice is removed. This was a rare event, but such images were removed to clean the database. On the right, a good image that is retained is shown. In the good image, the tissue region has pixel values close to zero (dark) and OCT region has pixel values up to 216 (close to white). (B) Tissue images were sometimes not correctly aligned. A typical misalignment was 20° and usually occurred due to tissue placement error (tissues had to be placed on the cryostat quickly in order to minimize temperature changes). All images were rotated until the top surface appeared horizontal. (C) Dark background was cropped until only white OCT background and dark tissue background was visible, this was done in order to facilitate image processing. (D) The image was thresholded and the bright OCT region was assigned a complete white intensity (255) so that only tissue region was considered for particle measurement. (E) In this coloring, fluorescent particles with high intensities can be seen (red corresponds to a pixel value of 216, blue corresponds to a pixel value of zero). The sum of all intensities across a single row represents the total number of particles at that depth. The resulting pink curve shows the distribution of particles with depth. The centroid of this pink curve quantifies the depth of penetration of particles into the tissue sample.

2.8 Results

To begin to understand the effect of magnetic field, particle characteristics, and tissue environment on the motion of particles, we studied three types of tissue: liver, kidney and brain, and four types of particles: starch, chitosan, lipid and PEG/P. For each tissue-particle pair, we conducted two types of experiments: 1) we let the particles passively diffuse through the tissue and 2) we held a permanent magnet (0.4 T field strength at its surface) immediately below the tissue in order to exert a maximal magnetic force on the particles at the top of the tissue. After conducting the experiments as described in Sec. 2.6 , we measured the fluorescence distribution of particles in tissue samples for each case and computed the centroidal distance d_c. In Figure 7 we show representative fluorescent images to illustrate penetration of three different particle types (100 nm chitosan, 100 nm PEG/P and 300 nm lipid) in three types of tissue slices (liver, kidney and brain) resulting from passive transport and magnetic drift. As can be seen from Figure 8, application of the magnet increased particle motion for 100 nm particles in liver and the brain.

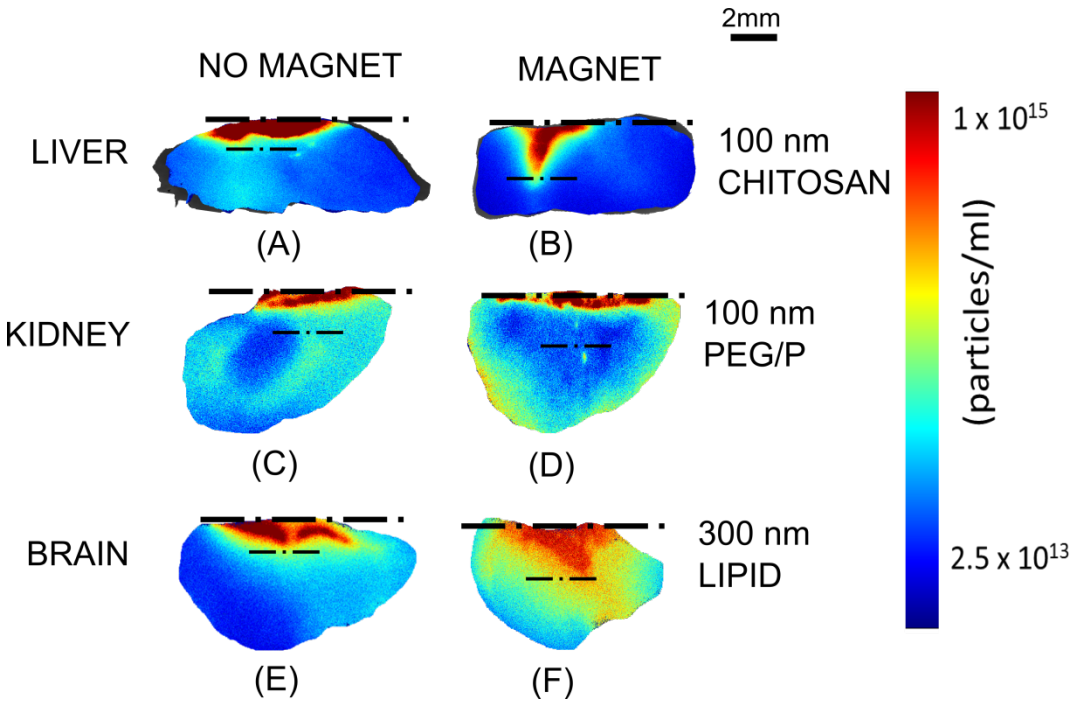

Figure 7 : Magnetic transport of particles versus diffusion alone. The images show fluorescence distribution in three types of particle-tissue pairs for passive and magnetic transport. In each case, dc is centroidal distance that particles penetrate in tissue (dc is defined in Sec. 0, step H). Chitosan 100 nm particles (A) passively diffusing through liver tissue demonstrated limited movement (dc = 2.6 mm) versus (B) moved substantially when pulled with a magnet (dc = 5.3 mm). PEG/P 100 nm particles (C) passively diffused through a section of kidney showing some spreading and diffusion (dc= 2.6 mm) versus (D) showed some small additional movement when pulled with a magnet (dc = 3.0 mm). Lipid 300 nm particles (E) showed limited diffusion in brain tissue (dc = 2.5 mm) versus (F) substantial magnetic drift (dc = 5 mm).

The degree of particle penetration into tissue samples under an applied magnetic field was then quantified for each particle type and tissue type pair. Each experiment was repeated three times (N=3) and the averaged penetration depth and its standard deviation are shown below in Figure 8. Since our experiments were repeated only three times, we computed coefficient of variation for each experiment. The coefficient of variation was 0.25 on average with a maximum of 0.78 and a minimum of 0.038. We have tabulated the results for each experiment in Table 5, Table 6, Table 7 and Table 8.

	BRAIN				LIVER				KIDNEY			
Zeta (mV)	34	-8	-19	-20	34	-8	-19	-20	34	-8	-19	-20
Coating / Size	Chitosan	Starch	Lipid	PEG/P	Chitosan	Starch	Lipid	PEG/P	Chitosan	Starch	Lipid	PEG/P
100 nm	4.3±0.5	2.4±1.4	3.8±1.5	4.7±1	5.3±0.2	2.86±1	4±0.9	5.2±1.6	4.1±1.2	1.78±1.4	3.5±1	3.0±0.8
300 nm	3.9±1.0	3.5±1.3	5.0±0.9		3.6±0.2	3.9±1.2	2.8±1.4		3.1±0.5	2.9±1	5.1±1.8	
500 nm	4.4±1.7	3.4±0.8			4.8±2.1	3.4±0.9			5.6±1.6	4.9±1.1		
1 micron	4.7±0.6				3.4±0.2				5.6±0.6			
	Relatively low			<2.5			High		4.5-5.25		mean±std dev.	
	Moderate			2.5--3.5			Very High		>5.25			
	Relatively high			3.5--4.5			Not available from Chemicell					

Table 5 : Tissue penetration after 45 minutes of pulling by a 0.4 Tesla magnet for various particle sizes (100 nm – 1 μm diameter), coating (chitosan, starch, lipid and PEG/P), and tissue types (rat brain, liver and kidney). Colors denote degree of penetration into the tissue, from red (low penetration) to green (high), as noted in the legend at the bottom.

	BRAIN				LIVER				KIDNEY			
Zeta (mV)	34	-8	-19	-20	34	-8	-19	-20	34	-8	-19	-20
Coating / Size	Chitosan	Starch	Lipid	PEG/P	Chitosan	Starch	Lipid	PEG/P	Chitosan	Starch	Lipid	PEG/P
100 nm	1.8±0.9	3.5±1.1	2.8±1.3	2.5±0.8	2.6±1.3	2.7±0.4	2.4±0.7	3.4±0.8	3.4±0.9	4.5±0.6	4.4±0.6	2.6±0.8
300 nm	3.8±1.5	3.2±0.35	2.5±0.5		3.2±1	3.9±1.2	2.6±1.2		2.5±0.7	3.4±1.2	4.5±0.9	
500 nm	2.7±0.2	3.8±1.2			3.9±0.4	2.0±0.26			3.0±0.8	3.1±0.96		
1 micron	2.5±1.2				2.8±0.8				2.4±0.4			
	Relatively low			<2.5			High		4.5-5.25		mean±std dev.	
	Moderate			2.5--3.5			Very High		>5.25			
	Relatively high			3.5--4.5			Unavailable from Chemicell					

Table 6: Tissue penetration after 45 minutes of passive transport for various particle sizes (100 nm – 1 μm diameter), coating (chitosan, starch, lipid and PEG/P), and tissue types (rat brain, liver and kidney) is shown above. Colors denote degree of penetration into the tissue, from red (low penetration) to green (high), as noted in the legend at the bottom.

	BRAIN				LIVER				KIDNEY			
Zeta (mV)	34	-8	-19	-20	34	-8	-19	-20	34	-8	-19	-20
Coating / Size	Chitosan	Starch	Lipid	PEG/P	Chitosan	Starch	Lipid	PEG/P	Chitosan	Starch	Lipid	PEG/P
100 nm	0.116	0.583	0.395	0.213	0.038	0.350	0.225	0.308	0.293	0.787	0.286	0.267
300 nm	0.256	0.371	0.180		0.056	0.308	0.500		0.161	0.345	0.353	
500 nm	0.386	0.235			0.438	0.265			0.286	0.224		
1 micron	0.128				0.059				0.107			
	<0.2						High		<0.8	Coefficient of Variation		
	<0.4						Very High			Std.Dev/Mean		
	<0.6						Unavailable from Chemicell					

Table 7: Coefficient of variation for N=3 experiments showing dispersion in tissue penetration after 45 minutes of pulling by a 0.4 Tesla magnet for various particle sizes (100 nm – 1 μm diameter), coating (chitosan, starch, lipid and PEG/P), and tissue types (rat brain, liver and kidney). Colors denote amount of coefficient of variation of penetration into the tissue, from red (low) to green (high), as noted in the legend at the bottom. On an average the coefficient of variation was 0.25 with a maximum of 0.78 and minimum of 0.038.

	BRAIN				LIVER				KIDNEY			
Zeta (mV)	34	-8	-19	-20	34	-8	-19	-20	34	-8	-19	-20
Coating / Size	Chitosan	Starch	Lipid	PEG/P	Chitosan	Starch	Lipid	PEG/P	Chitosan	Starch	Lipid	PEG/P
100 nm	0.500	0.314	0.464	0.320	0.500	0.148	0.292	0.235	0.265	0.133	0.136	0.308
300 nm	0.395	0.109	0.200		0.313	0.308	0.462		0.280	0.353	0.200	
500 nm	0.074	0.316			0.103	0.130			0.267	0.310		
1 micron	0.480				0.286				0.167			
	<0.2						High		<0.8	Coefficient of Variation		
	<0.4						Very High			Std.Dev/Mean		
	<0.6						Unavailable from Chemicell					

Table 8: Coefficient of variation for N=3 experiments showing dispersion in tissue penetration after 45 minutes of passive transport for various particle sizes (100 nm – 1 µm diameter), coating (chitosan, starch, lipid and PEG/P), and tissue types (rat brain, liver and kidney). Colors denote amount of coefficient of variation of penetration into the tissue, from red (low) to green (high), as noted in the legend at the bottom. On an average the coefficient of variation was 0.27 with a maximum of 0.5 and a minimum of 0.07.

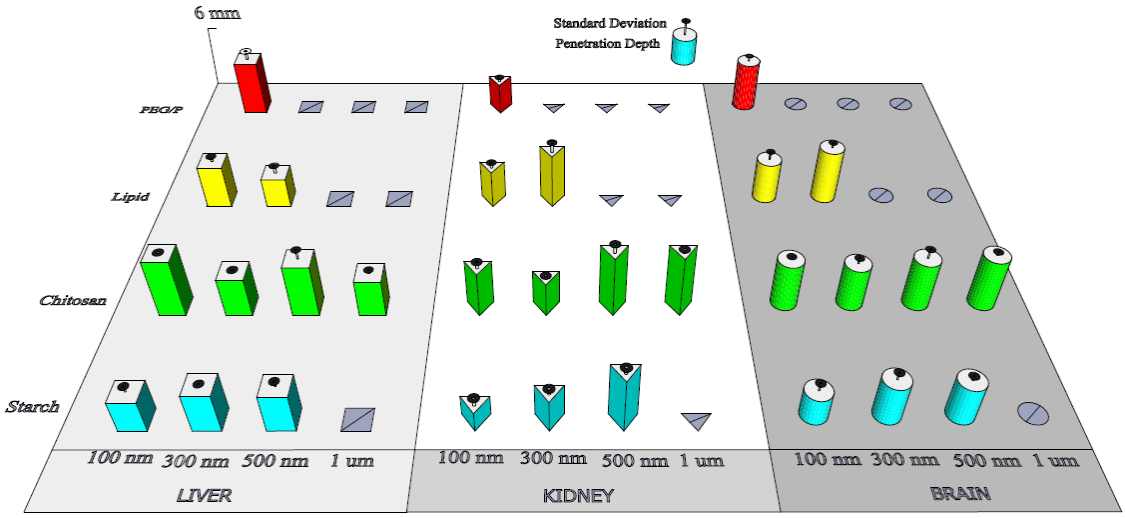

Figure 8 : Tissue penetration after 45 minutes of pulling by a 0.4 Tesla magnet for various particle sizes (100 nm to 1 µm diameter), with various coating (chitosan, starch, lipid and PEG/P), in different tissue types (rat brain, liver and kidney). Colors denote the type of coating, the shape of the prism denotes the tissue type, and the height of prisms shows the degree of penetration into that tissue. The vertical bar with black disk above it denotes the standard deviation of the measurement. Particles types that were not available from Chemicell are marked by the crossed-out symbols.

After comparing all available fluorescent Chemicell particle types and their movement through brain, liver, and kidney tissue types, we found that the average

particle penetration depth in all three tissue types fell within a range of 1.78 mm and 5.6 mm when exposed to a ~ 0.4 Tesla magnetic field for 45 minutes. Hence, the average velocity of particle motion in liver, kidney and brain tissue was found to lie between 0.66 and 2 μm/s. The particle motion was slowest for 100 nm starch particles through kidney and was fastest for 1 μm chitosan particles in kidney.

We compared the effect of particle coatings on the magnetic drift of particles through tissue. Among all coating types, for available fluorescent particles from Chemicell, we found that chitosan particles (with +34 mV zeta potential) moved better through the liver, kidney and brain than starch particles (with -8 mV zeta potential) for particles of all sizes (100 nm to 1 μm). In Figure 8, the penetration of chitosan particles (green bars) is higher than the penetration of starch particles (blue bars), except for the 300 nm size where starch particles penetrated slightly deeper than chitosan in liver tissue. Starch particles with a 1 μm diameter were not available from Chemicell, as mentioned before, and are marked by a data-not-available symbol (crossed-out square, triangle or circle).

Comparison of particle penetration due to magnetic drift versus passive diffusion in all tissue types for all particle sizes tested showed that penetration due to magnetic drift is more effective than passive diffusion for strongly positively charged particles such as chitosan (+34 mV) and strongly negatively charged particles such as PEG/P (-20 mV). The computed mean and standard deviation of centroidal distance

penetration by chitosan and PEG/P particles, for magnetic drift versus diffusion, is shown by green and red prisms in Figure 9.

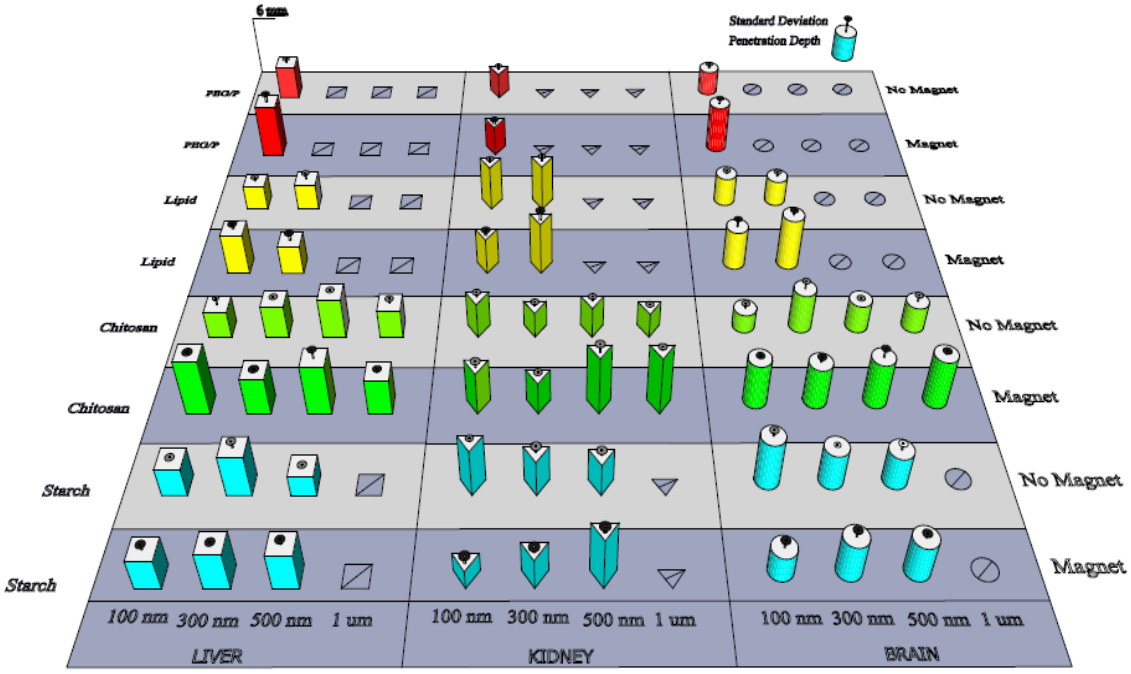

Figure 9: Tissue penetration after 45 minutes of passive diffusion and pulling by a 0.4 T magnet for all tested particle sizes (100 nm, 300 nm, 500 nm and 1 μm) and all available coatings (starch represented as blue, chitosan as green, lipid as yellow and PEG/P as red prisms). Penetration depth is represented by the height of each prism. The shape of the prisms represents movement through specific tissue type: square prisms denote movement through liver, triangular prisms denote kidney and cylinders denote brain. The color of the substrate (the base on which the prisms lie) denotes the presence of a pulling magnet (dark gray substrate) versus the absence of a magnet (diffusion only, light substrate).

Apart from the above clearly discernable trends, we observed some more nuanced effects of particle size on magnetic movement through tissue. Comparison of nanoscreenMag particles (up to 300 nm in size) showed that the smallest (100 nm) chitosan particles penetrated deeper than 300 nm size chitosan, in all tissue types. Among screenMag chitosan particles (500 nm size and above), the 500 nm sized particles penetrated deeper in the liver, penetrated to the same depth in the kidney, and penetrated less deep in the brain, compared to their 1 μm sized counterparts. The

largest available 1 μm particles with chitosan coating penetrated the deepest through kidney and brain tissues, but this was not the case for motion in liver tissue.

From Figure 8, we can also observe that penetration of particles due to magnetic drift increased with size for starch particles. This behavior was consistent for all starch particles (sizes 100 nm to 500 nm) in all tissue types. The blue triangular prisms for kidney tissue clearly show increasing penetration depth with starch particle size, although this increase is less pronounced when comparing 300 nm to 500 nm starch particles in liver and brain tissues.

We can also compare particle penetration due to magnetic drift for the available 100 nm and 300 nm lipid particles in liver, kidney and brain. As shown in Figure 8, the particle penetration was higher for 300 nm lipid particles compared to 100 nm lipid particles in kidney and brain tissue, as shown by the taller yellow triangular prisms and cylinders and their shorter counterparts for 100 nm particles. However, this behavior was reversed in the case of liver, as shown by the taller 100 nm yellow square bar compared to the shorter 300 nm yellow bar in the liver section in Figure **9**. Lipid particles larger than 300 nm were unavailable and are marked by a cross-out diagonal within the square, triangle, or circle shapes. We made every effort to insure that our results in freshly excised tissue would match *in-vivo* behavior as closely as possible. The time between organ excision and experiment was less than two hours, and according to accepted tissue handling procedures the tissue was preserved in cool environment (4ºC), and stored in phosphate buffer solution. This procedure and time

interval is within the time interval studied in transplant research and research for studying the mechanical properties of tissue[145,161–163]. Further, the tissue organs we selected (liver, kidney, and brain) were significantly larger than the volume of MNPs used, and only the outer surface of the tissue was exposed to the liquefied gelatin used for immobilizing the tissue. This protected the particle penetration path from the external environment to some extent, and we believe it helped ensure that the collected data will be representative of magnetic particle motion *in-vivo*.

2.9 Conclusions

An experimental method was presented to quantitatively measure the penetration depth of magnetic nano-particles (MNPs) into tissue samples under the action of an applied magnetic field. In this method, MNPs were placed on top of freshly excised liver, kidney, and brain tissue samples and were then pulled into the samples by a magnet placed underneath the tissues. The tissue samples were sliced by an automated cryostat, fluorescence from the particles was imaged and processed, and the degree of MNP penetration was quantified by a centroid distance metric. Tests were conducted on available fluorescent particles from Chemicell in four sizes (100 nm, 300 nm, 500 nm, and 1 μm diameter) and with four different coatings (starch, chitosan, lipid, PEG/P). The average particle penetration depth in all three tissue types, after a 45 minute application of a 0.4 Tesla 1” x 1” x 2” magnet, was between 1.78 mm and 5.6 mm, which corresponds to a transport velocity between 0.66 and 2 μm/s. We found that chitosan particles moved most effectively through all three-tissue types (compared to starch, lipid, and PEG/P coated particles). However, we

observed many additional dependencies on particle size, coating, and tissue type, which indicate that the motion of MNPs in tissue is complex and that additional studies will be required to elucidate transport mechanisms in tissue and to engineer MNPs for optimal transport in tissue. We also stress that our data was collected in freshly excised tissue, not *in-vivo* in live animals, and differences between excised and living tissue may affect MNP motion in ways that are not captured by this study.

Chapter 3: Movement of magnetic nanoparticles in brain tissue: mechanisms and safety

This work originally appeared in [164]

3.1 Background

Nanotechnology based solutions for the treatment of brain tumors have been used in recent years to address the challenges faced by conventional cancer therapeutics[165] such as surgery[166,167], chemotherapy[39,168,169] and radiation therapy[170,171]. Drugs such as doxyrubicin[88] and oxantrazole[172] can be combined with appropriate nanocarriers to penetrate the blood brain barrier (BBB) and increase the intracellular concentration of drugs in tumor cells[173,40,174]. Magnetic nanoparticles (MNPs) have been investigated as effective nanocarriers for targeted drug delivery in the brain[175,49,55,176]. Such MNPs, with attached drugs, proteins, or genes, could be imaged using MRI technology and guided towards brain tumor locations using external magnets.

MNPs with an aminosilane coating have been investigated in human trials for targeting glioblastoma multiforme cells and have been shown not to cause any adverse effects in patients. In the presence of an alternating magnetic field, the MNPs were found to extend tumor necrosis with minor or no side effects in the patients[176]. Hassan and Gallo showed that after a systemic injection of magnetic chitosan microspheres coated with oxantrazole, while in the presence of a 6000 Gauss magnetic field, the guided microspheres accumulated in targeted rat brain tissue[172].

Thus MNPs have been shown to cross the BBB and reach targets in brain tissue without disrupting the barrier in rat models[49,177].

Furthermore, endothelial progenitor cells (EPCs) from humans have been loaded with MNPs and guided to targets in mouse brains[178]. These EPCs loaded with MNPs have shown increase in secretion and migration of growth factors such as VEGF and FGF, in vitro, thereby promoting angiogenesis for neural regeneration. Various in vitro studies have shown that cancer cells can be made to internalize a higher level of nanoparticles with drugs by appropriate targeting of receptors[179,180,181,182]. The MNPs, therefore, can be used as a potential option to circumvent the challenges faced by conventional drug delivery techniques.

Most of the work mentioned above has focused on the motion of MNPs through blood vessels and the observation of MNP presence in living tissue[49,183,184]. The motion of MNPs in brain tissue surrounding the blood vessels is expected to differ from its motion in the vessels. Hence there is a need for a better understanding of the motion of MNPs in brain tissue after extravasating from blood vessels. The MNP motion in tissue should be safe. It must not be cytotoxic, nor should it affect the normal function of the intricate neural networks in the brain so as to eliminate the possibility of permanent side effects in the brain following the delivery of drugs using MNPs. Addressing these needs will result in better nanotherapeutic schemes to target tumors in brain tissue.

In the current work, we have studied the movement of magnetic nanoparticles (MNPs) in brain tissue under an applied magnetic field. The movement of MNPs throughout this work includes the interactive motion of MNPs towards each other caused by the influence of an external magnetic field. The mechanisms of this MNP motion and the primary factors that impact this motion have been explored. We found that the motion of MNPs did not cause any detrimental effects on the functional health of the neurons or the circuit function in the main olfactory bulb, a well-studied region in the brain. We examined the functional safety aspects of MNP motion by using whole-cell patch recordings, imaging and immunohistochemistry in the main olfactory bulb.

3.2 Experimental methods

3.2.1 Characterization of magnetic nanoparticles

The physical properties (mean hydrodynamic diameter, polydispersity index) of MNPs (nano-screenMag, Chemicell, listed as 300 nm diameter) used in our experiments were determined using dynamic light scattering. The MNPs were required to be monodispersed to avoid non-uniformity in their motion in the tissue caused by particle size variations. For the dynamic light scattering measurements, the stock concentration of MNPs (25 mg/mL in double distilled water) was diluted with de-ionized water to a concentration of 0.25 mg/mL. Three samples of 3 mL of the diluted solution were used for the measurement assays. The particle size distribution curve was plotted for these samples and used to calculate the polydispersity index (Figure 10A).

The magnetic properties of the nanoparticles including magnetic susceptibility and saturation magnetization were measured using a vibrating sample magnetometer (Lake Shore Cryotronics Inc.). Sample volumes of 60 μL of MNPs in DI water were pipetted into the sample holder (Kel-F) and the holder was placed in the vibrating sample magnetometer setup. The experiments were performed at room temperature (298 K). The samples were exposed to a cycle of different magnetic field values in the range of -1.5 to +1.5 Tesla and the corresponding net magnetization produced in the samples were recorded. The magnetic properties (susceptibility and saturation magnetization) of the samples were then calculated from the magnetization versus magnetic field (M vs H) plot obtained from the vibrating sample magnetometer (Figure 10B).

3.2.2 Uniform magnetic field using a two magnet setup

A system was created to apply a uniform magnetic field to magnetic particles inside brain tissue slices. A uniform magnetic field was desired so that all MNPs in the tissue would experience the same magnetic field irrespective of their location in the tissue. Two permanent magnets, appropriately sized and placed as shown in Figure 1A, were sufficient to create a uniform magnetic field. The uniformity of the field was verified by a 3-channel Gaussmeter (Lake Shore Inc.) mounted on a piezo positioning stage (VXM Motor Inc.). The Gaussmeter measured the spatial distribution of the magnetic field intensity between the two magnets and it was found that the deviation from the mean magnetic field intensity in the tissue sample volume was less than 1%. This data is displayed in Figure 11.

3.2.3 Motion experiments of MNPs in the brain tissue

The motion of MNPs towards each other under the influence of an applied uniform magnetic field was studied in rat brain tissue using a total of 12 rats (Sprague Dawley). Each different motion experiment was repeated three times using tissue from different rats to ensure that the data was independent of animal to animal variability. The rat brains were dissected out and immediately stored at 4°C in 1X Phosphate Buffer Saline (PBS) solution to increase their viability. After 15 minutes, the brains were injected in the prefrontal cortex with 4 μL of the MNPs, using a 10 μL micro-syringe (Hamilton). Following this injection we obtained cortical slices using a razor blade. The slicing was facilitated by the low temperature storage of the brain samples. The slices containing the injected MNPs were then stabilized at room temperature in 1X PBS solution in a petri dish. The MNPs were visualized by fluorescence using a lipophilic dye coating (Texas Red, Chemicell) with excitation and emission wavelengths of 578 nm and 613 nm respectively. The petri dish containing the brain tissue, immersed in PBS, was placed in the uniform magnetic field region of the two magnet setup. The effect of the uniform magnetic field on the MNPs in the brain tissue was observed using a fluorescent microscope (Zeiss) with 40X magnification and recorded using a video camera (Hamamatsu). The videos were post-processed in MATLAB (Mathworks) to quantify the movement of the MNPs in the uniform magnetic field.

3.2.4 Electrophysiological recordings

All animal studies were conducted in accordance with the policies and recommendations of the National Institute of Health Guide for the Care and Use of Laboratory Animals, and under approval from the Institutional Animal Care and Use Committee of the University of Maryland. The electrophysiological recordings were performed in brain slices extracted from wild-type BL6/C57 mice (Jackson Labs), or 4-6-week-old transgenic mice expressing green fluorescent protein (GFP) and subjected to MNP motion. Specifically, we used the ChAT-Tau-GFP line, generously provided by Dr. Sukumar Vijayaraghavan [185]. We performed these electrophysiology experiments in mice because of the feasibility of transgenic modification in a mouse model compared to a rat model. All the functional experiments involved whole-cell patching of neurons in an electrophysiology setup. The transgenic modification of mice enabled us to visualize the GFP expressing neurons in the presence of MNPs around them using a fluorescence microscope with multiple wavelength filters. Neurons from at least 5 different brains were used for the studies. The animals were anesthetized with isofluorane and decapitated. The whole brain was removed and immediately placed in ice-cold oxygenated artificial cerebrospinal fluid (ACSF). The ACSF used for the experiments contained the following composition (in mM): 125 NaCl, 25 $NaHCO_3$, 1.25 NaH_2PO_4, 3 KCl, 2 $CaCl_2$, 1 $MgCl_2$, 3 myo-inositol, 0.3 ascorbic acid, 2 Na-pyruvate, and 15 glucose. The solution was maintained at a constant pH of 7.4 and osmolarity of ~ 350 mOsm by continuous oxygenation (95% O_2- 5% CO_2). A block of the extracted tissue, containing the olfactory bulb, was glued to a stage with cyanoacrylate and bathed in ice-cold low Ca^{2+}, high

Mg^{2+}ACSF. Sagittal brain sections (250-300 μm), containing the olfactory bulb were sliced using a vibratome slicer (Leica). The slices were held at 34 °C for 30 minutes and then at room temperature to recuperate.

The slices were then transferred to a Petri dish and the MNPs were injected into the slices using a glass micro-pipette (≈ 5 μm diameter) attached to a micro injection system (Toohey spritzer). The MNPs in the brain slice were visualized using a fluorescence microscope and the two magnet setup was introduced for 5 minutes to produce MNP motion and chaining. Then the two magnet system was rotated by 90° to produce motion of MNPs in a perpendicular direction to ensure that the functional safety of neurons did not depend on the direction of MNP movement. The slices were then placed in the electrophysiology recording chamber mounted on the stage of an upright fluorescence microscope (Zeiss) and the region of the tissue containing MNPs was identified using fluorescence. Then neurons in that region were patched for electrophysiology recordings. The recordings were carried out in current-clamp and voltage-clamp mode using standard patch pipettes (3-7 MΩ resistance) pulled on a horizontal puller (Sutter). To further assess neuronal integrity and viability in slices loaded with MNPs, after the application of a magnetic field, we included the fluorescent dye Alexa-Fluor 488 (10 μM, Life Technologies) in the recording pipette solution. Data were acquired using a dual EPC10 amplifier (HEKA) and analyzed offline using the IgorPro software (Wavemetrics). We conducted control experiments in slices obtained from the same brain but not injected with MNPs or injected with the MNPs but not subjected to the magnetic field.

3.2.5 Calcium imaging

Following the post-slicing recuperation period, slices were transferred to a 30 mm Milicell culture dish insert (Millipore Corp, Billerica, Ma) containing 5 mL of normal oxygenated ACSF with 5 μM freshly prepared Fluo-4 AM Pluronic Acid F-127 20% solution in DMSO (Molecular Probes, Life Technologies). Slices were submerged in the dye for 20 minutes then transferred to a submerged recording chamber mounted on the stage of an Olympus BX51 microscope for acquisition.

We visualized labeled slices using epifluorescence illumination and a × 40 water immersion objective. Illumination was achieved using an OPTOLED green LED (exciter 488 nm center wavelength, Chroma; Cairn Research LTD), emitted light was collected by an ORCA-Flash4.0 V2 sCMOS camera (Hamamatsu), and images were recorded using the HCimage software (Hamamatsu). Imaging analysis was performed offline using the ImageJ and IgorPro (Wavemetrics) softwares. (*S*)-1-Aminopropane-1,3-dicarboxylic acid (Glutamate) was prepared from a stock solution and added to the bathing solution. The calcium indicator, Fluo-4 AM (Molecular Probes, Life Technologies), was excited at a wavelength of ~ 490 nm and the resulting emission detected at ~ 520 nm. The optical recording data are shown as the ratio of the change in fluorescence caused by glutamate in cells after 60 seconds to the baseline fluorescence ($\Delta f/f_0$) for the indicated regions of interest.

3.2.6 Immunohistochemistry

The ex-vivo brain tissue slices from ChAT-tau-GFP mice were analyzed using immunohistochemistry after magnetic field induced MNP motion. The nerve fibers in the slices were visualized using anti-GFP immunostaining to assess any damage caused due to MNP movement. The slices were extracted as above, injected with MNPs in the main olfactory bulb, and exposed to a uniform magnetic field in two different directions as described in the previous section. The slices were then fixed in 4% paraformaldehyde for 5 minutes, transferred to saline solution at 4º C, and then quickly washed with 1X PBS for 2 minutes. The slices were then incubated with the blocker (10% Donkey serum in PBS-T) for 1 hour, followed by incubation with the primary antibody in 2.5% Donkey serum in PBS-T overnight at room temperature. The slices were then washed once in PBS-T and then 7X for 5 minutes each in PBS-T and incubated in the secondary Alexa-488 antibody solution (1:750 concentration) for 2 hours at room temperature. The slices were washed 3X for 5 minutes in PBS-T, then further rinsed 3X for 5 minutes each in PBS. At this point, immunostained slices were visualized using confocal microscopy with appropriate fluorescence filters for the MNPs and the GFP-stained fibers.

3.3 Results

The MNPs were analyzed using dynamic light scattering to calculate the particle size distribution and the extent of polydispersity. The mean hydrodynamic diameter of the samples was measured to be 274.6 ± 40 nm (n = 3 samples) with a polydispersity index of 2%. The distribution of hydrodynamic diameter in the samples is shown in

Figure 10A. The magnetization of the particles was measured using the vibrating sample magnetometer for different field intensities and the hysteresis curve for the MNPs is shown in Figure 10B. The saturation magnetization of the particles was calculated to be 0.06 emu at a saturating magnetic field of 0.5 T. The magnetic susceptibility of the nanoparticles was calculated from the M vs H plot and was found to be χ_m = 15.2. Based on these measurements, the MNPs exhibited superparamagnetic behavior and were confirmed to be monodispersed.

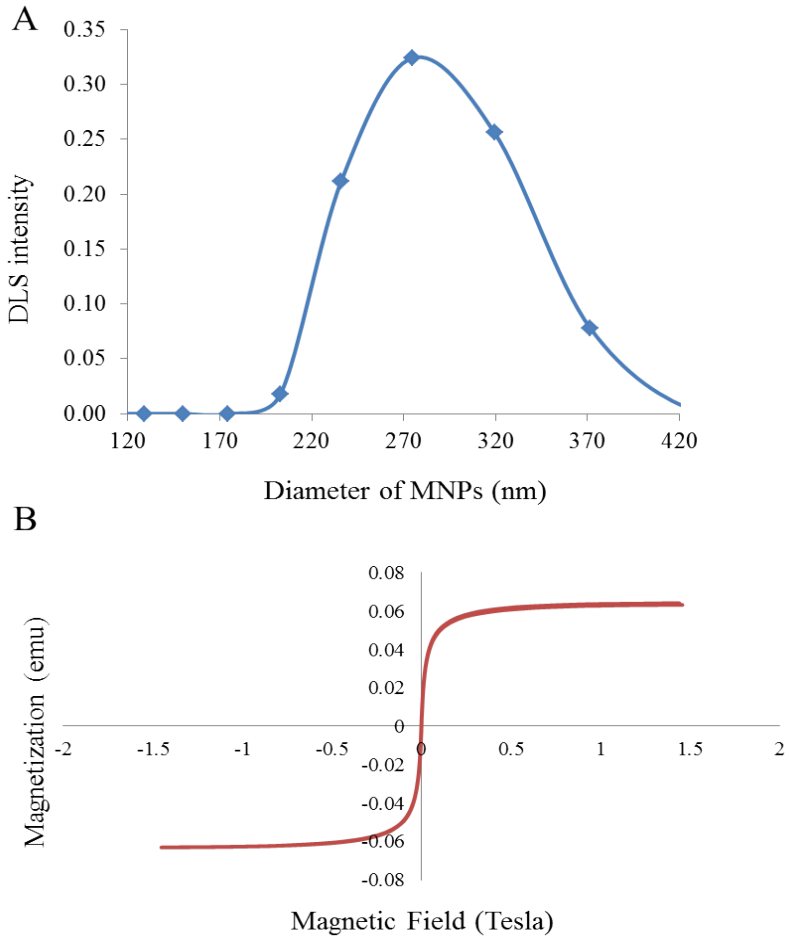

Figure 10 : (A) The distribution of hydrodynamic diameter of the MNPs measured using dynamic light scattering. (B) The magnetization versus magnetic field intensity profile of MNPs measured using vibrating sample magnetometry.

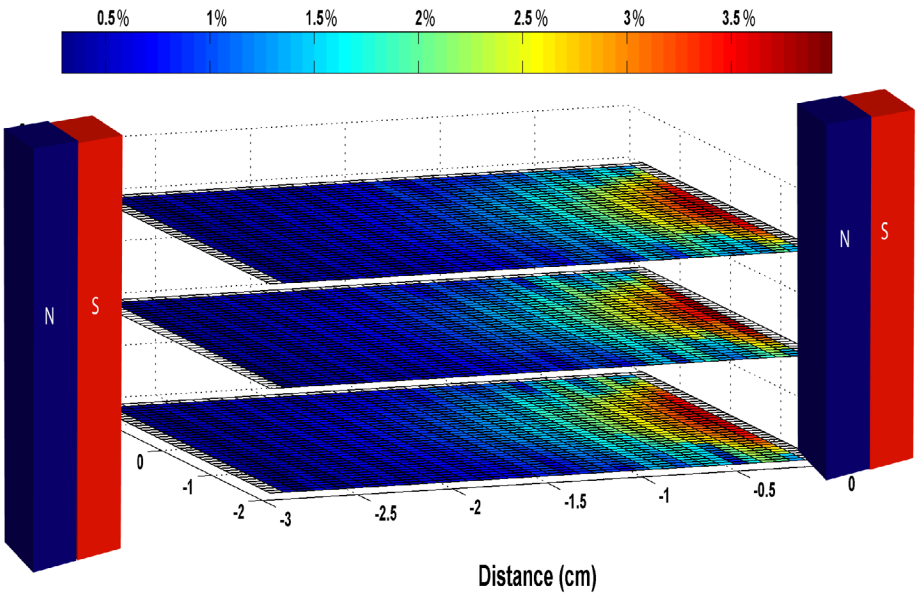

Figure 11: The deviation of magnetic field intensity from the mean value in the region between the two magnets. The two magnet-system produces a uniform field with less than 1.0% variation in the region occupied by the tissue (represented by yellow dotted lines).

The characterized MNPs were injected in rat brain tissue and exposed to a uniform magnetic field as shown in Figure 12A. These ex-vivo cortical slices were maintained at a low temperature in order to preserve structure and extend sample viability. Prior to applying a magnetic field, it was observed that the MNPs diffused in random directions in the tissue. However, when the uniform field was applied to the tissue using the two magnet system (Figure 12B), each magnetized MNP produced a magnetic field of influence around it. An MNP falling in the field of influence of any neighboring MNP experiences an attractive magnetic force towards its neighbor[186]. This attractive force between particles causes the motion of MNPs towards their neighbors. The interactive motion of MNPs in the presence of a uniform magnetic field resulted in the formation of MNP chains in the prepared rat brain tissue. Figure

12C shows a representative image of this chaining of MNPs in a mouse brain tissue (GFP line) after the application of magnetic field. The MNP chains increased in size over time as new particles were recruited to the chain and as the corresponding region of the magnetic field of influence grew larger. The phenomena of movement and agglomeration of MNPs into chains in the brain tissue was observed in all the tissue slices from different rats (n=12).

The motion of MNPs in brain tissue was further evaluated after varying two key parameters in the above experiment, namely, magnetic field intensity and MNP volume concentration. The experiments were performed in brain tissue slices combining either high (0.1 T) or low (0.02 T) uniform magnetic field intensity with either high (0.5 mg/mL) or low (0.05 mg/mL) MNP concentration. Each of these four experiments was repeated over three slices from different rats. In 3 out of the 4 experiments, MNPs formed chains in the presence of a uniform magnetic field while in one case, at the combined low magnetic field and low magnetic concentration, the MNPs were too far apart and the magnetic field was too small to produce any chaining. Table 9 shows a comparison of the extent of chaining observed for each combination of parameters. The amount of chaining for each of the experiments was defined by the average MNP chain length observed in the tissue after 10 minutes of applying the uniform magnetic field. As anticipated, the largest MNP chaining was observed for a combination of high magnetic field and high magnetic concentration (12.51 ± 3.5 μm). In addition, the chain length observed in a high magnetic field and low MNP concentration (5.84 ± 1.1 μm) was higher than observed for the case of a

low magnetic field and a high MNP concentration (2.76 ± 0.8 µm). This indicated a dominant effect of magnetic field intensity over the MNP concentration in the process of MNP movement and chaining.

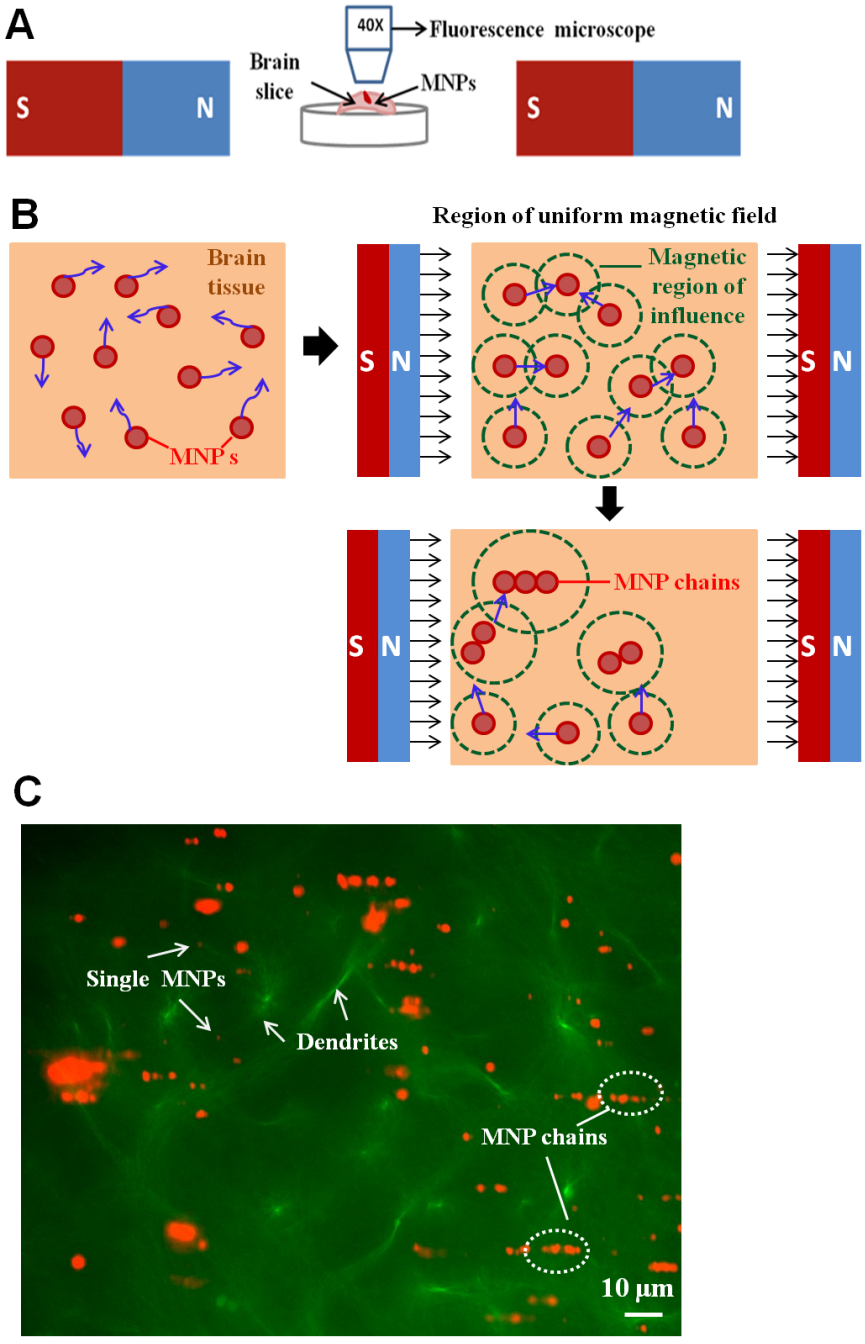

Figure 12: (A) The diagram of two-magnet setup used to study movement of MNPs in brain tissue. The tissue loaded with MNPs was mounted and visualized under a fluorescent microscope after exposing it to the uniform magnetic field (B) An illustration of how MNPs behave in brain tissue with

and without an applied uniform magnetic field. The MNPs diffuse in different directions (blue arrows) in the absence of a uniform magnetic field (left, top). After the introduction of the magnetic field, the MNPs move towards each other due to an overlap of induced magnetic fields of influence (green circles). As a result, the MNPs form chains as they move towards each other and longer chains have a larger field of influence which recruits additional particles to the chain (bottom). (C) Chaining of MNPs experimentally observed in mouse brain tissue (pre-frontal cortex region) in the presence of a uniform magnetic field. The MNP chains (orange) and single MNPs are enclosed by white ovals and white dotted circles respectively. The dendrites (green) in the tissue are indicated by white arrows.

MNP Concentration / Magnetic Field	High Concentration (0.5 mg/mL)	Low Concentration (0.05 mg/mL)
High field (0.1 T)	12.51 ± 3.5 μm	5.84 ± 1.1 μm
Low field (0.02 T)	2.76 ± 0.8 μm	No Chaining

Table 9 : Average chain length after 10 minutes for different applied magnetic field intensity and MNP concentration combinations in rat brain tissue.

To determine the functionality of cells after moving MNPs through or near them, we performed standard electrophysiology recordings in the neurons of the olfactory bulb[187,188]. Mitral cells from the main olfactory bulb were targeted for whole-cell recordings, after moving MNPs through a region that contained those cells. In these experiments the recording pipette contained a fluorescent dye (see methods), which allowed us to visually verify the integrity of the recorded neuron. As shown in Figure 13*B*, following the movement of MNPs, mitral cells remain excitable as determined by current injections, indicating that basic processes such as influx and efflux of sodium and potassium ions [189] respectively were unaffected by the motion of MNPs. The motion of MNPs did not alter the dependence of neuron firing frequency for different constant currents injected into the cells (Figure 13C). Additionally, we tested synaptic functionality by examining the occurrence of spontaneous inhibitory

post-synaptic currents (sIPSCs) in mitral cells. Previously, it has been shown that noradrenaline, a neuromodulatory transmitter, enhances the release of gamma-Aminobutyric acid (GABA) from granule cells in the main olfactory bulb, and greatly enhances the frequency of spontaneous inhibitory post-synaptic currents in mitral cells[190]. As shown in Figure 14B, slices exposed to noradrenaline (NA, 10 uM, for 3 minutes) after MNP motion showed a significant increase in spontaneous inhibitory post-synaptic current frequency, suggesting that the synaptic connectivity between granule and mitral cells in the main olfactory bulb remained functional.

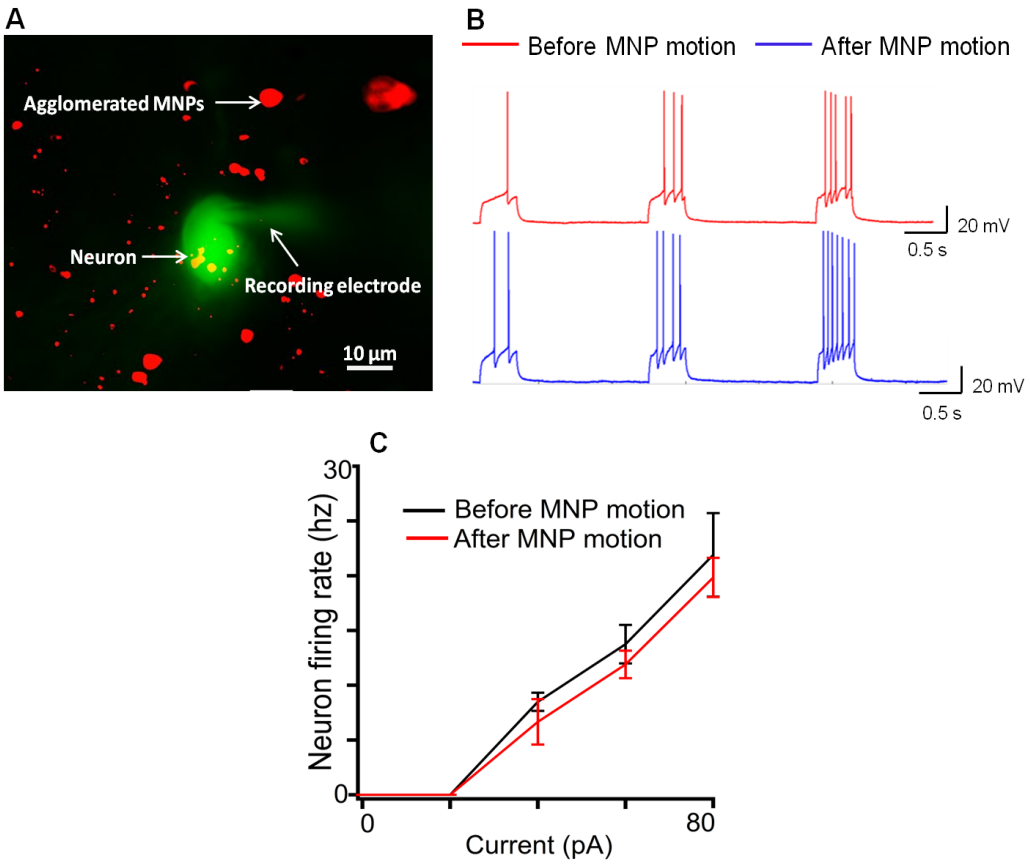

Figure 13: Functional health of brain tissue after MNP motion. (A) Recording from a mitral cell in the olfactory bulb after the slices treated with MNPs were subjected to a magnetic field. The recording electrode contained the fluorescent dye Alexa-488 (green), which diffuses into the neuron during the recording. The MNPs contained a fluorophore Texas-Red (red). Note this is a total summed two wavelength images (B). Current-clamp recordings in mitral cells before (red) and after magnet induced MNP movement (blue). Increasing depolarizing current pulses (not shown) elicited action potentials in both control and treated neurons. (C) In the range of depolarizing current used, the frequency of

neuronal firing increased linearly and it was comparable for different constant current stimuli before (black) and after MNP motion (red).

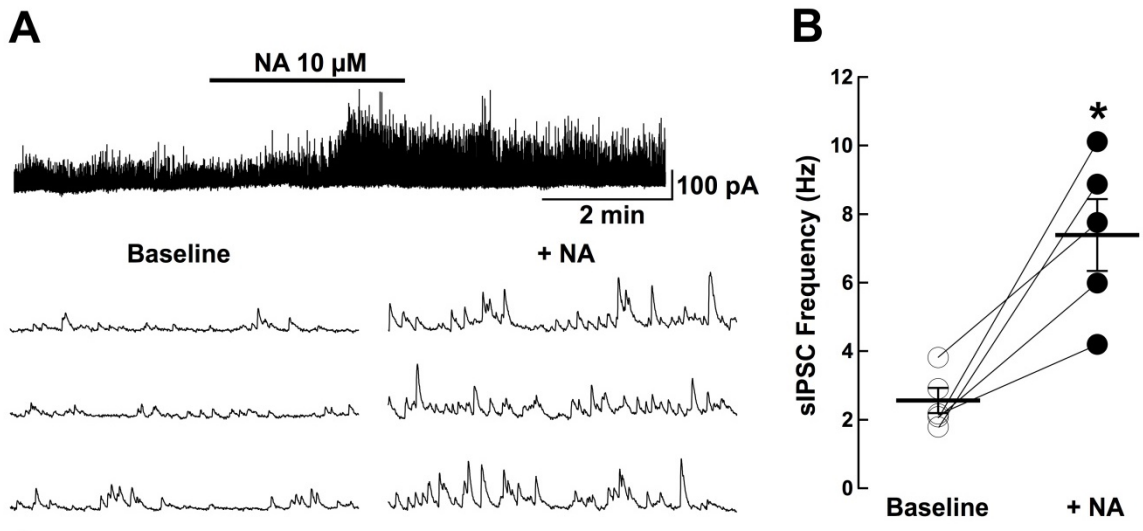

Figure 14: Synaptic connectivity in the olfactory bulb after MNP motion (A) Recording from a mitral cell showing the spontaneous occurrence of GABA IPSCs after MNP motion in brain slices. Top, application of noradrenaline (NA, 10 µM, 3 min) produced a long lasting increase in sIPSC frequency in this cell. Bottom, select traces from above, in an expanded time scale, showing sIPSC before (left) and after NA (right). (B) NA significantly increased the sIPSC frequency; baseline, 2.56 ± 0.82 Hz, NA, 7.39 ± 2.34 Hz (*, $p<0.003$; $n = 5$). The observed increase in sIPSC frequency caused by NA after MNP motion is similar to the trend observed previously by Zimnik et al. [190]

Next, we assessed whether the magnetically induced movement of MNPs disrupted the neural circuit function in the olfactory bulb. The olfactory bulb has a well-characterized neural circuit in which sensory inputs excite principal neurons, specifically the mitral/tufted cells[191]. Activation of mitral cells then excites the surrounding granule cells at dendrodendritic synapses. Thus, by monitoring the granule cells after MNP movement, we studied the effect of MNP motion on the excitatory synapses in the olfactory bulb [191]. To investigate olfactory bulb neural circuit function, we loaded olfactory bulb slices with a Ca^{2+} sensing dye (Fluo-4 AM dye, 5 µM, see Methods) to visualize and monitor the neural activity of the circuit, in particular granule cells (the most abundant neuron in the olfactory bulb) (Figure

15B). Fluo-4 dye AM is a cell permeable dye that exhibits an increase in fluorescence upon binding to Ca^{2+} (indicating neural activation), and allows for the monitoring of a large number of neurons simultaneously. MNPs were applied to the slice 30 minutes before the acquisition of images began and they were moved by exposure to a uniform magnetic field. We then assessed the responsiveness of granule cells to activation by the excitatory neurotransmitter glutamate after MNP movement in the region. As shown in Figure 15B, following the movement of MNPs in the slice, granule cells show normal fluorescence labeling suggesting that the overall morphology is maintained. In these slices, application of glutamate (100 µM) resulted in a robust increase in intracellular Ca^{2+} as evidenced by the changes in $\Delta F/F_0$ (45.25± 8.2%, n= 6 cells). Hence the responses to excitatory stimuli in granule cells were not affected by the MNP movement in the region.

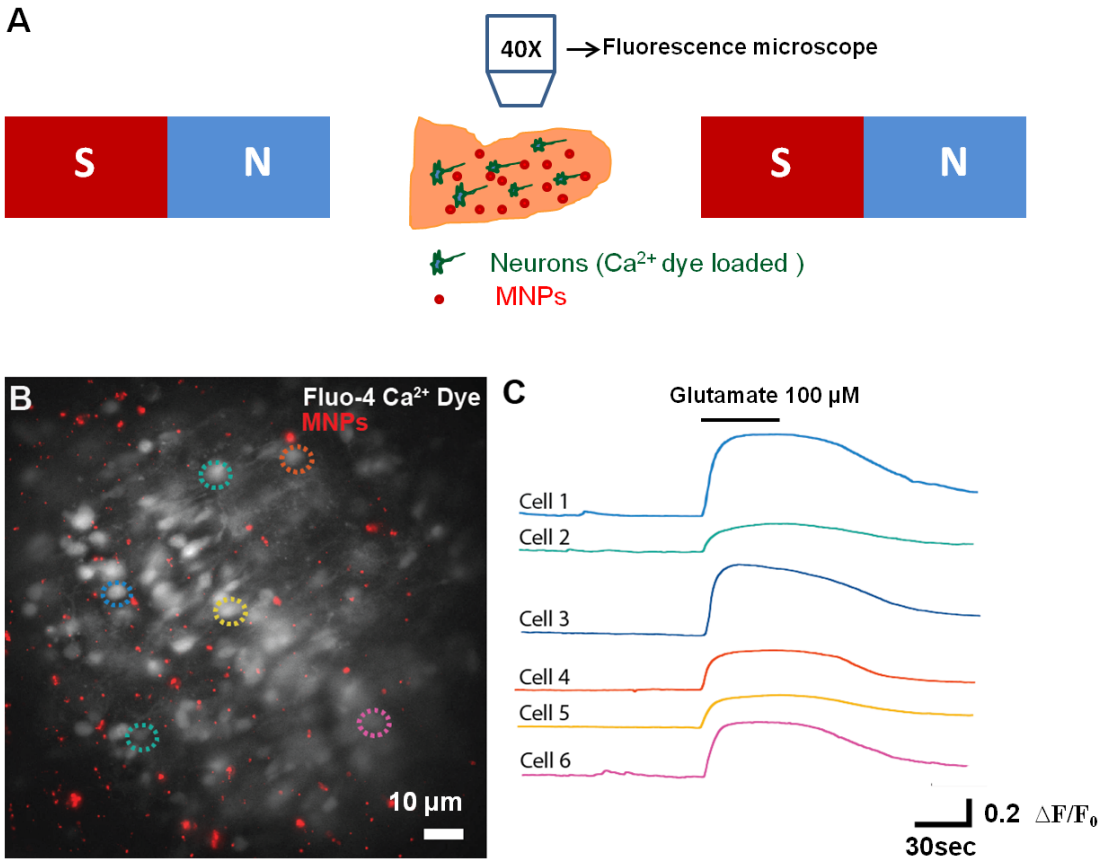

Figure 15: Calcium imaging recording in brain slices after MNP motion. (A) Experimental setup used for the calcium imaging experiments. After loading the calcium dye, MNPs are placed on the slice and subjected to a magnetic field. (B) Fluorescence image showing a network of functionally active neurons in a brain slice loaded with the calcium dye Fluo-4 AM (white) and MNPs (red), after exposing the slice loaded with MNPs to a uniform magnetic field. Dotted colored circles represent the neurons used for quantification of fluorescence changes shown on the right. (C) Optical fluorescence recordings of the selected cells shown in B. Images were taken at a rate of 1 Hz FPS. Application of the excitatory neurotransmitter, glutamate (100 µM, 45 seconds) resulted in a large, and reversible, increase in intracellular calcium levels. The color of each plot corresponds to cells indicated by the colored dotted circles in (B).

To further determine whether the movement of MNPs disrupted neural connections, we used transgenic mice (ChAT Tau-GFP) that expressed GFP under the promoter of choline acetyl transferase (ChAT), an enzyme involved in the synthesis of acetylcholine. Since the main olfactory bulb receives a rich cholinergic projection from the basal forebrain[192], we visualized the effect of MNPs on the fibers in this

particular region. The slices used in these experiments were divided into three main categories: treated, untreated, and control. The treated slices were injected with MNPs and were subjected to the applied uniform magnetic field for 5 minutes, followed by a rotation of the field for 5 minutes as explained in the Methods section. The untreated slices were just injected with MNPs and no magnetic field was applied. The control slices contained no MNPs and no magnetic field was applied. As shown in Figure 16, immunostaining of GFP in control mice samples (Figure 16, left) revealed abundant fibers throughout the different cellular layers of the main olfactory bulb. The untreated (Figure 16, middle) and treated slices (Figure 16, right) showed no difference in the pattern of distribution of GFP-positive fibers. Hence the motion or presence of MNPs did not disrupt the neural connections in the brain independent of the direction of MNP motion.

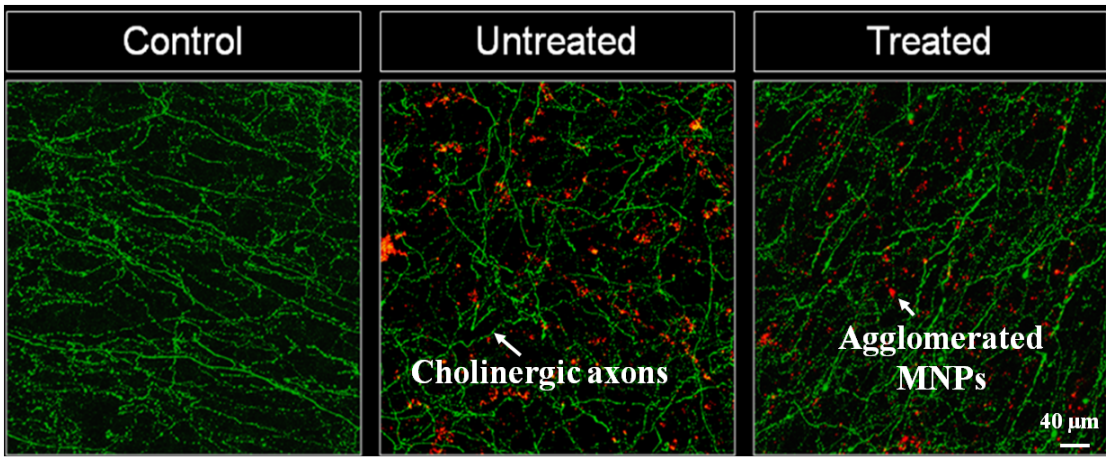

Figure 16: Confocal microscopy images of the granular cell layer in the main olfactory bulb from ChAT-Tau-GFP mice, after immunostaining for GFP. In control conditions (left) the slices show abundant distribution of GFP labelled fibers, corresponding to the axonal processes of cholinergic neurons. The pattern of distribution of axonal fibers was not affected in slices treated with MNPs without application of the magnetic field (middle) or after the MNPs exhibited motion into chains under an applied uniform magnetic field (right).

3.4 Conclusions

In previous works, MNPs of various sizes, shapes, and coatings have been successfully utilized in drug delivery, gene transfection, tumor imaging, and regenerative medicine [55,177,193,194,195,]. In principle, such MNPs can be controlled in the human body using external magnet systems to direct drugs and other biological factors to specific targets. Here we examined the motion of MNPs in brain tissue, to investigate both the character of MNP motion in the brain and its safety. We showed that monodispersed starch-coated MNPs are able to move towards each other in brain tissue when exposed to a uniform magnetic field and, importantly, that this movement produced no apparent disruption of the neural circuit function in the main olfactory bulb.

We observed that the MNPs agglomerated into chain like structures as they moved in the brain tissue under the influence of a uniform magnetic field. Such an agglomeration of MNPs in a uniform magnetic field has been previously studied in various media such as in water, bovine serum albumin and sodium dodecyl sulphate [196,197,186]. The dynamics of chain formation and the distribution of chain length have been modeled and compared with experiments[197,198,199]. Based on these prior studies, the mechanism of chain formation can be classified into two main cases: diffusion dominated and magnetic drift dominated agglomeration. In diffusion dominated agglomeration, the MNPs undergo diffusion in the media until they are close enough so that they bring each other together by the magnetic forces between them[200,201,202]. In the drift dominated agglomeration, the magnetic force has a sufficiently long range

that it drives the motion of MNPs together from the start [203,204,205]. In our experiments in brain tissue, the average chain length of MNPs was higher in a high magnetic field and low MNP concentration than in a low magnetic field and high concentration condition. This indicates that a high magnetic field intensity can bring even sparsely distributed nanoparticles together. Thus for our experimental conditions, the MNPs exhibit a magnetic drift dominated mechanism of agglomeration as they moved in brain tissue.

The MNPs used in this work have been shown to not produce cytotoxicity in various cell types and in-vivo studies[174,206,207]. However, it is equally important to study and ascertain that the motion of these nanoparticles in brain tissue does not affect the normal function of neurons or their connectivity. By taking electrophysiological recordings of neurons before and after MNP movement, we have shown that the MNP motion and chaining did not affect neural functionality. Current injections produced a robust depolarization in the neurons, and they exhibited a stimulus-dependent increase in firing when a constant current stimulus was provided to the cell. Importantly, the change in neural firing rate elicited by incremental current stimuli was not affected by the MNP motion. Therefore, we conclude that MNP presence, motion, or chaining did not affect the physiological properties of the neurons.

In addition, we showed that the movement of MNPs did not affect the inhibitory neural circuit in the olfactory bulb; a critical component of olfactory processing in the bulb. The frequency and amplitude of the GABA sIPSCs after movement of the

MNPs was similar to the previously reported values [190]. Further, since the sIPSCs recorded in the mitral cells are produced by the summation of multiple synapses from several interneuron types, these results suggest that circuit level basal release from interneurons and post synaptic mitral cells activation were not affected following MNP motion. Furthermore, noradrenaline caused a robust increase in the spontaneous inhibitory post-synaptic current frequency in mitral cells, suggesting that the overall functionality of interneurons was also not affected by the MNPs movement (see also [190]). This conclusion was further supported by the analysis of excitatory glutamatergic responses in a population of granule cells using a calcium indicator. In these optical recordings we found that a wide field of granule cells showed an increase in fluorescence after exposure to glutamate despite MNP motion in the same region. The increase in fluorescence corresponds to an increase in intracellular calcium ions in the granule cells, in response to the glutamate-induced excitation. Together, these results provide evidence that excitatory and inhibitory responses of the olfactory bulb neural network were not affected by the MNP movement.

Apart from the functional health of the neurons, the immunohistochemistry experiments suggested that the MNPs did not disrupt the fibers as they moved and chained in the tissue. The slices containing MNPs (both with and without an applied uniform magnetic field) did not exhibit any noticeable difference in the density of cholinergic fibers in the granule cell layer, compared to the control slices with no MNPs and no applied magnetic field. These experiments ruled out the possibility that

the passive diffusion or magnetically induced movement of MNPs disrupted neural connections.

In summary, we have shown that MNPs can move towards each other in brain tissue under an applied uniform magnetic field. This motion of MNPs results in the formation of chain like agglomerates in the tissue and for our experimental conditions this chaining was determined to be drift dominated (as opposed to diffusion dominated) behavior. We found that the chained MNP agglomerates did not affect the normal functioning of neurons in the main olfactory bulb. The MNP agglomerates also did not disrupt the dense connections between the neurons in this region. Since it is known that MNP chaining, and the resulting ability for magnetic fields to effective move MNP through tissue[208,209,210] depends on particle properties (size, shape, concentration), in the future the studies above could be expanded to select optimal MNP properties to enable effective but safe MNP motion in the brain. Enabling safe and effective manipulation of MNPs in the brain would aid drug and gene delivery and other tissue engineering applications in the brain.

Chapter 4: Magnetic steroid targeting to the inner ear to reduce cisplatin induced ototoxicity

4.1 Background

Cisplatin (cis-diamminedichloroplatinum) and other platinum based drugs are the antineoplastic drugs of choice for various genitourinary cancers, certain forms of breast cancers, and as radiosensitizers for most head and neck cancers. However, these platinum-based drugs are very toxic to the kidneys [211], the inner ear [212], and sometimes the peripheral nervous system [213]. While the nephrotoxicity may be mitigated by hyper-hydrating patients in the hours before and during cisplatin injections, addressing ototoxicity in cisplatin-treated patients remains an unmet medical need.

Cisplatin induced hearing loss occurs in adults with an average incidence of 62% [214]. Among pediatric patients, significant sensorineural hearing loss is observed in 90.5% of patients at 8 kHz [215]. The ototoxic effect of cisplatin is noticeable, with hearing loss within hours or days after the first cisplatin injection [216]. It is also cumulative, and the cumulative effect implies particular vulnerability in pediatric populations as repeated treatments, even separated by years, eventually lead to complete hearing loss, which may in turn lead to pervasive developmental delays including speech, cognitive and social developmental challenges.

The molecular mechanisms underlying the ototoxicity of cisplatin remain under debate. The various mechanisms include generation of reactive oxygen species and the depletion of antioxidant enzymes such as superoxide dismutase [217], catalase, glutathione peroxidase and glutathione reductase [216]. Overall, cisplatin causes damage to the organ of Corti, the stria vascularis and spiral ganglion cells, possibly through different molecular mechanisms [218,219].

Steroids have been shown to reduce cisplatin-induced hearing loss, presumably by counteracting the effect of the reactive oxygen species induced by cisplatin administration [214,220]. Though commonly used, steroids interfere with cisplatin's efficacy and prolonged use of systemic steroids is undesirable due to additive toxicities [221–224]. Thus it has been proposed that local administration of steroids into the middle ear, subsequently diffusing into the cochlea via the round window membrane at the base of the cochlea, could be used to protect hearing. However, administration of a liquid steroid into the middle ear results in a rapid elimination of the drug from the cochlea as well as a very steep drug gradient from the base to the apex of the cochlea [77,225]. The liquid formulation in the middle ear is also rapidly eliminated via the Eustachian tube as soon as the patient stands up and swallows.

In prior animal studies we showed that application of our magnetic injection device could be used to direct drug-eluting bio-compatible nanoparticles from the middle ear to the inner ear. Once inside the inner ear, the drug payload is released from the nanoparticles, providing a significant therapeutic effect [226,227]. In this paper, we show

that magnetic steroid delivery to the inner ear can be used to protect hearing in mice receiving systemic cisplatin regimens. Previously both dexamethasone and prednisolone had been used for their otoprotective effect against cisplatin [214,228]. Due to an ability to more effectively load the magnetic particles with prednisolone than dexamethasone, we employed prednisolone-loaded magnetic nanoparticles deposited intra-tympanically into the middle ear, and then applied a magnetic field that transported the nanoparticles through the window membranes into the inner ear where they released the steroid in therapeutic amounts. In the mouse model employed in this study, this steroid delivery method effectively mitigated the cisplatin-induced rise in hearing threshold of the animals at high frequencies and protected the outer hair cells in the basal cochlear region from the ototoxic effect of cisplatin.

4.2 Methods

4.2.1 Animals

The study was conducted on CBA/CAJ mice (10 weeks old) of both sexes (23-27 gm body weight) from the Jackson Laboratory (Bar Harbor, ME). All animal studies were conducted in accordance with the policies and recommendations of the National Institute of Health Guide for the Care and Use of Laboratory Animals, and under approval from the Institutional Animal Care and Use Committee of the University of Maryland.

4.2.2 Anesthesia

The mice were anaesthetized via intraperitoneal injections of ketamine 100 mg/kg and xylazine 20 mg/kg supplemented as necessary and were placed on a warming pad (Deltaphase isothermal pad, Braintree Scientific, MA) to maintain body temperature at 37 °C.

4.2.3 Study design

The overall study design is shown in Table 10. We used the mouse cisplatin administration protocol [229], which involves multiple cisplatin cycles spread over time (as is the case for patients), which reliably elicits hearing loss but leads to less than 10% animal mortality. Hearing of all mice was first tested by auditory brainstem response (ABR) measurements. Then, all mice were pre-hydrated with two subcutaneous doses of 1 mL of sterile normal saline separated by 8 hours (Hospira, IL), 24 hours before starting each cisplatin cycle, to protect their kidneys against nephrotoxicity. Cisplatin was administered intraperitoneally at 4 mg/kg daily for 4 days on and 10 days off (14-day cycles for the first 2 cycles) plus a 16-day (3^{rd}) cycle (2 days on and 14 days off) (Table 10). During the recovery periods, the animals were hydrated with 1 mL of normal saline twice per day for 5 days or more based on animal's weight and health. After the third cycle, hearing was measured by post-treatment ABR. Then the mice were sacrificed and prepared for cytocochleograms as described below.

	Group A : Saline control	Group B : Intra-tympanic methyl-prednisolone	Group C: Magnetic delivery of prednisolone
Number of animals	N = 6	N = 6	N = 6
Day 0	Pre-treatment auditory brainstem response recording		
Day 1 - 4	4 mg/kg of cisplatin per day	4 mg/kg of cisplatin per day	4 mg/kg of cisplatin per day
Day 5 - 14	Recovery period with 2 mL/day of subcutaneous saline injection		
Day 15	Left ear saline injection	Left ear methyl-prednisolone injection	Left ear nanoparticle injection + magnet exposure for 20 mins
Day 16 - 19	4 mg/kg of cisplatin per day	4 mg/kg of cisplatin per day	4 mg/kg of cisplatin per day
Day 20 - 29	Recovery period with 2 mL/day of subcutaneous saline injection		
Day 30	Left ear saline injection	Left ear methyl-prednisolone injection	Left ear nanoparticle injection + magnet exposure for 20 mins
Day 31 - 32	4 mg/kg of cisplatin per day	4 mg/kg of cisplatin per day	4 mg/kg of cisplatin per day
Day 33 - 46	Recovery period with 2 mL/day of subcutaneous saline injection		
Day 47	Post-treatment auditory brainstem response recording		
Day 50	Termination and cochlear preparations		

Table 10 : Animal groups and schedule for our cisplatin and ear treatment study.

The animals were divided into three different groups, with N = 6 mice per group. Six mice per group attained a statistically significant p value of < 0.05 for protection of high frequency hearing. For all groups, ear treatment was administered one day before the second and third cisplatin cycles respectively. Group A mice received 1.8 µL of intra-tympanic saline into their left ears. Group B mice received 1.8 µL of intra-tympanic methylprednisolone (Pharmacia&Upjohn, NJ) into their left ears. Group C mice received 1.8 µL of 300 nm diameter magnetic nanoparticles into their left ears. These particles were loaded with prednisolone sodium phosphate at a concentration

of 82 µg/mL, and labeled with Texas red fluorescent dye for easy visualization in tissue samples (Chemicell, Berlin, Germany). A 0.5 Tesla magnet (5 × 2.5 × 2.5 cm, K&J Magnetics, PA) was then placed contralateral near the right eye of each animal in group C for 20 minutes to pull the nanoparticles from the middle ear into the inner ear. For all animals in all groups, the right ears remained as untreated same-animal controls.

4.2.4 Auditory brainstem response

The hearing thresholds of the animals in all groups were measured by performing auditory brain stem response (ABR) assays before and after the cisplatin treatment and recovery periods. The mice were anesthetized and placed inside a sound booth (Industrial Acoustics, NY). Two recording electrodes (RLSND110-1.5, Rhythmlink International) were inserted postero-ventral to the auricular area of the left and right ears. A reference electrode was placed at the apex of the head. A ground reference electrode was placed subcutaneously in the lumbar area. Using our ABR recording system (Tucker Davis Technologies, FL), the animals were then presented in free field with 600 sweeps of 5 ms long bursts (shaped with 1 ms onset and offset sinusoidal ramps) at varying intensities beginning at a 94 dB sound pressure level (SPL) and proceeding in 5 dB decrements down to a 14 dB SPL. The electrophysiological signals were recorded for 10 milliseconds. These cycles of sound intensities were repeated for different sound frequencies (8 kHz, 16 kHz, and 32 kHz). Hearing threshold at each frequency was determined as the lowest intensity at which a definite cochlear response could be identified (waves I&II). Figure 17B

shows sample traces at 16 KHz for various SPLs and the corresponding hearing threshold. The percentage hearing loss of each animal at a specific frequency was defined as the ratio of the change in thresholds after the treatment compared to pre-treatment thresholds. Hence 0% represents no loss in hearing at that frequency (pre and post hearing thresholds were identical), while 100% represents no measurable response or a measurable response only at the highest sound pressure level of 94 dB.

4.2.5 Cytocochleogram

The cochleas from the different groups were dissected to study the pathophysiology of the cisplatin treatment on the organ of Corti, as well as any effect of the otoprotective treatments. The animals were euthanized using carbon dioxide and the cochleas rapidly isolated. The cochleas were continuously perfused with ice cold 4% paraformaldehyde into the round window membrane and out of a small hole pierced in the apex of the cochlea, and then placed in paraformaldehyde overnight at 4 $^{\circ}$C. This was followed by 3X wash with 1X PBS at pH 7.4 and decalcification in 0.5M EDTA for 3-4 days. After washing the cochleas three times using 1X PBS, they were micro-dissected into three turns (Basal, Middle, Apical) using an ophthalmic knife (MANI Ophthalmics, Tochigi, Japan). The tectorial membrane was removed. Cochlear outer and inner hair cell layers were stained using Alexa Fluor 488 Phalloidin (1:800 in 1X PBS + 0.5% Tween, Life Technologies) for 45 minutes. The turns were mounted on a glass slide using Fluoromount-G with DAPI (Electron Microscopy Sciences). Images of each cochlear turn were taken at 40X magnification using an LSM 710 confocal microscope (Zeiss) in z-stack mode. The outer hair cells

in these images were counted for the presence of nuclei and cell membranes over a 200 μm distance of the different cochlear turns using Zen 2010 software (Zeiss).

4.3 Results

In our experiments, the hearing thresholds of the animals in the three different groups were determined after the completion of the cisplatin treatment by using ABR assays. The hearing loss experienced by the animal at a particular frequency was determined by the ratio of change in threshold post-treatment to the initial hearing threshold at the same frequency. After systemic cisplatin treatment, this threshold increase is known to occur first at high frequencies, progressing to the lower frequencies as treatment continues, eventually reaching speech frequencies [216,230].

In our study, untreated (right) ears experienced significantly greater hearing loss at high frequency (at 32 kHz) compared to at 16 kHz and 8 kHz (Figure 17A). In contrast, in the treated (left) ears at 32 kHz**,** the magnetic delivery group C ears experienced substantially less hearing loss (53% ± 12%) compared to ears that received saline (group A, 93% ± 7%) or intra-tympanic methylprednisolone (group B, 97% ± 3%). As evident in Figure 17A at 32 kHz, the difference in means between group C and the other groups was much larger than the variance within each group. Our approach therefore achieved a statistically significant reduction in high frequency hearing loss for the magnetically treated group C ears, compared to the untreated and group A and B ears which exhibited almost complete hearing loss at high frequencies ($p^{**} < 0.05$). Overall, the steroid loaded nanoparticles mitigated cisplatin induced

ototoxicity at high frequencies, with 95% statistical significance. At 8 and 16 kHz, magnetic delivery also seemed to reduce the degree of hearing loss, but at these lower frequencies a statistical significance of 95% was not reached, in part because cisplatin caused less hearing loss at these lower frequencies (see 8 and 16 kHz bars in Figure 17A).

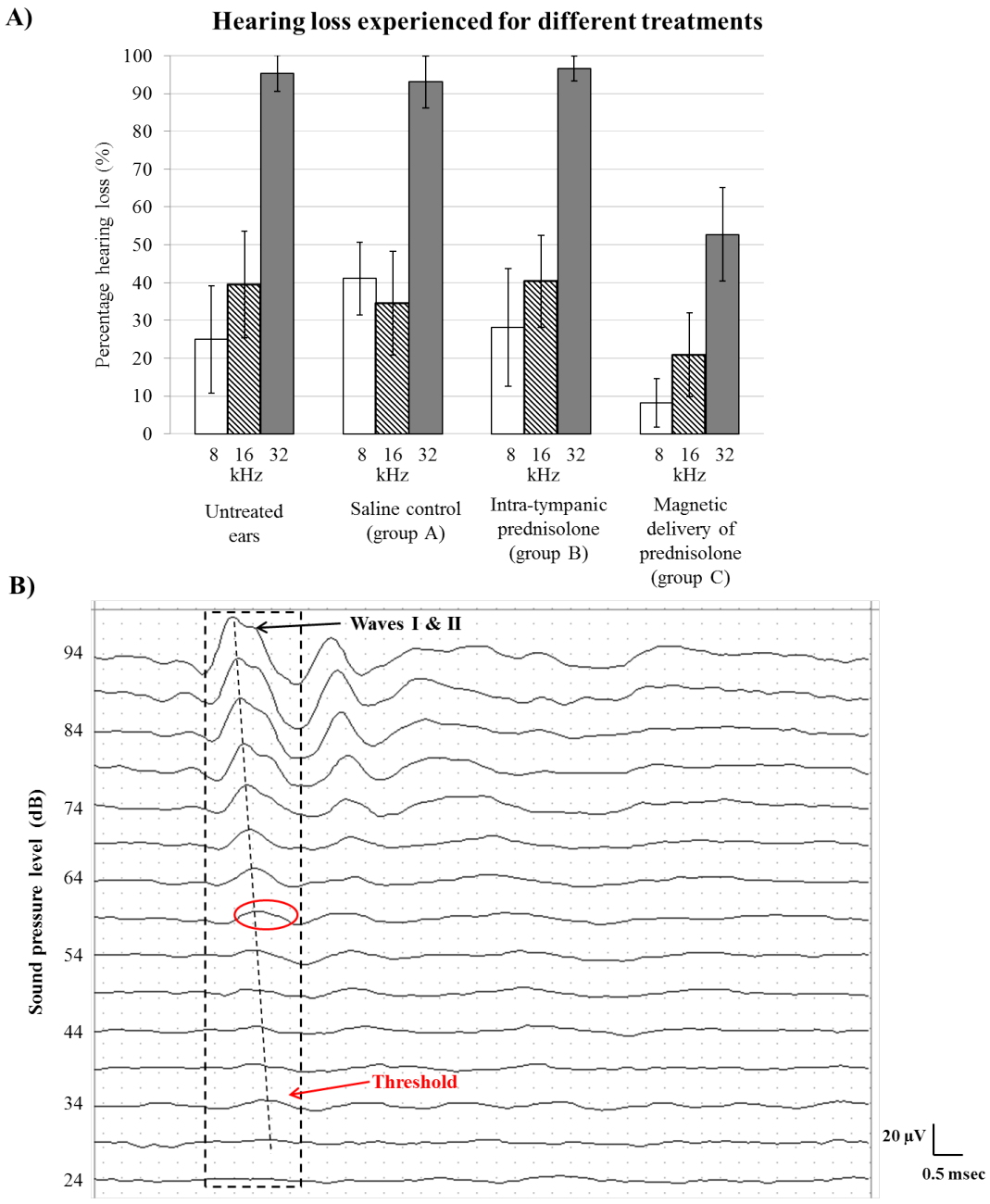

Figure 17: Comparison of hearing loss between the three animal groups for the injected left ears and corresponding untreated right ears (N = 6 for each group). Percent hearing loss at each frequency, per group, is shown. A) Treated ears that received magnetic nanoparticles showed significantly less hearing loss (group A bars) compared to the intra-tympanic methyl-prednisolone group (group B bars, $p^{**} < 0.05$) and the saline control group (group C bars, $p^{**} < 0.05$), especially at high frequency of 32 KHz. Hearing loss remained similar at high frequency across all groups for untreated ears. B) A sample ABR trace containing the waves I and II (dotted black box) at 16 KHz has been shown to demonstrate threshold measurement (note that positive voltage is up, the convention for animal ABRs). The threshold for this animal is at 34 dB beyond which the waves I and II are completely attenuated.

Cisplatin is known to induce apoptosis in the three rows of outer hair cells starting at the outer row and progressing to the inner row [231]. There have also been reports of damage to the inner hair cells of the organ of Corti, cuticular plate and stria vascularis [230]. These ototoxic effects have been consistently shown to progress from the basal, high frequency region of the cochlea to the apical, low frequency region with continuing cisplatin treatment. We extracted cytocochleograms to evaluate the effect of magnetic delivery in protecting hair cells. The cochleas were micro-dissected post-treatment and the organ of Corti examined in the different turns after staining the hair cells. Sample cytocochleograms are shown for the basal cochlear region in Figure 18. Hair cell preservation is evident in the magnetically treated cochlea (Figure 18D, group C) compared to group A (Figure 18B, saline) and group B (Figure 18C, intra-tympanic steroid). Magnetically delivered nanoparticles can be seen among the hair cells in the cochlea (red fluorescence in Figure 18D).

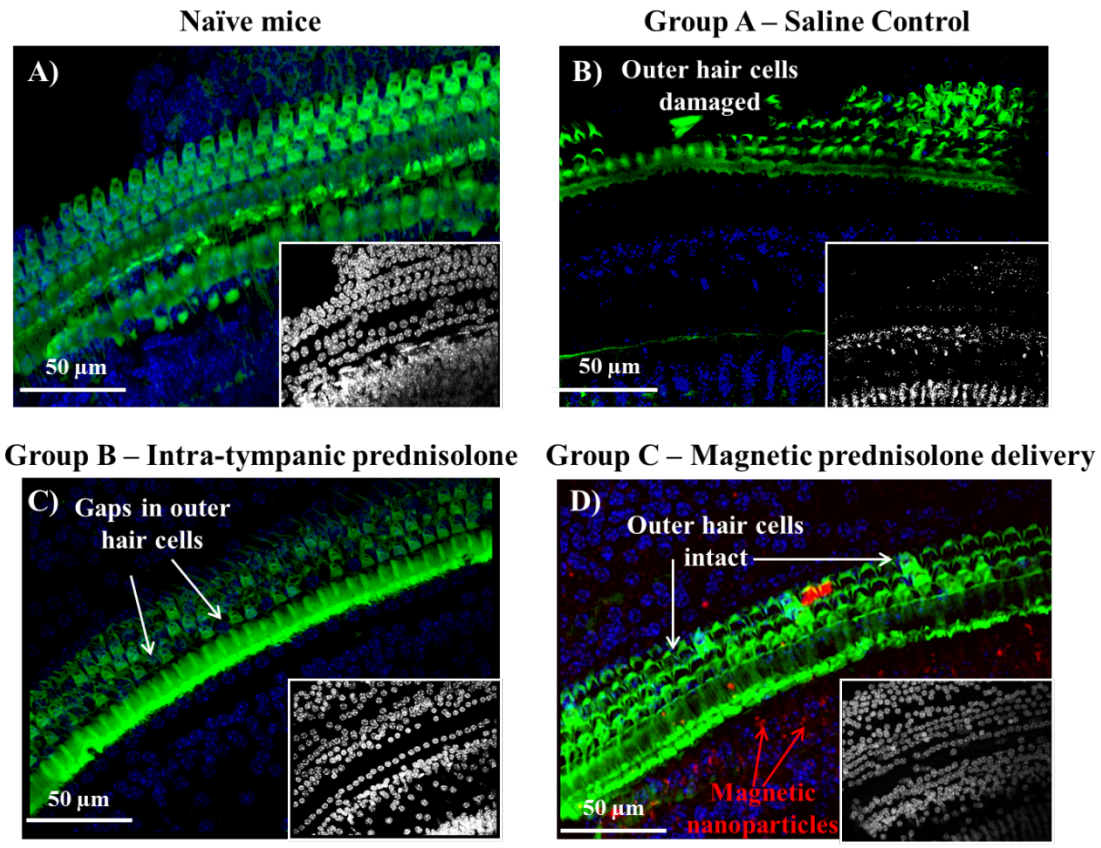

Figure 18: Sample cytocochleograms of the basal cochlear region of different groups. The outer hair cells were stained for actin with Alexa Fluor 488 Phalloidin (green) and the various cell nuclei were stained using DAPI counterstain (blue). A) Left ear from a naïve animal that did not receive any cisplatin treatment or otoprotection. For animals that were administered cisplatin: B) Left ear that received saline; C) Left ear that received intra-tympanic methyl-prednisolone; and D) Left ear that received magnetic steroid delivery. The images of the DAPI stained nuclei for all the groups have been shown in the image insets of A), B), C) and D) correspondingly.

The number of outer hair cells in each cochlear micro-sections was counted and compared between the three groups. The outer hair cell density observed for control animals (no cisplatin and no ear treatments) versus from ears of animals that received cisplatin plus one of the 3 types of ear treatments (group A saline, group B intra-tympanic methylprednisolone, or group C magnetic delivery of prednisolone) is shown in Table 11. A significant decrease in hair cells was observed for the saline group A ears (72% decrease, $p < 0.01$) and intra-tympanic group B ears (33%

decrease, $p < 0.01$). In contrast, cochleas from treated ears in the magnetic delivery group C displayed a small loss of 9% of hair cells in the basal region compared to control (no cisplatin) animals. This indicates that in the magnetic prednisolone delivery group, the outer hair cells in the basal cochlear region were preserved by the magnetic delivery of steroid to the cochlea.

	Naïve mice: no cisplatin or ear treatment	**Treated ears from group A**: cisplatin + intra-tympanic saline	**Treated ears from group B**: cisplatin + intra-tympanic methyl prednisolone	**Treated ears from group C:** cisplatin + magnetic delivery of prednisolone	**Untreated ears from groups A, B, C:** cisplatin, but no ear treatment
Outer hair cell density (number per 200 µm)	75 ± 2	21 ± 5	50 ± 7	68 ± 4	26 ± 9
% decrease in hair cell density	N/A	72%	33%	9%	65%

Table 11: Comparison of outer hair cell density for cochleas in naïve mice (N = 6), versus in mice that received the 3 ear treatment types (N = 6 for each group). The second row lists the percent decrease in hair cell density compared to the no cisplatin naïve group. In the magnetically treated group C, hair cell density decreased by just 9% compared to substantially greater hair loss in all the other groups.

4.4 Discussion

Cisplatin administration is known to be ototoxic, likely by the production of reactive oxygen species in the inner ear and by depletion of the inherent antioxidant system of the cochlea, leading to apoptosis of hair cells in the organ of Corti, spiral ganglion cells, and marginal cells of the stria vascularis [230,231]. Steroids such as dexamethasone and prednisolone are thought to reduce the production of free radicals in the inner ear and decrease the formation of inflammatory molecules and could protect hearing

from cisplatin [214,228,232]. However, prolonged systemic administration of steroids reduces the anti-cancer efficacy of cisplatin and is also undesirable due to added toxicity [221–224,233,234], which has led to studies on local intra-tympanic administration of steroids to protect hearing [234]. Compared to intra-tympanic administration, magnetic forces can better deliver therapy directly to the cochlea and confer a stronger therapeutic effect. In our animal study we observed that magnetic delivery of steroids protected hair cells more effectively and concomitantly reduced the degree of cisplatin-induced hearing loss, compared to no treatment or to intra-tympanic steroid administration.

Chapter 5: Spintronic devices for potential single neuron sensing and activation

A part of this work originally appeared in [235]

5.1 Wireless sensing of local currents

The ability to detect small local currents with high spatial resolution plays an important role in a broad range of applications such as non-destructive testing, industrial electronics, and biosensing. For example, local currents identify the location of defects and malfunctioning circuits in current transformers and complementary metal oxide semiconductor (CMOS) circuits [236,237], detect mechanical defects[238], and sense the concentration of polluting gas byproducts of combustion or automotive emission such as NO_2 and NH_3[239]. In biological systems such as the central nervous system, local currents provide information about nerve and cell activity[240] .The ability to wirelessly detect local currents with high spatial precision is highly desirable for many of these applications. For example, detecting the amplitude and position of currents wirelessly provides information about the activity inside of an organism non-invasively and helps track regions of abnormality[241,242]. In electronic circuits, wireless inspection of defects enables diagnosis without dismantling the whole system[236].

A number of methods currently exist for detecting currents wirelessly. Magnetic field sensors can detect current flowing by measuring the static magnetic fields they generate[243,244]. Although these methods can detect very low current levels, they

generally cannot achieve high spatial resolution without placing the sensor very close to the current because magnetometers will detect the sum of the fields from all current sources within their detection range[243]. One way to circumvent this problem is place a small sensor near the source of the current that reports wirelessly to an external receiver. Although this method requires a direct connection between the sensor and the current source, it can provide very high spatial resolutions while still providing wireless access to the sensor by an external receiver. For example, magnetometers based on diamond nanocrystals can detect local magnetic fields and report them to an external detector via their fluorescence at optical frequencies [245,246]. But optical fields cannot penetrate opaque specimen such as biological tissue and electronic packaging. Methods based on voltage sensitive dyes can also report local current activity with high spatial resolution[247]. But these methods also require optical access.

5.2 Spin transfer torque nano-oscillators for wireless local current sensing

Spin transfer torque nano-oscillators can provide an alternate approach for detecting local currents. These devices take as their input small direct currents and convert them to microwave current oscillations [248–252] that can report wirelessly to a receiver by magnetic induction. The spin transfer torque nano-oscillator occupies a small device footprint, potentially in the nanoscale, and can operate with input currents as low as 50 μA [253] opening the possibility for detecting weak signals with high spatial precision. Furthermore, the oscillation frequency of the device shifts in the presence of an external magnetic field and current magnitude[250,254], enabling the precession frequency to encode spatial information in an analogous way to conventional

magnetic resonance imaging. These properties make spin transfer torque nano-oscillators promising candidates for detecting small currents with high spatial precision. For example, in biological sensing they could potentially report on electrical activity in vivo in areas with no optical access due to the presence of bone or thick tissue.

Previous theoretical works investigated wireless broadcast with spin-transfer torque nano-oscillators for power transfer applications. Amin et al. [255] theoretically studied the radiation pattern of these devices and showed that the magnetic field oscillations in a spin-transfer torque nano-oscillator are detectable in the near field. Propenko et al [256] evaluated the radiation of arrays of oscillators as efficient sources of microwave signals for telecommunication devices. Experimentally, previous studies demonstrated wireless transmission using a spin transfer torque nano-oscillator over distances from 10 mm to 1 m [257,258], with potential applications in wireless communication. However, these works used active amplifiers and large dipole antennas to broadcast the signal. Such amplifiers and large antennas are appropriate for communication, but are difficult to integrate into small wireless sensors and require wireless power supplies which are challenging to fabricate. Many sensing applications often require compact passive sensors without any power sources beyond the local currents. To date, such wireless sensing of currents using a spin-transfer torque nano-oscillator has not been experimentally demonstrated.

Here we report direct wireless sensing of local currents by magnetic induction using a spin-transfer torque nano-oscillator. We use a micro-fabricated receiving coil to detect the microwave oscillations produced by the device, and detect currents in the range of 300-700 μA at distances of up to 6.5 mm. These results show that spintronic devices could potentially serve as nanoscale sensors for applications in biotechnology, electronics and embedded systems.

5.3 Materials and methods

The devices studied in this work were fabricated by Professor. Ilya Krivorotov's group at the University of California, Irvine under a grant from Weinberg Medical Physics Inc., Bethesda, Maryland. These devices are elliptical magnetic tunnel junction nanopillars with lateral dimensions 70 nm × 170 nm. Figure 19A shows the complete layer structure for the device, with thicknesses indicated in parentheses in units of nanometers. We deposited all layers using magnetron sputtering in a Singulus TIMARIS system, and patterned the magnetic tunnel junctions using electron beam lithography followed by ion milling. The synthetic antiferromagnet is PtMn(15)/ Co_{70} Fe_{30}(2.3)/ Ru(0.85)/ Co_{40} Fe_{40} B_{20}(2.4) with the $Co_{70}Fe_{30}$ pinned layer and the $Co_{40}Fe_{40}B_{20}$ reference layer antiferromagnetically coupled by the tuned thickness of Ru. Prior to patterning, we anneal the multilayer for 2 hours at 300 °C in a 1 T in-plane field to set the pinned layer exchange bias direction parallel to the long axis of the nanopillars.

To perform wireless current sensing, we utilize the experimental configuration illustrated in Figure 19B. We inject the small direct signal current into the device using a non-magnetic picoprobe (10-50/30-125-BeCu-2-R-200, GGB industries). This direct current flows from the free layer to the fixed layer of the device (Figure 19C). We apply a magnetic field of 0.15 T using a permanent magnet (K&J Magnetics) at an out-of-plane angle of 60^{o} with respect to the sample plane and an in-plane component of 30^{o} with respect to the major axis of the ellipse, which induces a free-layer precession [253] at a frequency of $f = 2.7$ GHz. The fixed layer and free layer are oriented mostly anti-parallel in the applied field conditions[259] and the observed oscillation mode is likely the lowest-frequency free layer mode in the anti-parallel state[26].The free layer precession generates a microwave frequency electromagnetic signal across the oscillator terminals via a tunneling magnetoresistance effect [260,261]. The microwave signal inductively couples to a receiving micro-coil resulting in a microwave voltage detected across the terminals of the coil. We also use a bias tee (Pasternack, PE1604) to extract the microwave at the output of the device using the capacitive port, which we can compare to the wireless induction signal. The magnitude of this microwave signal depends on the amount of direct current injected to the spin transfer torque nano-oscillator, while the resonant frequency depends on the magnitude and direction of the external magnetic field applied to the device as well as on the direct current injected to the device.

The receiving micro-coil, shown in Figure 19D, is composed of a metallic loop antenna with outer diameter of 46 μm and width of 6 μm. We fabricated the

receiving coil on a SiO_2 substrate using optical lithography followed by thermal vapor deposition of copper (thickness of 0.5 μm) and liftoff. We position the receiving coil directly above the device surface with the patterned coil facing the device. This is to ensure that the substrate thicknesses do not limit the distance between the device and the receiving coil. We collect the current from the coil using a microwave transmission strip line as a matching network to match the coil impedance to 50 Ohms and a coaxial SMA connector directly soldered to the leads of the strip line. A low noise amplifier (Pasternack PE15A1010, noise figure = 0.9 dB, gain = 40 dB and input impedance $z_0 = 50\ \Omega$) amplifies the output from the coil. We analyze the amplified output using a spectrum analyzer (Agilent 8564 EC, 9 kHz-40 GHz). We used the same spectrum analyzer to measure the output of the device through the capacitive port of the bias tee, so that we can compare the signals under identical gain

conditions.

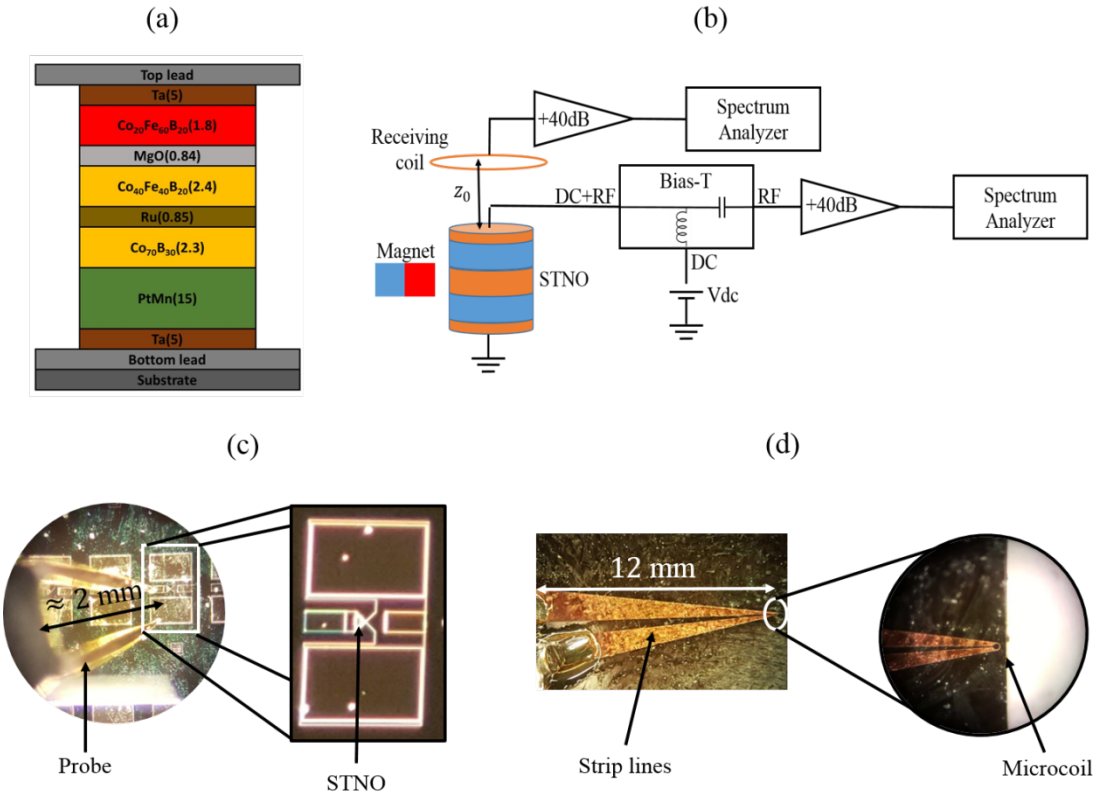

Figure 19: A) Schematic of the nanopillar spin torque oscillator device. The numbers in parentheses are the layer thicknesses in units of nanometers. B) A schematic of the microwave circuit used for direct electrical measurement from the device and wireless measurement of the microwave signal emission from spin transfer torque nano-oscillator. C) The microprobe and the connection pads along with the spin torque nano-oscillator forming an effective inductive coupler. D) The micro-fabricated receiving coil patterned on SiO_2 substrate.

5.4 Wireless measurement of Spin transfer torque nano-oscillators

Fig. 20A shows the power spectral density of the device output collected from the bias tee for several different values of the direct input current. The device begins to oscillate at an input current of approximately 100 μA with an oscillation frequency of 2.75 GHz. The oscillation frequency decreases as we increase the input current, which is expected because the nonlinear frequency shift for this device geometry is negative[250,254]. At 600 μA the device approaches the maximum output power spectral

density of 400 nW/GHz. At even larger input current of 700 μA we observe a second oscillation mode at slightly lower frequency which results in a broadened spectrum with two peaks. We attribute the lower frequency mode to the onset of the spin-torque-driven auto-oscillation mode [254,259]while the higher frequency mode is likely due to thermally activated oscillations [262]. Either of the signals can be used to perform sensing and the choice mainly depends on the amplitude of the input current.

Figure 20B shows the power spectrum of the induction signal obtained from the receiving coil for the same input currents used in Figure 20A. In these measurements, we position the receiving coil at a distance of 15 μm above the device. The spectra through the coil match the electrical measurements directly from the device shown in Figure 20A. We attribute the difference in the spectral shapes of the induced signal and the direct electrical signal to a mismatch between the frequency response of the device and the receiving coil. We attain a peak signal power density of 1.7 nW/GHz, which is a factor of 300 smaller than the measurement from the capacitive port of the bias tee. We note that the capacitive port of the bias tee shows microwave signal at input currents as low as 100 μA, but the wireless induction signal requires 300 μA to be detectable with our measurement setup. This disparity is caused by the reduced signal in the induction coil, which requires more driving current to generate a signal that exceeds the noise floor of the electrical circuit. We also note that the lower frequency mode (which appears at an input current 700 μA) induces signal more efficiently in the receiving coil, due to better spectral matching with the coil. We further confirmed this by measuring the transmission characteristics between the coil

and the device using a vector network analyzer as explained in later sections. As shown in Figure 20B inset, the transmission coefficient is higher for the lower frequency mode of 2.66 GHz compared to the higher frequency mode of 2.73 GHz.

Figure 20C plots the total microwave power for both the electrical output of the bias tee and the wireless signal induced in the receiving coil. Both signals exhibit the expected behavior where the microwave power increases with increased current [263]. Furthermore, the input current dependence of the wireless signal shows an identical behavior to the electrical measurement from the bias tee, which confirms that the wireless signal originates from the current induced in the device. At maximum input current of 700 μA, the electrical power measured directly from the bias tee is 69 nW as shown in Figure 20C. However, due to the impedance mismatch between the device and the amplifier, the measured electrical power from the bias tee is not the total power produced in the device. The total power produced in the device, P_d, is given by [264] :

$$P_d = \frac{Z_0 + Z_d}{Z_0} P_e \tag{1}$$

where P_e is the electrical power measured in the spectrum analyzer, $Z_d = 1$ kΩ is the impedance of the device and $Z_0 = 50$ Ω is the input impedance of the amplifier connected to the device. From Eq. (1) the total power produced in the device is 1470 nW. The wireless signal power measured in the receiving coil at maximum input current of 700 μA, is 0.15 nW, as shown in Figure 20C. The transmission efficiency

defined as the ratio between the wireless power received in the coil and the power generated by the device is 0.01%. Figure 21 plots the total power in the receiving coil as a function of distance between the receiving coil and the surface of the device, where we fix the input current at 700 μA. We observe a clear induction signal at distances of up to 6.5 mm.

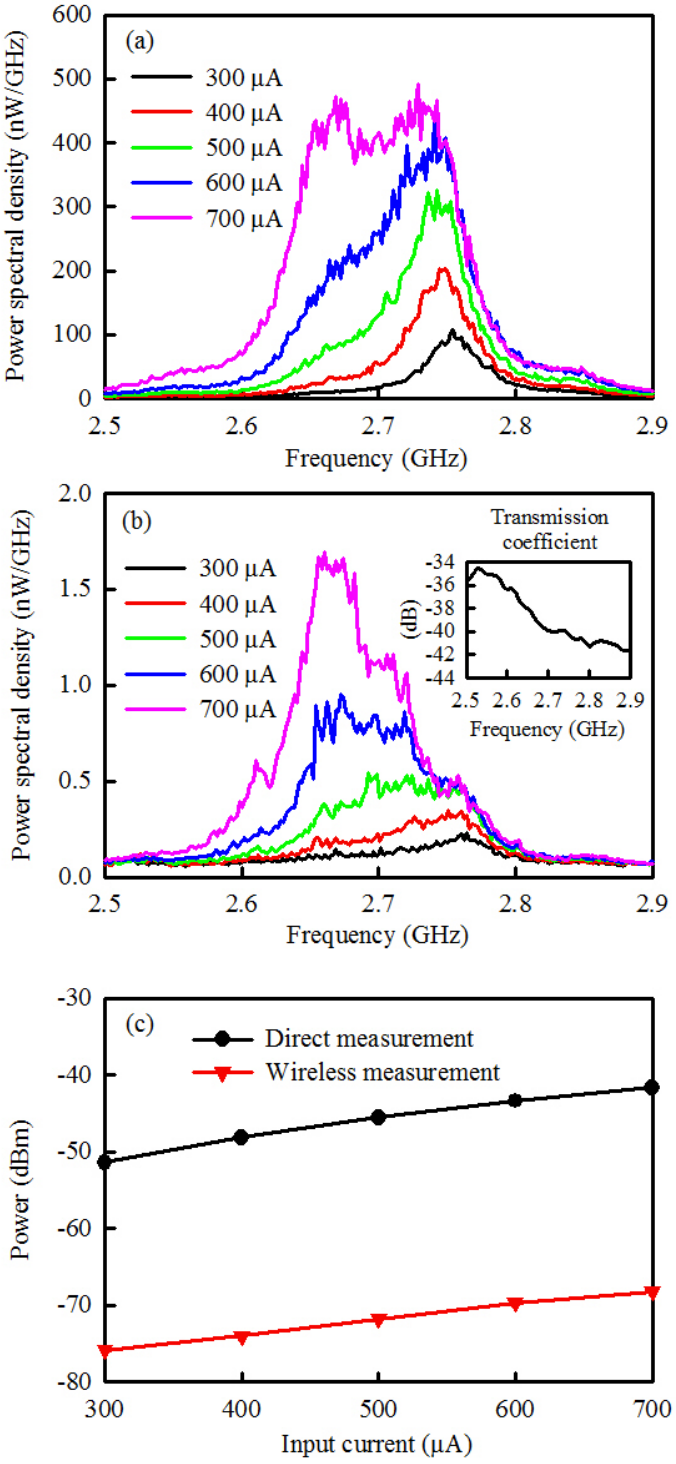

Figure 20: A) The power spectral density of the direct electrical signal measured from the spin transfer torque nano-oscillator at 0.15 T. B) The power spectral density of the wireless signal measured from the receiving coil at 0.15 T. The transmission coefficient measured between the device and coil using a network analyzer for the same frequency range (inset) C) The integrated power obtained in measurements versus bias current A) and B).

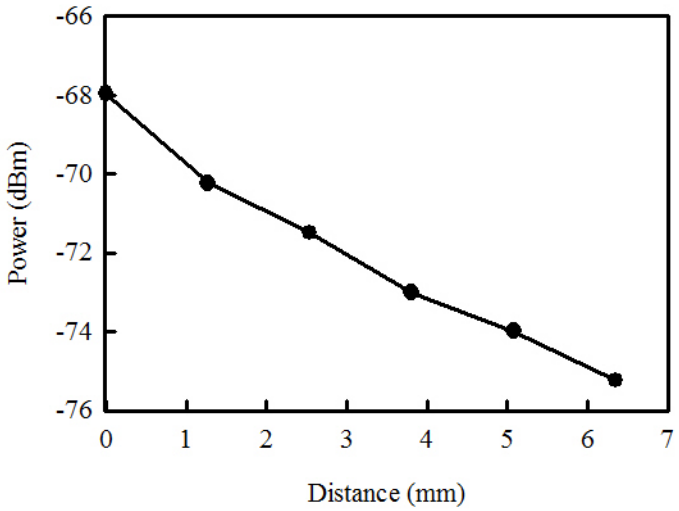

Figure 21: The wireless signal received from the spin transfer torque nano oscillator as a function of distance between the STNO and the receiving coil for a detection current I_{DC} = 700μA

The spin transfer torque nano-oscillator can induce current in the receiving micro-coil through two different mechanisms. The first is by direct induction from precessing magnetization of the free layer, and the second is induction by the microwave current oscillation in the electrical wires that connect to the device. We can estimate the contribution from the first mechanisms by treating the free layer as a magnetic point dipole and the receiving micro-coil as a single circular loop antenna. Since the receiving micro-coil impedance is matched to the amplifier impedance (50 Ω), the calculated power transmitted to the spectrum analyzer depends only upon the coil resistance and can be expressed as [264]:

$$P = \frac{1}{8}\frac{\varepsilon^2}{R_c} \tag{2}$$

where R_c is the micro-coil resistance and ε is the electromotive force amplitude induced in the receiving coil. We can estimate the resistance of the circular receiving micro-coil using the expression

$$R_c = \frac{1}{\sigma}\frac{2\pi r}{wt} \tag{3}$$

where σ is the copper conductivity, r is the mean radius of the micro-coil, w is the strip width and t is the copper thickness (t smaller than the skin depth). The electromotive force induced by a magnetic dipole is $\varepsilon = 2\pi f m_f B_c$ [265], where f is the frequency of the magnetic dipole, m_f is the amplitude of oscillations of the free layer magnetic moment and B_c is the magnetic field per unit current created by the receiving micro-coil at the position of the magnetic dipole. We approximate the circular loop as a thin wire loop and assume that the device lies along the axis. Under this approximation the magnetic field created by the circular receiving micro-coil per unit current is

$$B_c = \frac{\mu_0}{2}\frac{r^2}{(r^2 + z_0{}^2)^{\frac{3}{2}}} \tag{4}$$

where μ_0 is the magnetic permeability of vacuum, r is the coil radius and z_0 is the distance between the receiving micro-coil and the device. To perform calculations, we use experimental values of $r = 45$ μm, $w = 6$ μm, $t = 0.5$ μm and a distance of 15 μm between the spin transfer torque nano-oscillator and the receiving micro-coil. We use a free layer magnetic moment of $m_f = 10^{-17}$ J/T [266], and a resonant frequency $f = 2.7$ GHz consistent with our measurements, and we use Eq. (4) to

determine B_c. Using these values we estimate the induced power from Eq. (2) to be $P = 2.76 \cdot 10^{-6}$ pW. This value is 8 orders smaller than the actual signal we detect.

The induced power due to the second mechanism depends upon the geometry of the connecting pads, wires surrounding the spin-transfer torque nano-oscillator, and the microwave probe that contacts the chip. These wires form an effective inductive coupler that can induce current in the receiver. We performed numerical simulations using CST Microwave Studio (Computer Simulation Technology Inc.) to determine the induced power in the receiving micro-coil by this effective inductive coupler. These simulations incorporate the receiving micro coil with its corresponding strips lines (see Figure 19D) connected to a port of impedance 50 Ω. We model the spin transfer torque nano-oscillator as a port of impedance 1 kΩ. We include the pads connected to the device along with the input probe (see Figure 19C), and add a series resistance of 50 Ω to the probe to account for the characteristic impedance of the amplifier connected to the probe. From the numerical simulations we calculate an induced power of $P = 0.05$ nW in the receiving coil, which is close to our measured value of P = 0.15 nW, suggesting that the wireless power received is due to the microwave current oscillation in the electrical wires that connect to the device. The remaining discrepancy between the measured and numerically calculated values is likely due to the simplification of the complex probe geometry in our model.

To further validate that the wireless induction signal originates from the microwave current oscillations in the device, we use a two port network analyzer (HP Hewlett

Packard 8722D, 50 MHz – 40 GHz) to estimate the transmission efficiency between the device and the receiver and we compare it with the value previously calculated from the measurements in the spectrum analyzer. We connect the port one of the network analyzer to the device and the port two to the receiving coil with the coil placed directly above the device as explained before. For simplicity we assume that the receiver is perfectly matched to 50 Ω (due to the matching network) and that the main power is dissipated in the device (which is a good assumption due to its high impedance). With these assumptions, the transmission efficiency, η, can be estimated from the scattering parameters as [264]:

$$\eta = \frac{Z_d}{Z_d + Z_0} \frac{|S_{21}|^2}{1 - |S_{11}|^2} \tag{5}$$

where $Z_d = 1$ kΩ is the impedance of the device, $Z_0 = 50$ Ω is the input impedance of the amplifier connected to the device, S_{11} is the reflection coefficient in the device and S_{21} is the transmission coefficient between the device and the receiving coil. We measured the scattering parameters at 2.7 GHz, to be $S_{11} = -1.22$ dB and $S_{21} = -39.95$ dB. Introducing these values into Eq. (5) we estimate a transmission efficiency of 0.04%. This value approximates the transmission efficiency of 0.01% observed in our previous experiment of wireless detection from the device.

In summary, we have demonstrated that spin transfer torque nano-oscillators can act as wireless sensors for small local currents. We detected current and reported it wirelessly at distances exceeding 6 mm from the spin transfer torque nano-oscillators. We could improve the current sensitivity by using spin transfer torque nano-

oscillators with lower threshold currents [253]. Non-adiabatic stochastic resonance of magnetization[267,268] could also improve the sensitivity of the measurement by enhancing the amplitude of magnetization precession for a small current input. In addition, the current device uses the contact wires on the chip as an effective inductive coupler, which has a small mutual inductance with the receiving coil. We could increase the detection distance by patterning optimized inductors on the device itself that have higher mutual inductance with the receiver. Devices with large-amplitude magnetization precession [269,270] or reduced phase noise[271], arrays of phase locked oscillators [272–274], or oscillators with large volume of the free magnetic layer[275] could further extend the sensing range by emitting more power in a narrower bandwidth. Ultimately, our results present an approach for wireless current sensing that may play an important role in embedded systems, non-destructive testing of electronics, and in-vivo biological sensing and imaging.

5.5 Powering the nano-oscillators using crayfish neurons

Spin transfer torque nano-oscillators have been conventionally used to convert direct current to microwave whose frequency can be modulated using an external magnetic field. We investigated the possibility of using action potentials from crayfish lateral giant neurons as a direct current source for the spin transfer torque nano-oscillators. Such an ability to fire the nano-oscillators using bioelectric signals has a potential in in-vivo biosensing applications in the brain, heart and other electrophysiological systems.

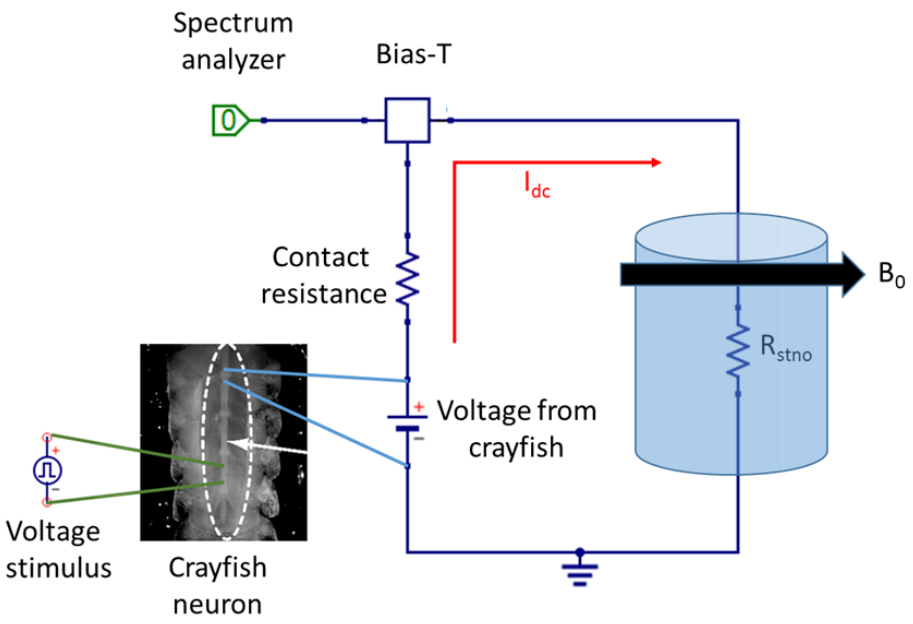

Figure 22: The schematic diagram for powering the spin transfer torque nano-oscillators using the neuronal action potentials from a crayfish neuron.

The lateral giant neurons from crayfish were extracted as explained by Herberholz et al [276]. The lateral giant neurons were stimulated using voltage pulses of 10 V amplitude and 5 Hz frequency and the corresponding action potentials produced in the neurons were recorded. These action potentials were visualized and confirmed using a digital oscilloscope (Keysight). Both the stimulations and the recordings were performed using extracellular silver electrodes of 1 mm diameter placed on the surface of the neurons. The operational frequency of the spin transfer torque nano-oscillator for a given external magnetic field was characterized as explained in Sec. 5.4 . In our measurements, an external in-plane magnetic field of 0.1 T was applied to the nano-oscillator using an electromagnet (GMW associates). The neuronal action potentials from the recording electrodes were input to the spin transfer torque nano-oscillator using the DC port of the bias-tee as shown in the Figure 22. The microwave

output from the spin transfer torque nano-oscillator was sent to a spectrum analyzer through the RF port of the bias-tee to analyze the power spectral density of the nano-oscillator response for its specific frequency of operation. The sweep time of the spectrum analyzer was synchronized with the crayfish stimulus frequency using the external trigger option in the spectrum analyzer. This was done to ensure that the nano-oscillator's response matched in time with the onset of the action potentials. The spectrum analyzer was operated in the zero-span mode to receive the measurements for the spin transfer nano-oscillator working frequency as a function of time. The measurements were averaged over 50 readings to filter the signal from the noise in the data. The measurements were sent to a LabVIEW program using a GPIB port for data collection and analysis.

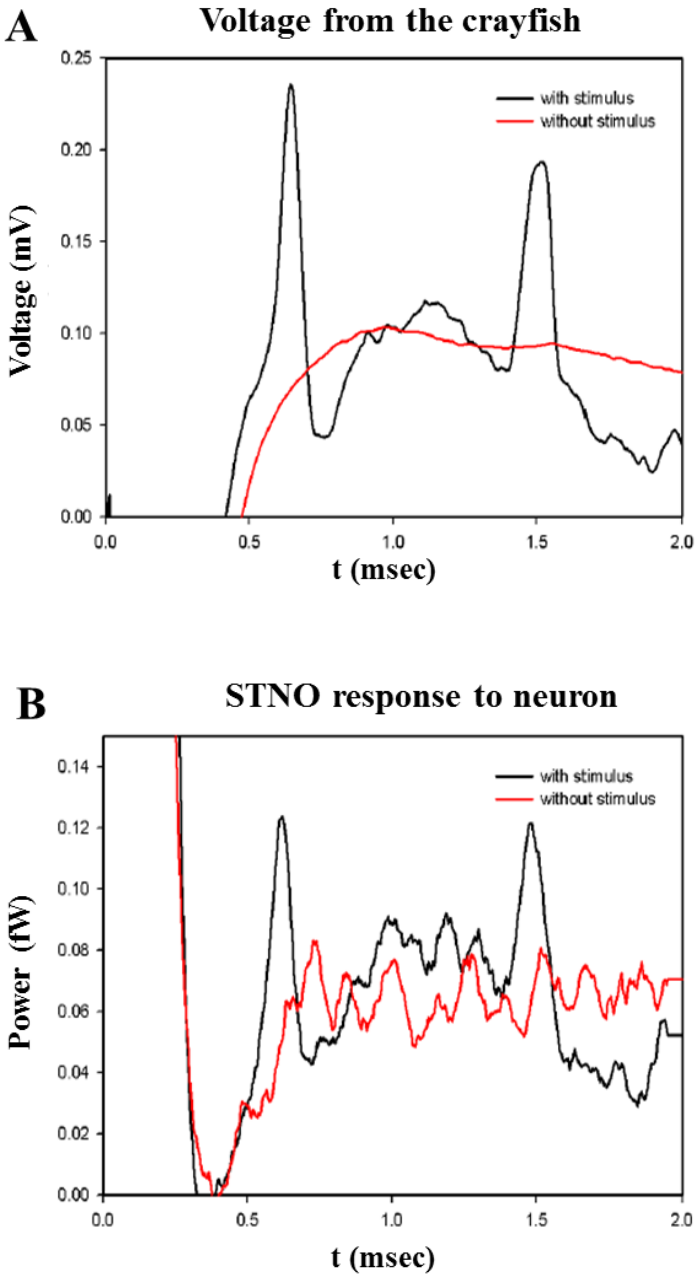

Figure 23: A) The recordings from the crayfish neurons with the application of a voltage stimulus (black) and without a stimulus (red). The neuronal action potential peaks can be observed in the recordings with stimulus. B) The response of the spin transfer torque nano-oscillators for the neuronal current input. The nano-oscillator responded to the action potential spikes with its corresponding power spikes at its working frequency.

The spin transfer torque nano-oscillator was characterized to oscillate at 0.85 GHz for an in-plane external magnetic field of 0.1 T. The crayfish later giant neuron, when stimulated electrically at 5 Hz, produced action potential spikes as shown in Figure 23A. These action potential spikes produced a current of ~ 0.8 μA when connected to the spin transfer torque nano-oscillator. The nano-oscillators responded with corresponding peak power spikes of 0.12 fW as shown in Figure 23B. These peaks were confirmed to be due to the neuronal currents by removing the stimulus electrode from the lateral giant neuron and observing no peaks in both the recording electrodes and the nano-oscillator.

5.6 Nano-oscillators as wireless microwave rectifiers

The rectifying effect of spin transfer torque nano-oscillators for an alternating current input has been demonstrated previously[277]. By using an appropriate external magnetic field, the nano-oscillators can be used to selectively rectify a specific frequency which is typically its operational frequency at that field. Such a mode of operation can be used for potential applications in wireless energy harvesting [278] and biomedical systems for wireless electrical stimulation of cells such as neurons[279–281]. In this section we have shown that the nano-oscillators can be used as wireless rectifiers where an alternating current is transmitted to it by near field induction to be rectified to a proportional DC voltage across the nano-oscillator.

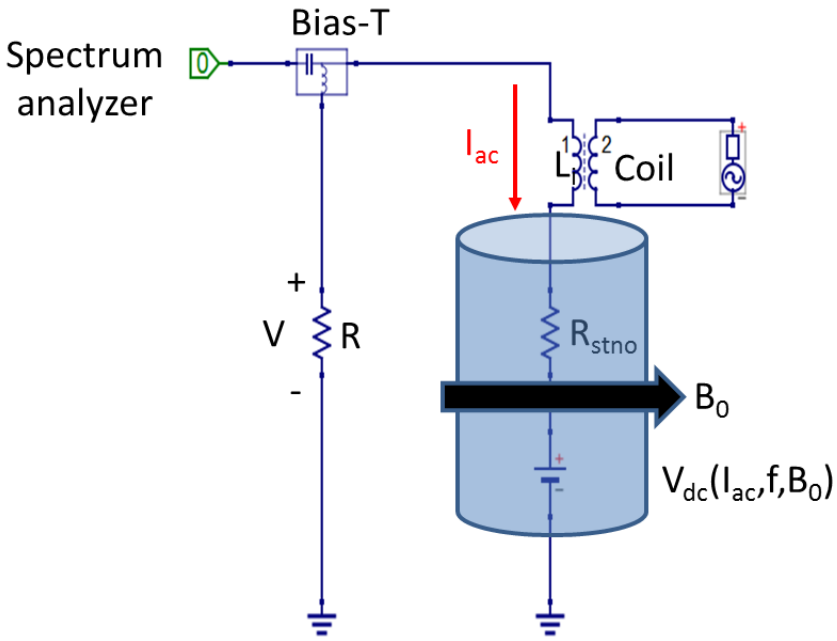

Figure 24: The schematic diagram of the circuit used for wireless alternate current stimulation of the spin transfer torque nano-oscillator and measuring the rectified DC voltage produced in it.

The spin transfer torque nano-oscillator was characterized for its working frequency for a particular external magnetic field as explained before. For these measurements, an magnetic field with an out of plane component of 0.06 T was applied with its axis perpendicular to the major and minor axes of the elliptical nano-oscillator device using a permanent magnet. The in-plane component of this field was 0.04T at an angle of 35° to the major axis of the nano-oscillator. The magnetic field was measured using a 3D gaussmeter (Lakeshore). A transmission coil was fabricated using copper with a single turn and connected to a microwave signal generator (Agilent) for transmitting alternate currents through near field induction. The coil was placed above the spin transfer-torque nano-oscillator at different distances from it controlled by a micropositioner. The direct and alternating current (radio frequency) output produced in the spin transfer torque nano-oscillator were studied using a high

precision digital multimeter (Agilent 34401A) and a spectrum analyzer (Agilent 8564EC 9kHz – 40 GHz) respectively after being routed through the corresponding ports in the bias tee as shown in Figure 24. The transmission frequency was swept between 0.1-6 GHz in the signal generator to study the dependence of DC voltage on the frequency of alternating current transmitted to the nano-oscillator from the coil.

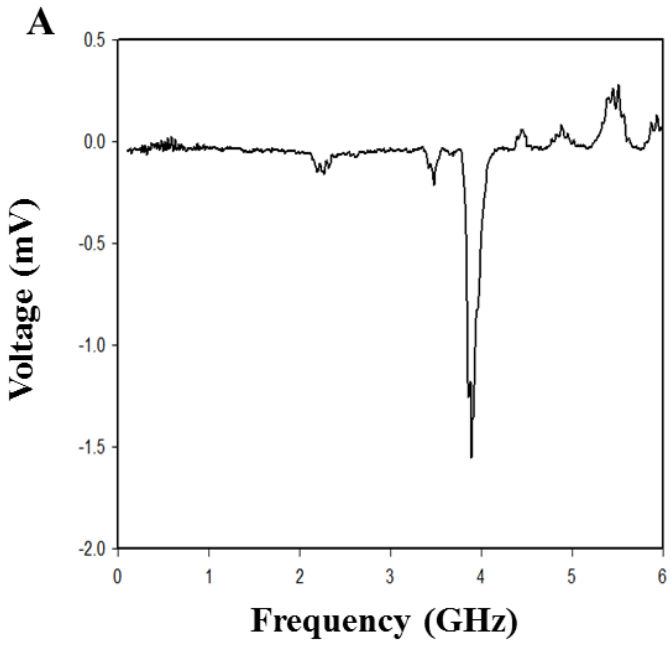

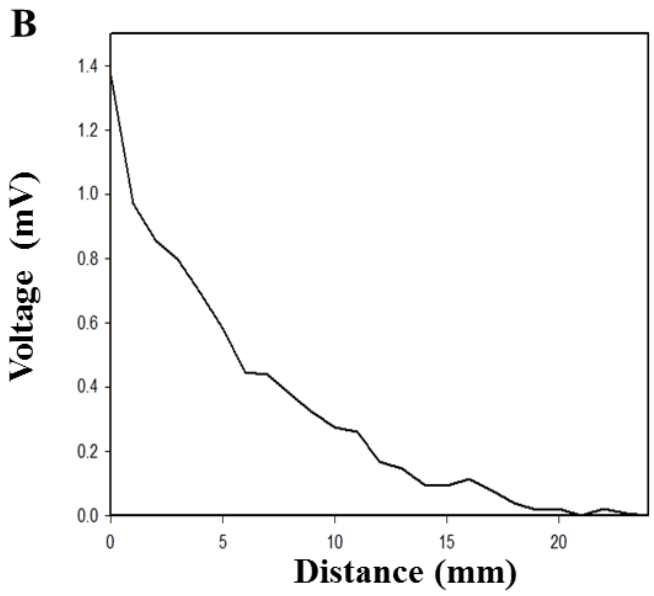

Figure 25: A) Dc voltage produced in the spin transfer torque nano-oscillator for different wirelessly transmitted input ac signals. The nano-oscillator produced DC voltage peaks for specific input frequencies (for e.g. 3.8 GHz) which can be modulated using the external magnetic field. B) The DC voltage produced for different distances between the transmission coil and the spin transfer torque nano-oscillator at an input AC frequency of 3.8 GHz.

The peak rectified DC voltage produced in the spin transfer torque nano-oscillator was around 1.4 mV for ac power transmitted at 3.81 GHz as shown in Figure 25A. Another peak with the opposite polarity was observed at 5.4 GHz. This change in polarity can be explained due to the direction of phase difference between the input AC power and the microwave magnetoresistance initiated in the nano-oscillator. The rectified DC voltage decreased with increasing distances between the transmission coil and the nano-oscillator as shown in Figure 25B and a DC voltage was produced in the device at distances of upto 1.5 cm.

Chapter 6: Conclusions

In this dissertation, I studied the motion of magnetic nanocarriers in different tissues, determined the factors influencing their motion and analyzed the safety of their motion in a live brain tissue. Prednisolone coated magnetic nanocarriers were shown to reduce cisplatin induced ototoxicity in mice. Finally, spin transfer torque nano-oscillators have been shown to respond to action potentials from a single neuron. The nano-oscillators have been wirelessly detected and activated with potential applications in wireless neuroimaging and neuromodulation.

An automated cryostat system was designed and built to quantitatively measure the penetration depth of magnetic nanoparticles (MNPs) into tissue samples under the action of an applied magnetic field. Fluorescent MNPs of four different sizes (100 nm, 300 nm, 500 nm, and 1 μm diameter) and with four different coatings (starch, chitosan, lipid, PEG/P) were tested in liver, kidney and brain tissue samples using this system. The nanoparticle size, magnetic properties and surface coating influenced their motion in tissue samples. The automated cryostat system can be used in future applications to engineer, test and optimize nanoparticles for increasing their transport in tissue.

The interactive motion of MNPs was studied in detail in brain tissue under the influence of a uniform magnetic field. MNPs agglomerated into MNP chains in tissue and this behavior was influenced by a combination of applied uniform magnetic field and the concentration of magnetic nanoparticles present in tissue. The mechanism of

MNP chaining was shown to be dominated by magnetic drift caused by overlapping regions of influence of each magnetized nanoparticle. At cellular level, the movement of MNPs did not cause a significant change in the firing rate of the neurons. Spontaneous inhibitory post-synaptic currents in the granule cells of the main olfactory bulb have been shown to increase in frequency by the addition of noradrenaline[190]. This behavior was not modified by the movement of MNPs in the region thereby maintaining the synaptic connectivity of the neurons. This was further confirmed using calcium imaging of granule cells after moving MNPs in the region followed by adding glutamate. The increase in intracellular calcium due to glutamate stimuli remained consistent in the region even after the nanoparticle motion. Finally, the nanoparticle motion did not physically affect the connections between the neurons in the olfactory bulb. Therefore, magnetic nanocarriers attached to therapeutic agents can be safely transported in the brain using external magnets. In future, chaining of MNPs in brain tissue can be mathematically modeled based on the magnetic drift dominated mechanism. This can be used to predict the distribution of MNP chain lengths observed in brain tissue for specific external magnetic field configuration. During chaining, the magnetic force experienced by the group of MNPs in a chain is increased and the drag force is reduced. This is due to increase in magnetic volume but decrease in the effective surface area in contact with the tissue. Therefore, a predictive model that helps in determining and controlling MNP chain lengths can be used to increase the transportation efficiency of magnetic nanocarriers in tissue.

Cisplatin, a common chemotherapeutic drug, has been shown to cause severe ototoxicity by affecting outer and inner cochlear hair cells, stria vascularis and spiral ganglion[216]. The ototoxic effect of cisplatin has been reduced by intra-tympanic administration of steroids such as dexamethasone or prednisolone in various animal studies[80,214,228]. Such a method faces the dual challenge of low concentration of drugs in the cochlea due to ineffective passive diffusion from the middle ear through the window membranes and drainage of drugs in the middle ear through the eustachian tube. Magnetic delivery of prednisolone to the cochlea of cisplatin treated mice has been demonstrated. This method has been shown to reduce hearing loss significantly at high frequencies compared to intra-tympanic prednisolone application or saline control. Magnetic prednisolone delivery also significantly reduced the damage caused to the hair cells in the cochlea. This method can be improved in future through better designs of magnetic targeting systems to target magnetic nanocarriers uniformly across all turns of the cochlea. This will reduce cisplatin induced hearing loss throughout the audible frequency range and not just the high frequencies. The entry of nanoparticles and mechanism of steroid action in preventing the ototoxic effects of cisplatin in cochlea, need to be studied. Apart from providing pharmacological insights, this study will also help design better nanocarriers with a controlled drug release synchronized to the onset of cisplatin induced ototoxicity.

High resolution functional imaging has remained one of the major challenges in image guided delivery of therapeutics in the brain. Most conventional imaging modalities provide only structural information of different regions in the brain with

resolution in the order of millimeters. Even functional MRI (fMRI) only provides coarse information on which region in the brain received more oxygen. Therefore, there is an unmet medical need to sense currents from individual neurons in a region and supplement the conventional structural images. This will help in understanding various physiological processes in the brain paving way for a better diagnosis of neurodegenerative diseases. Spin transfer torque nano-oscillators have been hypothesized to sense currents from a single neuron and report the information wirelessly. First, such a wireless broadcast and reception of detected dc currents has been shown possible with a nano-oscillator using near field induction. These nano-oscillators have been shown to respond to a single neuron action potential. The response magnitude depends upon the amount of current input to the device and the response frequency can be modulated using an external magnetic field. With the knowledge of the frequency dependence of the nano-oscillator signal with magnetic field and by applying a known magnetic field distribution in the brain, signals from the nano-oscillators can be precisely located in the brain, Therefore, neurons attached to such nano-oscillators can in turn be spatially located in the brain. The response of the nano-oscillator for a crayfish neuron signal was shown to be in the order of 10^{-15} W. Due to a low signal to noise ratio of this measurement, it is difficult to detect this power wirelessly using the current configuration. In future, nano-oscillators need to be optimized to produce higher response for currents less than 1 μA. In order for this method to be applicable for mammalian neurons, the devices have to respond effectively to currents in the order of nanoamperes. This can be achieved through better device designs[271,275], phase locking the response of multiple

devices[272,282],improving the coupling efficiency of the wireless receiver coils and using signal conditioning systems such as lock-in amplifiers at the receiver end.

The nano-oscillators have been shown to function as wireless rectifiers. They produce a DC voltage across them for a wireless AC current transmitted to them by magnetic induction. This rectifying property has been shown to be frequency selective and the external magnetic field determines this selectivity. The DC voltage produced can be used stimulate a neuron attached to the nano-oscillator. Similar to determining the precise location of firing neurons using the nano-oscillators, a combination of magnetic field and frequency of transmitted signal, neurons at specific locations can be activated without affecting other neurons in the region. In summary, spin transfer torque nano-oscillators can potentially sense or activate a single specific neuron wirelessly. This technique can supplement current imaging modalities such as MRI to provide more insights into inner workings of the brain during different physiological processes and improve our understanding of various neurological disorders.

Intellectual contributions

Most of the work in this dissertation is a result of inter-disciplinary collaboration. In this section, I attribute key aspects of the work to the people most responsible for them. The table gives a summary of my contributions relative to other collaborators. The first column lists the different projects explained in detail in each chapter of this dissertation. The second column and third column explain my contribution and the collaborators' contributions to each of the projects respectively.

Project	**My contribution**	**Collaborators' contribution**
Movement of magnetic nanoparticles in brain tissue : mechanisms and safety (Chapter 3)	I developed the concept, built the hardware and software platform for automated 3D magnetic field measurement. I characterized the properties of nanoparticles used in the experiments I designed and performed experiments for studying the mechanism of nanoparticle motion in brain tissue. I assisted Villar and Eberly with electrophysiology and immunohistochemistry experiments for safety study I analyzed electrophysiology recordings to assess the safety of nanoparticle motion in brain	Villar: Performed the patch clamp experiments to study action potentials and inhibitory post-synaptic currents in live brain tissue. Smith : Performed the calcium imaging experiments to study changes in neural circuitry in the main olfactory bulb after nanoparticle motion Eberly: Performed the immunohistochemistry experiments and confocal imaging to study the impact of nanoparticle motion on neuronal connections.
Magnetic steroid targeting to the inner ear to reduce cisplatin induced ototoxicity (Chapter 4)	I implemented the animal experiments to study cisplatin induced ototoxicity and performed magnetic targeting experiments in the mice model.	

	I performed ABR recordings and cytocochleograms to visualize the cochlear hair cells of animals from the different groups I analyzed ABR data for different animal groups and imaged cochlear hair cells from the different groups using confocal microscopy	
Spintronic devices for single neuron sensing and activation (Chapter 5)	I analytically modeled, simulated and fabricated the wireless receiver coil to obtain signals from the spin transfer torque nano-oscillator tuned to its working frequency With Algarin: I designed, implemented the circuit and developed the data acquisition software platform to characterize the nano-oscillators and perform wireless measurements. With Swierzbinski, Venuti and Algarin : I performed integration experiments for powering the nano-oscillators using crayfish neuronal currents With Algarin: I performed wireless AC stimulation experiments	Swierzbinski and Venuti: Performed crayfish neuron dissections and implemented the extracellular recording setup. Algarin : Fabricated the solenoid coils for AC stimulation experiments
Analyzing the movement of different magnetic nanoparticles in various tissues (Chapter 2)	With Kulkarni and Nacev: I developed the hardware and software platform for building the automated cryostat system to slice tissue samples and perform fluorescence imaging. I characterized the size, surface charge and magnetic properties of different magnetic nanoparticles and performed the cryostat experiments. Assisted Kulkarni with data processing and analysis for conclusions.	Nacev and Kulkarni : Initial hardware integration of cryostat hardware and software Kulkarni: Developed concept, designed and performed experiments. Developed the image processing software.

Bibliography

1. Freeman, A. I. & Mayhew, E. Targeted drug delivery. *Cancer* **58,** 573–583 (1986).
2. Fielding, R. M. Liposomal Drug Delivery. *Clin. Pharmacokinet.* **21,** 155–164 (2012).
3. Allen, T. M. & Cullis, P. R. Liposomal drug delivery systems: From concept to clinical applications. *Adv. Drug Deliv. Rev.* **65,** 36–48 (2013).
4. Singh, R. & Lillard Jr., J. W. Nanoparticle-based targeted drug delivery. *Exp. Mol. Pathol.* **86,** 215–223 (2009).
5. Mora-Huertas, C. E., Fessi, H. & Elaissari, A. Polymer-based nanocapsules for drug delivery. *Int. J. Pharm.* **385,** 113–142 (2010).
6. Lang, C., Schüler, D. & Faivre, D. Synthesis of Magnetite Nanoparticles for Bio- and Nanotechnology: Genetic Engineering and Biomimetics of Bacterial Magnetosomes. *Macromol. Biosci.* **7,** 144–151 (2007).
7. Freiberg, S. & Zhu, X. X. Polymer microspheres for controlled drug release. *Int. J. Pharm.* **282,** 1–18 (2004).
8. Pillai, O. & Panchagnula, R. Polymers in drug delivery. *Curr. Opin. Chem. Biol.* **5,** 447–451 (2001).
9. Tan, M. L., Choong, P. F. M. & Dass, C. R. Recent developments in liposomes, microparticles and nanoparticles for protein and peptide drug delivery. *Peptides* **31,** 184–193 (2010).
10. Rösler, A., Vandermeulen, G. W. M. & Klok, H.-A. Advanced drug delivery devices via self-assembly of amphiphilic block copolymers. *Adv. Drug Deliv. Rev.* **64, Supplement,** 270–279 (2012).
11. London, N. J. S., Chiang, A. & Haller, J. A. The dexamethasone drug delivery system: Indications and evidence. *Adv. Ther.* **28,** 351–366 (2011).

12. Tan, D. T. H., Chee, S.-P., Lim, L., Theng, J. & Van Ede, M. Randomized clinical trial of surodex steroid drug delivery system for cataract surgery: Anterior versus posterior placement of two surodex in the eye1. *Ophthalmology* **108,** 2172–2181 (2001).

13. Eroğlu, H., Sargon, M. F. & Öner, L. Chitosan Formulations for Steroid Delivery: Effect of Formulation Variables on In Vitro Characteristics. *Drug Dev. Ind. Pharm.* **33,** 265–271 (2007).

14. Pan, Y. *et al.* Bioadhesive polysaccharide in protein delivery system: chitosan nanoparticles improve the intestinal absorption of insulin in vivo. *Int. J. Pharm.* **249,** 139–147 (2002).

15. Mitragotri, S., Blankschtein, D. & Langer, R. Ultrasound-mediated transdermal protein delivery. *Science* **269,** 850 (1995).

16. Sinha, V. R. & Trehan, A. Biodegradable microspheres for protein delivery. *J. Controlled Release* **90,** 261–280 (2003).

17. Gan, Q. & Wang, T. Chitosan nanoparticle as protein delivery carrier—Systematic examination of fabrication conditions for efficient loading and release. *Colloids Surf. B Biointerfaces* **59,** 24–34 (2007).

18. Cho, K., Wang, X., Nie, S., Chen, Z. (Georgia) & Shin, D. M. Therapeutic Nanoparticles for Drug Delivery in Cancer. *Clin. Cancer Res.* **14,** 1310–1316 (2008).

19. Haley, B. & Frenkel, E. Nanoparticles for drug delivery in cancer treatment. *Urol. Oncol. Semin. Orig. Investig.* **26,** 57–64 (2008).

20. Morton, S. W. *et al.* A Nanoparticle-Based Combination Chemotherapy Delivery System for Enhanced Tumor Killing by Dynamic Rewiring of Signaling Pathways. *Sci. Signal.* **7,** ra44 (2014).

21. Loebinger, M. R., Eddaoudi, A., Davies, D. & Janes, S. M. Mesenchymal Stem Cell Delivery of TRAIL Can Eliminate Metastatic Cancer. *Cancer Res.* **69,** 4134–4142 (2009).

22. Ballios, B. G., Cooke, M. J., van der Kooy, D. & Shoichet, M. S. A hydrogel-based stem cell delivery system to treat retinal degenerative diseases. *Biomaterials* **31,** 2555–2564 (2010).

23. Perin, E. C. & López, J. Methods of stem cell delivery in cardiac diseases. *Nat. Rev. Cardiol.* **3,** S110–S113 (2006).

24. Naldini, L., Blomer, U., Gallay, P., Ory, D. & al, et. In vivo gene delivery and stable transduction of nondividing cells by a lentiviral vector. *Science* **272,** 263 (1996).

25. Pack, D. W., Hoffman, A. S., Pun, S. & Stayton, P. S. Design and development of polymers for gene delivery. *Nat. Rev. Drug Discov.* **4,** 581–593 (2005).

26. Kim, J., Kim, J., Jeong, C. & Kim, W. J. Synergistic nanomedicine by combined gene and photothermal therapy. *Adv. Drug Deliv. Rev.* **98,** 99–112 (2016).

27. Sun, C., Lee, J. S. H. & Zhang, M. Magnetic nanoparticles in MR imaging and drug delivery. *Adv. Drug Deliv. Rev.* **60,** 1252–1265 (2008).

28. Alexiou, C. *et al.* Magnetic Drug Targeting - A new approach in locoregional tumortherapy with chemotherapeutic agents. Experimental animal studies. *Hno* **53,** 618–622 (2005).

29. Dobson, J. Magnetic micro- and nano-particle-based targeting for drug and gene delivery. *Nanomed.* **1,** 31–37 (2006).

30. Lee, J.-C. & Lee, S. Dielectrophoresis-magnetophoresis force driven magnetic nanoparticle movement in transformer oil based magnetic fluids. *J. Nanosci. Nanotechnol.* **13,** 6179–6182 (2013).

31. Forbes, Z. G. *et al.* Validation of high gradient magnetic field based drug delivery to magnetizable implants under flow. *IEEE Trans. Biomed. Eng.* **55,** 643–649 (2008).

32. Mitragotri, S. Healing sound: the use of ultrasound in drug delivery and other therapeutic applications. *Nat. Rev. Drug Discov.* **4,** 255–260 (2005).

33. Hernot, S. & Klibanov, A. L. Microbubbles in ultrasound-triggered drug and gene delivery. *Adv. Drug Deliv. Rev.* **60,** 1153–1166 (2008).

34. Tachibana, K. & Tachibana, S. The Use of Ultrasound for Drug Delivery. *Echocardiography* **18,** 323–328 (2001).

35. Woodworth, G. F., Dunn, G. P., Nance, E. A., Hanes, J. & Brem, H. Emerging insights into barriers to effective brain tumor therapeutics. *Neuro-Oncol.* **4,** 126 (2014).

36. Alam, M. I. *et al.* Strategy for effective brain drug delivery. *Eur. J. Pharm. Sci.* **40,** 385–403 (2010).

37. Banerjee, S. & Bhat, M. A. Neuron-Glial Interactions in Blood-Brain Barrier Formation. *Annu. Rev. Neurosci.* **30,** 235–258 (2007).

38. Risau, W. Differentiation of endothelium. *FASEB J. Off. Publ. Fed. Am. Soc. Exp. Biol.* **9,** 926–933 (1995).

39. Ghose, A. K., Viswanadhan, V. N. & Wendoloski, J. J. A knowledge-based approach in designing combinatorial or medicinal chemistry libraries for drug discovery. 1. A qualitative and quantitative characterization of known drug databases. *J. Comb. Chem.* **1,** 55–68 (1999).

40. Pardridge, W. M. Drug transport across the blood–brain barrier. *J. Cereb. Blood Flow Metab.* **32,** 1959–1972 (2012).

41. Groothuis, D. R. The blood-brain and blood-tumor barriers: A review of strategies for increasing drug delivery. *Neuro-Oncol.* **2,** 45–59 (2000).

42. Sjo¨gren, A. *et al.* Extravasation of staphylococcal α-toxin in normal and injured CNS regions lacking blood-brain barrier function: observations after ventral root replantation. *Brain Res.* **559,** 276–282 (1991).

43. Brightman, M. W., Klatzo, I., Olsson, Y. & Reese, T. S. The blood-brain barrier to proteins under normal and pathological conditions. *J. Neurol. Sci.* **10,** 215–239 (1970).

44. Pollay, M. & Roberts, P. A. Blood-Brain Barrier: A Definition of Normal and Altered Function. *Neurosurgery* **6,** 675–685 (1980).

45. Abbott, N. J. Evidence for bulk flow of brain interstitial fluid: significance for physiology and pathology. *Neurochem. Int.* **45,** 545–552 (2004).

46. Min, K. J., Yoon, S. H. & Kang, J.-K. New understanding of the role of cerebrospinal fluid: offsetting of arterial and brain pulsation and self-dissipation of cerebrospinal fluid pulsatile flow energy. *Med. Hypotheses* **76,** 884–886 (2011).

47. Vargová, L. *et al.* Diffusion parameters of the extracellular space in human gliomas. *Glia* **42,** 77–88 (2003).

48. Blasi, P., Giovagnoli, S., Schoubben, A., Ricci, M. & Rossi, C. Solid lipid nanoparticles for targeted brain drug delivery. *Adv. Drug Deliv. Rev.* **59,** 454–477 (2007).

49. Kong, S. D. *et al.* Magnetic targeting of nanoparticles across the intact blood-brain barrier. *J. Control. Release Off. J. Control. Release Soc.* **164,** 49–57 (2012).

50. Chertok, B. *et al.* Iron oxide nanoparticles as a drug delivery vehicle for MRI monitored magnetic targeting of brain tumors. *Biomaterials* **29,** 487–496 (2008).

51. Xia, H. *et al.* Low molecular weight protamine-functionalized nanoparticles for drug delivery to the brain after intranasal administration. *Biomaterials* **32,** 9888–9898 (2011).

52. Weinberg, I. N. *et al.* Non-invasive image-guided brain access with gradient propulsion of magnetic nanoparticles. in *2012 IEEE Nuclear Science Symposium and Medical Imaging Conference (NSS/MIC)* 3732–3734 (2012). doi:10.1109/NSSMIC.2012.6551857

53. Trapani, A. *et al.* Characterization and evaluation of chitosan nanoparticles for dopamine brain delivery. *Int. J. Pharm.* **419,** 296–307 (2011).

54. Aktaş, Y. *et al.* Development and Brain Delivery of Chitosan−PEG Nanoparticles Functionalized with the Monoclonal Antibody OX26. *Bioconjug. Chem.* **16,** 1503–1511 (2005).

55. Wankhede, M., Bouras, A., Kaluzova, M. & Hadjipanayis, C. G. Magnetic nanoparticles: an emerging technology for malignant brain tumor imaging and therapy. *Expert Rev. Clin. Pharmacol.* **5,** 173–186 (2012).

56. Mykhaylyk, O. *et al.* Glial brain tumor targeting of magnetite nanoparticles in rats. *J. Magn. Magn. Mater.* **225,** 241–247 (2001).

57. Burkhardt, J.-K. *et al.* Intra-arterial delivery of bevacizumab after blood-brain barrier disruption for the treatment of recurrent glioblastoma: progression-free survival and overall survival. *World Neurosurg.* **77,** 130–134 (2012).

58. Boockvar, J. A. *et al.* Safety and maximum tolerated dose of superselective intraarterial cerebral infusion of bevacizumab after osmotic blood-brain barrier disruption for recurrent malignant glioma. *J. Neurosurg.* **114,** 624–632 (2011).

59. Miyagami, M., Tsubokawa, T., Tazoe, M. & Kagawa, Y. Intra-arterial ACNU Chemotherapy Employing 20% Mannitol Osmotic Blood-brain Barrier Disruption for Malignant Brain Tumors. *Neurol. Med. Chir. (Tokyo)* **30,** 582–590 (1990).

60. Grossman, S. A. *et al.* The intracerebral distribution of BCNU delivered by surgically implanted biodegradable polymers. *J. Neurosurg.* **76,** 640–647 (1992).

61. Kerr, J. Z., Berg, S. & Blaney, S. M. Intrathecal chemotherapy. *Crit. Rev. Oncol. Hematol.* **37,** 227–236 (2001).

62. Yamada, K. *et al.* Basic fibroblast growth factor prevents thalamic degeneration after cortical infarction. *J. Cereb. Blood Flow Metab. Off. J. Int. Soc. Cereb. Blood Flow Metab.* **11,** 472–478 (1991).

63. Graff, C. L. & Pollack, G. M. Nasal drug administration: potential for targeted central nervous system delivery. *J. Pharm. Sci.* **94,** 1187–1195 (2005).

64. Costantino, H. R., Illum, L., Brandt, G., Johnson, P. H. & Quay, S. C. Intranasal delivery: Physicochemical and therapeutic aspects. *Int. J. Pharm.* **337,** 1–24 (2007).

65. Stachler, R. J. *et al.* Clinical practice guideline: sudden hearing loss. *Otolaryngol.--Head Neck Surg. Off. J. Am. Acad. Otolaryngol.-Head Neck Surg.* **146,** S1-35 (2012).

66. Prevalence of Chronic Tinnitus: Chart | NIDCD. Available at: https://www.nidcd.nih.gov/health/statistics/prevalence-chronic-tinnitus-chart. (Accessed: 26th October 2016)

67. Ménière's Disease | NIDCD. Available at: https://www.nidcd.nih.gov/health/menieres-disease. (Accessed: 26th October 2016)

68. Shapiro, B. *et al.* Shaping Magnetic Fields to Direct Therapy to Ears and Eyes. *Annu. Rev. Biomed. Eng.* **16,** 455–481 (2014).

69. Parnes, L. S., Sun, A. H. & Freeman, D. J. Corticosteroid pharmacokinetics in the inner ear fluids: an animal study followed by clinical application. *The Laryngoscope* **109,** 1–17 (1999).

70. Sorrells, S. F. & Sapolsky, R. M. An inflammatory review of glucocorticoid actions in the CNS. *Brain. Behav. Immun.* **21,** 259–272 (2007).

71. Sholter, D. E. & Armstrong, P. W. Adverse effects of corticosteroids on the cardiovascular system. *Can. J. Cardiol.* **16,** 505–511 (2000).

72. Kratchman, L. B. *et al.* A manually operated, advance off-stylet insertion tool for minimally invasive cochlear implantation surgery. *IEEE Trans. Biomed. Eng.* **59,** 2792–2800 (2012).

73. Hoffer, M. E. *et al.* Use of the round window microcatheter in the treatment of Meniere's disease. *The Laryngoscope* **111,** 2046–2049 (2001).

74. Merchant, S. N. & Nadol, J. B. *Schuknecht's Pathology of the Ear*. (PMPH-USA, 2010).

75. Radeloff, A. *et al.* Impact of intrascalar blood on hearing. *The Laryngoscope* **117,** 58–62 (2007).

76. Rivera, T., Sanz, L., Camarero, G. & Varela-Nieto, I. Drug delivery to the inner ear: strategies and their therapeutic implications for sensorineural hearing loss. *Curr. Drug Deliv.* **9,** 231–242 (2012).

77. Salt, A. N. & Plontke, S. K. Principles of Local Drug Delivery to the Inner Ear. *Audiol. Neurotol.* **14,** 350–360 (2009).

78. Swan, E. E. L., Mescher, M. J., Sewell, W. F., Tao, S. L. & Borenstein, J. T. Inner ear drug delivery for auditory applications. *Adv. Drug Deliv. Rev.* **60,** 1583–1599 (2008).

79. McCall, A. A. *et al.* Drug delivery for treatment of inner ear disease: current state of knowledge. *Ear Hear.* **31,** 156–165 (2010).

80. Salt, A. N., Hartsock, J., Plontke, S., LeBel, C. & Piu, F. Distribution of Dexamethasone and Preservation of Inner Ear Function following Intratympanic Delivery of a Gel-Based Formulation. *Audiol. Neurotol.* **16,** 323–335 (2011).

81. Kopke, R. D. *et al.* Magnetic nanoparticles: inner ear targeted molecule delivery and middle ear implant. *Audiol. Neurootol.* **11,** 123–133 (2006).

82. Silverstein, H. Use of a new device, the MicroWick, to deliver medication to the inner ear. *Ear. Nose. Throat J.* **78,** 595–598, 600 (1999).

83. Suryanarayanan, R., Srinivasan, V. R. & O'Sullivan, G. Transtympanic gentamicin treatment using Silverstein MicroWick in Ménière's disease patients: long term outcome. *J. Laryngol. Otol.* **123,** 45–49 (2009).

84. Plontke, S. K., Zimmermann, R., Zenner, H.-P. & Löwenheim, H. Technical note on microcatheter implantation for local inner ear drug delivery: surgical technique and safety aspects. *Otol. Neurotol. Off. Publ. Am. Otol. Soc. Am. Neurotol. Soc. Eur. Acad. Otol. Neurotol.* **27,** 912–917 (2006).

85. Lee, K. Y. *et al.* Novel therapy for hearing loss: delivery of insulin-like growth factor 1 to the cochlea using gelatin hydrogel. *Otol. Neurotol. Off. Publ. Am. Otol. Soc. Am. Neurotol. Soc. Eur. Acad. Otol. Neurotol.* **28,** 976–981 (2007).

86. Paulson, D. P. *et al.* A novel controlled local drug delivery system for inner ear disease. *The Laryngoscope* **118,** 706–711 (2008).

87. Nacev, A. *et al.* Towards Control of Magnetic Fluids in Patients: Directing Therapeutic Nanoparticles to Disease Locations. *IEEE Control Syst.* **32,** 32–74 (2012).

88. Arruebo, M. *et al.* Sustained release of doxorubicin from zeolite–magnetite nanocomposites prepared by mechanical activation. *Nanotechnology* **17,** 4057 (2006).

89. Du, X. *et al.* Magnetic targeted delivery of dexamethasone acetate across the round window membrane in guinea pigs. *Otol. Neurotol. Off. Publ. Am. Otol. Soc. Am. Neurotol. Soc. Eur. Acad. Otol. Neurotol.* **34,** 41–47 (2013).

90. Ito, A. *et al.* Tumor regression by combined immunotherapy and hyperthermia using magnetic nanoparticles in an experimental subcutaneous murine melanoma. *Cancer Sci.* **94,** 308–313 (2003).

91. Cromer Berman, S. M., Walczak, P. & Bulte, J. W. M. Tracking stem cells using magnetic nanoparticles. *Wiley Interdiscip. Rev. Nanomed. Nanobiotechnol.* **3,** 343–355 (2011).

92. Nitin, N., LaConte, L. E. W., Zurkiya, O., Hu, X. & Bao, G. Functionalization and peptide-based delivery of magnetic nanoparticles as an intracellular MRI contrast agent. *JBIC J. Biol. Inorg. Chem.* **9,** 706–712 (2004).

93. Dobson, J. Gene therapy progress and prospects: magnetic nanoparticle-based gene delivery. *Gene Ther.* **13,** 283–287 (2006).

94. Johannsen, M. *et al.* Clinical hyperthermia of prostate cancer using magnetic nanoparticles: Presentation of a new interstitial technique. *Int. J. Hyperthermia* **21,** 637–647 (2005).

95. Ally, J., Martin, B., Behrad Khamesee, M., Roa, W. & Amirfazli, A. Magnetic targeting of aerosol particles for cancer therapy. *J. Magn. Magn. Mater.* **293,** 442–449 (2005).

96. Dames, P. *et al.* Targeted delivery of magnetic aerosol droplets to the lung. *Nat. Nanotechnol.* **2,** 495–499 (2007).

97. Mahmoudi, M., Serpooshan, V. & Laurent, S. Engineered nanoparticles for biomolecular imaging. *Nanoscale* **3,** 3007–3026 (2011).

98. Schenck, J. F. Safety of Strong, Static Magnetic Fields. *J. Magn. Reson. Imaging* **12,** 2–19 (2000).

99. Lübbe, A. S. *et al.* Clinical experiences with magnetic drug targeting: a phase I study with 4'-epidoxorubicin in 14 patients with advanced solid tumors. *Cancer Res.* **56,** 4686–4693 (1996).

100. Goodwin, S., Peterson, C., Hoh, C. & Bittner, C. Targeting and retention of magnetic targeted carriers (MTCs) enhancing intra-arterial chemotherapy. *J. Magn. Magn. Mater.* **194,** 132–139 (1999).

101. Grady, M. S. *et al.* Nonlinear magnetic stereotaxis: three-dimensional, in vivo remote magnetic manipulation of a small object in canine brain. *Med. Phys.* **17,** 405–415 (1990).

102. Ritter, R. C. *et al.* Open field system for magnetic surgery. (2001).

103. Bauernfeind, T. *et al.* The magnetic navigation system allows safety and high efficacy for ablation of arrhythmias. *Eur. Eur. Pacing Arrhythm. Card. Electrophysiol. J. Work. Groups Card. Pacing Arrhythm. Card. Cell. Electrophysiol. Eur. Soc. Cardiol.* **13,** 1015–1021 (2011).

104. Ciuti, G., Valdastri, P., Menciassi, A. & Dario, P. Robotic magnetic steering and locomotion of capsule endoscope for diagnostic and surgical endoluminal procedures. *Robotica* **28,** 199–207 (2010).

105. Yim, S. & Sitti, M. Design and analysis of a magnetically actuated and compliant capsule endoscopic robot. in *2011 IEEE International Conference on Robotics and Automation (ICRA)* 4810–4815 (2011). doi:10.1109/ICRA.2011.5979819

106. Ergeneman, O., Dogangil, G., Abbott, J. J., Nazeeruddin, M. K. & Nelson, B. J. A magnetically controlled wireless intraocular oxygen sensor: concept, prototype, and in vitro experiments. *Conf. Proc. Annu. Int. Conf. IEEE Eng. Med. Biol. Soc. IEEE Eng. Med. Biol. Soc. Annu. Conf.* **2007,** 4189–4193 (2007).

107. Mathieu, J.-B., Beaudoin, G. & Martel, S. Method of Propulsion of a Ferromagnetic Core in the Cardiovascular System Through Magnetic Gradients Generated by an MRI System. *IEEE Trans. Biomed. Eng.* **53,** 292–299 (2006).

108. Tamaz, S., Gourdeau, R., Chanu, A., Mathieu, J.-B. & Martel, S. Real-time MRI-based control of a ferromagnetic core for endovascular navigation. *IEEE Trans. Biomed. Eng.* **55,** 1854–1863 (2008).

109. Meeker, D. C., Maslen, E. H., Ritter, R. C. & Creighton, F. M. Optimal realization of arbitrary forces in a magnetic stereotaxis system. *IEEE Trans. Magn.* **32,** 320–328 (1996).

110. Kummer, M. P. *et al.* OctoMag: An Electromagnetic System for 5-DOF Wireless Micromanipulation. *IEEE Trans. Robot.* **26,** 1006–1017 (2010).

111. Belharet, K., Folio, D. & Ferreira, A. Three-Dimensional Controlled Motion of a Microrobot using Magnetic Gradients. *Adv. Robot.* **25,** 1069–1083 (2011).

112. Nacev, A., Beni, C., Bruno, O. & Shapiro, B. The Behaviors of Ferro-Magnetic Nano-Particles In and Around Blood Vessels under Applied Magnetic Fields. *J. Magn. Magn. Mater.* **323,** 651–668 (2011).

113. Park, J. Y. *et al.* Paramagnetic Ultrasmall Gadolinium Oxide Nanoparticles as Advanced T1 MRI Contrast Agent: Account for Large Longitudinal Relaxivity,

Optimal Particle Diameter, and In Vivo T1 MR Images. *ACS Nano* **3,** 3663–3669 (2009).

114. Kulkarni, S. *et al.* Quantifying the motion of magnetic particles in excised tissue: effect of particle properties and applied magnetic field. *J. Magn. Magn. Mater.* **393,** 243–252 (2015).
115. Weissleder, R. *et al.* In vivo magnetic resonance imaging of transgene expression. *Nat. Med.* **6,** 351–354 (2000).
116. Bonnemain, B. Superparamagnetic agents in magnetic resonance imaging: physicochemical characteristics and clinical applications. A review. *J. Drug Target.* **6,** 167–174 (1998).
117. Nacev, A., Beni, C., Bruno, O. & Shapiro, B. Magnetic Nanoparticle Transport within Flowing Blood and Into Surrounding Tissue. *Nanomed.* **5,** 1459–66 (2010).
118. Pankhurst, Q. A., Thanh, N. T. K., Jones, S. K. & Dobson, J. Progress in applications of magnetic nanoparticles in biomedicine. *J. Phys. Appl. Phys.* **42,** 224001 (2009).
119. Lubbe, A. S., Alexiou, C. & Bergemann, C. Clinical applications of magnetic drug targeting. *J. Surg. Res.* **95,** 200–206 (2001).
120. Shapiro, B. *et al.* Shaping Magnetic Fields to Direct Therapy to Ears and Eyes. *Annu. Rev. Biomed. Eng.* (2014). doi:10.1146/annurev-bioeng-071813-105206
121. Alexiou, C. *et al.* Targeting cancer cells: magnetic nanoparticles as drug carriers. *Eur. Biophys. J. Biophys. Lett.* **35,** 446–450 (2006).
122. Yigit, M. V., Moore, A. & Medarova, Z. Magnetic nanoparticles for cancer diagnosis and therapy. *Pharm. Res.* **29,** 1180–1188 (2012).
123. Brigger, I., Dubernet, C. & Couvreur, P. Nanoparticles in cancer therapy and diagnosis. *Adv Drug Deliv Rev* **54,** 631–651 (2002).
124. McCarthy, J. R. & Weissleder, R. Multifunctional magnetic nanoparticles for targeted imaging and therapy. *Adv. Drug Deliv. Rev.* **60,** 1241–1251 (2008).

125. Mornet, S., Vasseur, S., Grasset, F. & Duguet, E. Magnetic nanoparticle design for medical diagnosis and therapy. *J. Mater. Chem.* **14,** 2161–2175 (2004).

126. Lai, S. K. *et al.* Rapid transport of large polymeric nanoparticles in fresh undiluted human mucus. *Proc. Natl. Acad. Sci.* **104,** 1482–1487 (2007).

127. Kalambur, V. S., Han, B., Hammer, B. E., Shield, T. W. & Bischof, J. C. In vitro characterization of movement, heating and visualization of magnetic nanoparticles for biomedical applications. *Nanotechnology* **16,** 1221 (2005).

128. Allard, E., Passirani, C. & Benoit, J.-P. Convection-enhanced delivery of nanocarriers for the treatment of brain tumors. *Biomaterials* **30,** 2302–2318 (2009).

129. MacKay, J. A., Deen, D. F. & Szoka Jr., F. C. Distribution in brain of liposomes after convection enhanced delivery; modulation by particle charge, particle diameter, and presence of steric coating. *Brain Res.* **1035,** 139–153 (2005).

130. Thorne, R. G. & Nicholson, C. In vivo diffusion analysis with quantum dots and dextrans predicts the width of brain extracellular space. *Proc. Natl. Acad. Sci.* **103,** 5567–5572 (2006).

131. Nance, E. A. *et al.* A Dense Poly(Ethylene Glycol) Coating Improves Penetration of Large Polymeric Nanoparticles Within Brain Tissue. *Sci. Transl. Med.* **4,** 149ra119-149ra119 (2012).

132. Valberg, P. A. & Feldman, H. A. Magnetic particle motions within living cells. Measurement of cytoplasmic viscosity and motile activity. *Biophys. J.* **52,** 551–561 (1987).

133. Zhang, E. *et al.* Dynamic Magnetic Fields Remote-Control Apoptosis *via* Nanoparticle Rotation. *ACS Nano* **8,** 3192–3201 (2014).

134. Baroli, B. *et al.* Penetration of Metallic Nanoparticles in Human Full-Thickness Skin. *J Invest Dermatol* **127,** 1701–1712 (2007).

135. Pankhurst, Q. A., Connolly, J., Jones, S. K. & Dobson, J. Applications of magnetic nanoparticles in biomedicine. *J. Phys. Appl. Phys.* **36,** R167 (2003).

136. Domínguez-García, P., Melle, S., Pastor, J. M. & Rubio, M. A. Scaling in the aggregation dynamics of a magnetorheological fluid. *Phys. Rev. E* **76,** 51403 (2007).

137. Sano, K. & Doi, M. Theory of agglomeration of ferromagnetic particles in magnetic fluids. *J PHYS SOC Jpn.* **52,** 2810–2815 (1983).

138. Taketomi, S., Takahashi, H., Inaba, N. & Miyajima, H. Experimental and theoretical investigations on agglomeration of magnetic colloidal particles in magnetic fluids. *J Phys Soc Jpn* **60,** 1689–1707 (1991).

139. Saltzman, W. M. *Drug Delivery: Engineering Principles for Drug Therapy*. (Oxford University Press, 2001).

140. Bausch, A. R., Ziemann, F., Boulbitch, A. A., Jacobson, K. & Sackmann, E. Local Measurements of Viscoelastic Parameters of Adherent Cell Surfaces by Magnetic Bead Microrheometry. *Biophys. J.* **75,** 2038–2049 (1998).

141. Valberg, P. A. & Albertini, D. F. Cytoplasmic motions, rheology, and structure probed by a novel magnetic particle method. *J. Cell Biol.* **101,** 130–140 (1985).

142. Renkin, E. M. Filtration, diffusion, and molecular sieving through porous cellulose membranes. *J. Gen. Physiol.* **38,** 225–243 (1954).

143. Ogston, A. G., Preston, B. N. & Wells, J. D. On the transport of compact particles through solutions of chain-polymers. *Proc. R. Soc. Lond. Math. Phys. Sci.* **333,** 297 (1973).

144. Nacev, A. *et al.* A dynamic magnetic shift method to increase nanoparticle concentration in cancer metastases: a feasibility study using simulations on autopsy specimens. *Int. J. Nanomedicine* **6,** 2907–2923 (2011).

145. Fung, Y.-C. *Biomechanics*. (Springer New York, 1993).

146. Ikada, Y. *Tissue Engineering: Fundamentals and Applications*. (Academic Press, 2011).

147. Teicher, B. A. In Vivo/Ex Vivo and In Situ Assays Used in Cancer Research: A Brief Review. *Toxicol. Pathol.* **37,** 114–122 (2009).

148. Zhaolong Shen *et al.* Automated Fluorescence and Reflectance Coregistered 3-D Tissue Imaging System. *Magn. IEEE Trans. On* **49,** 279–284 (2013).

149. Fleisch, D. A. *A Student's Guide to Maxwell's Equations*. (Cambridge University Press, 2008).

150. Forbes, Z. G., Yellen, B. B., Barbee, K. A. & Friedman, G. An approach to targeted drug delivery based on uniform magnetic fields. *IEEE Trans. Magn.* **39,** 3372–3377 (2003).

151. Jackson, J. D. *Classical Electrodynamics Third Edition*. (Wiley, 1998).

152. Feynman, R. P. *Feynman lectures on physics.* (Addison Wesley Longman, 1970).

153. Mikkelsen, C. I. Magnetic separation and hydrodynamic interactions in microfluidic systems. (Technical University of Denmark, 2005).

154. Foner, S. Versatile and Sensitive Vibrating #x2010;Sample Magnetometer. *Rev. Sci. Instrum.* **30,** 548–557 (1959).

155. Murdock, R. C., Braydich-Stolle, L., Schrand, A. M., Schlager, J. J. & Hussain, S. M. Characterization of Nanomaterial Dispersion in Solution Prior to In Vitro Exposure Using Dynamic Light Scattering Technique. *Toxicol. Sci.* **101,** 239–253 (2008).

156. Seliger, C. *et al.* In vitro investigation of the behaviour of magnetic particles by a circulating artery model. *J. Magn. Magn. Mater.* **311,** 358–362 (2007).

157. Bootz, A., Vogel, V., Schubert, D. & Kreuter, J. Comparison of scanning electron microscopy, dynamic light scattering and analytical ultracentrifugation for the sizing of poly(butyl cyanoacrylate) nanoparticles. *Eur. J. Pharm. Biopharm.* **57,** 369–375 (2004).

158. Sennett, P. & Olivier, J. P. COLLOIDAL DISPERSIONS, ELECTROKINETIC EFFECTS, AND THE CONCEPT OF ZETA POTENTIAL. *Ind. Eng. Chem.* **57,** 32–50 (1965).

159. Zhang, Y. *et al.* Zeta potential: a surface electrical characteristic to probe the interaction of nanoparticles with normal and cancer human breast epithelial cells. *Biomed. Microdevices* **10,** 321–328 (2007).

160. Verwey, E. J. W., Overbeek, J. T. G. & Overbeek, J. T. G. *Theory of the Stability of Lyophobic Colloids*. (Courier Dover Publications, 1999).

161. Samani, A. & Plewes, D. A method to measure the hyperelastic parameters of ex vivo breast tissue samples. *Phys. Med. Biol.* **49,** 4395 (2004).

162. Fo, B., Nr, G., Hw, S., Rm, H. & Jh, S. A new perfusate for kidney preservation. *Transplantation* **33,** 322–323 (1982).

163. Collins, G. M., Bravo-Shugarman, M. & Terasaki, P. I. KIDNEY PRESERVATION FOR TRANSPORTATION. *The Lancet* **294,** 1219–1222 (1969).

164. Ramaswamy, B. *et al.* Movement of magnetic nanoparticles in brain tissue: mechanisms and impact on normal neuronal function. *Nanomedicine Nanotechnol. Biol. Med.* **11,** 1821–1829 (2015).

165. Woodworth, G. F., Dunn, G. P., Nance, E. A., Hanes, J. & Brem, H. Emerging Insights into Barriers to Effective Brain Tumor Therapeutics. *Front. Oncol.* **4,** (2014).

166. DANDY WE. Removal of right cerebral hemisphere for certain tumors with hemiplegia: Preliminary report. *J. Am. Med. Assoc.* **90,** 823–825 (1928).

167. Matsukado, Y., Maccarty, C. S. & Kernohan, J. W. The growth of glioblastoma multiforme (astrocytomas, grades 3 and 4) in neurosurgical practice. *J. Neurosurg.* **18,** 636–644 (1961).

168. Kaiser, M. G. *et al.* Tissue distribution and antitumor activity of topotecan delivered by intracerebral clysis in a rat glioma model. *Neurosurgery* **47,** 1391-1398-1399 (2000).

169. Brem, H. *et al.* Placebo-controlled trial of safety and efficacy of intraoperative controlled delivery by biodegradable polymers of chemotherapy for recurrent gliomas. The Polymer-brain Tumor Treatment Group. *Lancet* **345,** 1008–1012 (1995).

170. Stupp, R. *et al.* Radiotherapy plus Concomitant and Adjuvant Temozolomide for Glioblastoma. *N. Engl. J. Med.* **352,** 987–996 (2005).

171. Chinot, O. L. *et al.* Bevacizumab plus Radiotherapy–Temozolomide for Newly Diagnosed Glioblastoma. *N. Engl. J. Med.* **370,** 709–722 (2014).

172. Hassan, E. E. & Gallo, J. M. Targeting Anticancer Drugs to the Brain. I: Enhanced Brain Delivery of Oxantrazole following Administration in Magnetic Cationic Microspheres. *J. Drug Target.* **1,** 7–14 (1993).

173. Lockman, P. R., Mumper, R. J., Khan, M. A. & Allen, D. D. Nanoparticle Technology for Drug Delivery Across the Blood-Brain Barrier. *Drug Dev. Ind. Pharm.* **28,** 1–13 (2002).

174. del Burgo, L. S., Hernández, R. M., Orive, G. & Pedraz, J. L. Nanotherapeutic approaches for brain cancer management. *Nanomedicine Nanotechnol. Biol. Med.* **10,** 905–919 (2014).

175. Maier-Hauff, K. *et al.* Intracranial Thermotherapy using Magnetic Nanoparticles Combined with External Beam Radiotherapy: Results of a Feasibility Study on Patients with Glioblastoma Multiforme. *J. Neurooncol.* **81,** 53–60 (2007).

176. van Landeghem, F. K. H. *et al.* Post-mortem studies in glioblastoma patients treated with thermotherapy using magnetic nanoparticles. *Biomaterials* **30,** 52–57 (2009).

177. Sensenig, R., Sapir, Y., MacDonald, C., Cohen, S. & Polyak, B. Magnetic nanoparticle-based approaches to locally target therapy and enhance tissue regeneration in vivo. *Nanomed.* **7,** 1425–1442 (2012).

178. Carenza, E. *et al.* In vitro angiogenic performance and in vivo brain targeting of magnetized endothelial progenitor cells for neurorepair therapies. *Nanomedicine Nanotechnol. Biol. Med.* **10,** 225–234 (2014).

179. Zhan, C. *et al.* Micelle-Based Brain-Targeted Drug Delivery Enabled by a Nicotine Acetylcholine Receptor Ligand. *Angew. Chem. Int. Ed.* **50,** 5482–5485 (2011).

180. Feng, B. *et al.* Delivery of sodium borocaptate to glioma cells using immunoliposome conjugated with anti-EGFR antibodies by ZZ-His. *Biomaterials* **30,** 1746–1755 (2009).

181. Wu, X.-X. *et al.* Doxorubicin enhances TRAIL-induced apoptosis in prostate cancer. *Int. J. Oncol.* **20,** 949–954 (2002).

182. Yang, C. *et al.* Nanoimmunoliposome delivery of superparamagnetic iron oxide markedly enhances targeting and uptake in human cancer cells in vitro and in vivo. *Nanomedicine Nanotechnol. Biol. Med.* **4,** 318–329 (2008).

183. Nacev, A., Beni, C., Bruno, O. & Shapiro, B. Magnetic nanoparticle transport within flowing blood and into surrounding tissue. *Nanomed.* **5,** 1459–1466 (2010).

184. Huynh, N. T. *et al.* Treatment of 9L gliosarcoma in rats by ferrociphenol-loaded lipid nanocapsules based on a passive targeting strategy via the EPR effect. *Pharm. Res.* **28,** 3189–3198 (2011).

185. Salcedo, E. *et al.* Activity-dependent changes in cholinergic innervation of the mouse olfactory bulb. *PloS One* **6,** e25441 (2011).

186. Erb, R. M. Magnetic Manipulation and Assembly of Multi-component Particle Suspensions. (Duke University, 2009).

187. Hamill, O. P., Marty, A., Neher, E., Sakmann, B. & Sigworth, F. J. Improved patch-clamp techniques for high-resolution current recording from cells and cell-free membrane patches. *Pflüg. Arch.* **391,** 85–100 (1981).

188. Galarreta, M. & Hestrin, S. A network of fast-spiking cells in the neocortex connected by electrical synapses. *Nature* **402,** 72–75 (1999).

189. Sakmann, B. & Neher, E. *Single-channel recording*. (Springer New York, 2009).

190. Zimnik, N. C., Treadway, T., Smith, R. S. & Araneda, R. C. α(1A)-Adrenergic regulation of inhibition in the olfactory bulb. *J. Physiol.* **591,** 1631–1643 (2013).

191. Shipley, M. T. & Ennis, M. Functional organization of olfactory system. *J. Neurobiol.* **30,** 123–176 (1996).

192. Rye, D. B., Wainer, B. H., Mesulam, M.-M., Mufson, E. J. & Saper, C. B. Cortical projections arising from the basal forebrain: A study of cholinergic and noncholinergic components employing combined retrograde tracing and immunohistochemical localization of choline acetyltransferase. *Neuroscience* **13,** 627–643 (1984).

193. Richter, H. *et al.* Magnetorelaxometric quantification of magnetic nanoparticles in an artery model after ex vivo magnetic drug targeting. *Phys. Med. Biol.* **54,** N417 (2009).

194. Wang, H. *et al.* Smart multifunctional core–shell nanospheres with drug and gene co-loaded for enhancing the therapeutic effect in a rat intracranial tumor model. *Nanoscale* **4,** 6501 (2012).

195. Ang, D. *et al.* Insights into the mechanism of magnetic particle assisted gene delivery. *Acta Biomater.* **7,** 1319–1326 (2011).

196. Jones, G. A. & Niedoba, H. IMP-Field induced agglomeration in thin films of aqueous based magnetic fluids. *J. Magn. Magn. Mater.* **73,** 33–38 (1988).

197. Domínguez-García, P., Melle, S., Pastor, J. M. & Rubio, M. A. Scaling in the aggregation dynamics of a magnetorheological fluid. *Phys. Rev. E* **76,** 51403 (2007).

198. Helgesen, G., Skjeltorp, A. T., Mors, P. M., Botet, R. & Jullien, R. Aggregation of Magnetic Microspheres: Experiments and Simulations. *Phys. Rev. Lett.* **61,** 1736–1739 (1988).

199. Černák, J., Helgesen, G. & Skjeltorp, A. T. Aggregation dynamics of nonmagnetic particles in a ferrofluid. *Phys. Rev. E* **70,** 31504 (2004).

200. Vicsek, T. & Family, F. Dynamic Scaling for Aggregation of Clusters. *Phys. Rev. Lett.* **52,** 1669–1672 (1984).

201. Witten, T. A. & Sander, L. M. Diffusion-Limited Aggregation, a Kinetic Critical Phenomenon. *Phys. Rev. Lett.* **47,** 1400–1403 (1981).

202. Miyazima, S., Meakin, P. & Family, F. Aggregation of oriented anisotropic particles. *Phys. Rev. A* **36,** 1421–1427 (1987).

203. Erb, R. M., Sebba, D. S., Lazarides, A. A. & Yellen, B. B. Magnetic field induced concentration gradients in magnetic nanoparticle suspensions: Theory and experiment. *J. Appl. Phys.* **103,** 63916-63916–5 (2008).

204. Vartholomeos, P. & Mavroidis, C. In Silico Studies of Magnetic Microparticle Aggregations in Fluid Environments for MRI-Guided Drug Delivery. *IEEE Trans. Biomed. Eng.* **59,** 3028–3038 (2012).

205. Socoliuc, V., Bica, D. & Vekas, L. Estimation of magnetic particle clustering in magnetic fluids from static magnetization experiments. *J. Colloid Interface Sci.* **264,** 141–147 (2003).

206. Kim, J. S. *et al.* Toxicity and Tissue Distribution of Magnetic Nanoparticles in Mice. *Toxicol. Sci.* **89,** 338–347 (2006).

207. Talelli, M. *et al.* Intrinsically active nanobody-modified polymeric micelles for tumor-targeted combination therapy. *Biomaterials* **34,** 1255–1260 (2013).

208. Alexiou, C. *et al.* Locoregional Cancer Treatment with Magnetic Drug Targeting. *Cancer Res.* **60,** 6641–6648 (2000).

209. Nacev, A. *et al.* Towards Control of Magnetic Fluids in Patients: Directing Therapeutic Nanoparticles to Disease Locations. *IEEE Control Syst.* **32,** 32–74 (2012).

210. Probst, R. *et al.* Planar Steering of a Single Ferrofluid Drop by Optimal Minimum Power Dynamic Feedback Control of Four Electromagnets at a Distance. *J. Magn. Magn. Mater.* **323,** 885–896 (2011).

211. Miller, R. P., Tadagavadi, R. K., Ramesh, G. & Reeves, W. B. Mechanisms of Cisplatin Nephrotoxicity. *Toxins* **2,** 2490–2518 (2010).

212. Rademaker-Lakhai, J. M. *et al.* Relationship between cisplatin administration and the development of ototoxicity. *J. Clin. Oncol. Off. J. Am. Soc. Clin. Oncol.* **24,** 918–924 (2006).

213. Gregg, R. W. *et al.* Cisplatin neurotoxicity: the relationship between dosage, time, and platinum concentration in neurologic tissues, and morphologic evidence of toxicity. *J. Clin. Oncol. Off. J. Am. Soc. Clin. Oncol.* **10,** 795–803 (1992).

214. Marshak, T., Steiner, M., Kaminer, M., Levy, L. & Shupak, A. Prevention of Cisplatin-Induced Hearing Loss by Intratympanic Dexamethasone: A Randomized Controlled Study. *Otolaryngol.--Head Neck Surg. Off. J. Am. Acad. Otolaryngol.-Head Neck Surg.* **150,** 983–990 (2014).

215. Allen, G. C. *et al.* Transient-Evoked Otoacoustic Emissions in Children after Cisplatin Chemotherapy. *Otolaryngol. -- Head Neck Surg.* **118,** 584–588 (1998).

216. Rybak, L. P., Mukherjea, D., Jajoo, S. & Ramkumar, V. Cisplatin ototoxicity and protection: clinical and experimental studies. *Tohoku J. Exp. Med.* **219,** 177–186 (2009).

217. DeWoskin, R. S. & Riviere, J. E. Cisplatin-induced loss of kidney copper and nephrotoxicity is ameliorated by single dose diethyldithiocarbamate, but not mesna. *Toxicol. Appl. Pharmacol.* **112,** 182–189 (1992).

218. Monzack, E. L., May, L. A., Roy, S., Gale, J. E. & Cunningham, L. L. Live imaging the phagocytic activity of inner ear supporting cells in response to hair cell death. *Cell Death Differ.* (2015). doi:10.1038/cdd.2015.48

219. Lee, J. E. *et al.* Mechanisms of apoptosis induced by cisplatin in marginal cells in mouse stria vascularis. *ORL J. Oto-Rhino-Laryngol. Its Relat. Spec.* **66,** 111–118 (2004).

220. Himeno, C. *et al.* Intra-cochlear administration of dexamethasone attenuates aminoglycoside ototoxicity in the guinea pig. *Hear. Res.* **167,** 61–70 (2002).

221. Wooldridge, J. E., Anderson, C. M. & Perry, M. C. Corticosteroids in advanced cancer. *Oncol. Williston Park N* **15,** 225-234-236 (2001).

222. Ranganath, P. *et al.* Management of Chemotherapy Induced Nausea and Vomiting in Patients on Multiday Cisplatin Based Combination Chemotherapy, Management of Chemotherapy Induced Nausea and Vomiting in Patients on Multiday Cisplatin Based Combination Chemotherapy. *BioMed Res. Int. BioMed Res. Int.* **2015, 2015,** e943618 (2015).

223. Morin, C. & Fardet, L. Systemic glucocorticoid therapy: risk factors for reported adverse events and beliefs about the drug. A cross-sectional online survey of 820 patients. *Clin. Rheumatol.* **34,** 2119–2126 (2015).

224. Fardet, L. & Fève, B. Systemic Glucocorticoid Therapy: a Review of its Metabolic and Cardiovascular Adverse Events. *Drugs* **74,** 1731–1745 (2014).

225. Bird, P. A. *et al.* Intratympanic versus intravenous delivery of methylprednisolone to cochlear perilymph. *Otol. Neurotol. Off. Publ. Am. Otol. Soc. Am. Neurotol. Soc. Eur. Acad. Otol. Neurotol.* **28,** 1124–1130 (2007).

226. Shapiro, B. *et al.* Shaping Magnetic Fields to Direct Therapy to Ears and Eyes. *Annu. Rev. Biomed. Eng.* **16,** 455–481 (2014).

227. Shapiro, B. *et al.* Pre-Clinical Development of Magnetic Delivery of Therapy to Middle and Inner Ears. *ENT & Audiology News* 54–56 (2014).

228. Özel, H. E. *et al.* Comparison of the protective effects of intratympanic dexamethasone and methylprednisolone against cisplatin-induced ototoxicity. *J. Laryngol. Otol.* **130,** 225–234 (2016).

229. Roy, S., Ryals, M. M., Van den Bruele, A. B., Fitzgerald, T. S. & Cunningham, L. L. Sound preconditioning therapy inhibits ototoxic hearing loss in mice. *J. Clin. Invest.* **123,** 4945–4949 (2013).

230. Chirtes, F. & Albu, S. Prevention and restoration of hearing loss associated with the use of cisplatin. *BioMed Res. Int.* **2014,** 925485 (2014).

231. Boulikas, T. & Vougiouka, M. Cisplatin and platinum drugs at the molecular level (Review). *Oncol. Rep.* (2003). doi:10.3892/or.10.6.1663

232. Okano, T. Immune system of the inner ear as a novel therapeutic target for sensorineural hearing loss. *Front. Pharmacol.* **5,** 205 (2014).

233. Zhang, C. *et al.* Corticosteroids induce chemotherapy resistance in the majority of tumour cells from bone, brain, breast, cervix, melanoma and neuroblastoma. *Int. J. Oncol.* (2006). doi:10.3892/ijo.29.5.1295

234. Herr, I. *et al.* Glucocorticoid cotreatment induces apoptosis resistance toward cancer therapy in carcinomas. *Cancer Res.* **63,** 3112–3120 (2003).

235. Ramaswamy, B. *et al.* Wireless current sensing by near field induction from a spin transfer torque nano-oscillator. *Appl. Phys. Lett.* **108,** 242403 (2016).

236. Ziegler, S., Woodward, R. C., Iu, H. H.-C. & Borle, L. J. Current Sensing Techniques: A Review. *IEEE Sens. J.* **9,** 354–376 (2009).

237. Feltham, D. B. I., Nigh, P. J., Carley, L. R. & Maly, W. Current sensing for built-in testing of CMOS circuits. in *, Proceedings of the 1988 IEEE International Conference on Computer Design: VLSI in Computers and Processors, 1988. ICCD '88* 454–457 (1988). doi:10.1109/ICCD.1988.25742

238. Akira Todorokj, H. K. & Matsuura, K. Application of electric potential method to smart composite structures for detecting delamination. in *Proceedings of the Tenth International Conference on Composite Materials: Structures* **5,** 323 (Woodhead Publishing, 1995).

239. Kong, J. *et al.* Nanotube molecular wires as chemical sensors. *Science* **287,** 622–625 (2000).

240. Buzsáki, G., Anastassiou, C. A. & Koch, C. The origin of extracellular fields and currents — EEG, ECoG, LFP and spikes. *Nat. Rev. Neurosci.* **13,** 407–420 (2012).

241. Heeger, D. J. & Ress, D. What does fMRI tell us about neuronal activity? *Nat. Rev. Neurosci.* **3,** 142–151 (2002).

242. Cassará, A. M., Maraviglia, B., Hartwig, S., Trahms, L. & Burghoff, M. Neuronal current detection with low-field magnetic resonance: simulations and methods. *Magn. Reson. Imaging* **27,** 1131–1139 (2009).

243. Lenz, J. & Edelstein, A. S. Magnetic sensors and their applications. *IEEE Sens. J.* **6,** 631–649 (2006).

244. Nakayama, S. & Uchiyama, T. Real-time measurement of biomagnetic vector fields in functional syncytium using amorphous metal. *Sci. Rep.* **5,** 8837 (2015).

245. Taylor, J. M. *et al.* High-sensitivity diamond magnetometer with nanoscale resolution. *Nat. Phys.* **4,** 810–816 (2008).

246. Balasubramanian, G. *et al.* Nanoscale imaging magnetometry with diamond spins under ambient conditions. *Nature* **455,** 648–651 (2008).

247. Chemla, S. & Chavane, F. Voltage-sensitive dye imaging: Technique review and models. *J. Physiol.-Paris* **104,** 40–50 (2010).

248. Rippard, W. H., Pufall, M. R., Kaka, S., Russek, S. E. & Silva, T. J. Direct-current induced dynamics in Co90Fe10/Ni80Fe20 point contacts. *Phys. Rev. Lett.* **92,** 027201.1-027201.4 (2004).

249. Deac, A. M. *et al.* Bias-driven high-power microwave emission from MgO-based tunnel magnetoresistance devices. *Nat. Phys.* **4,** 803–809 (2008).

250. Kiselev, S. I. *et al.* Microwave oscillations of a nanomagnet driven by a spin-polarized current. *Nature* **425,** 380–383 (2003).

251. Houssameddine, D. *et al.* Spin transfer induced coherent microwave emission with large power from nanoscale MgO tunnel junctions. *Appl. Phys. Lett.* **93,** 22505 (2008).

252. Zhou, Y., Zha, C. L., Bonetti, S., Persson, J. & Åkerman, J. Spin-torque oscillator with tilted fixed layer magnetization. *Appl. Phys. Lett.* **92,** 262508 (2008).

253. Zeng, Z. *et al.* Ultralow-current-density and bias-field-free spin-transfer nano-oscillator. *Sci. Rep.* **3,** 1426 (2013).

254. Slavin, A. & Tiberkevich, V. Nonlinear Auto-Oscillator Theory of Microwave Generation by Spin-Polarized Current. *IEEE Trans. Magn.* **45,** 1875–1918 (2009).

255. Amin, N., Xi, H. & Tang, M. X. Analysis of Electromagnetic Fields Generated by a Spin-Torque Oscillator. *IEEE Trans. Magn.* **45,** 4183–4186 (2009).

256. Prokopenko, O., Bankowski, E., Meitzler, T., Tiberkevich, V. & Slavin, A. Spin-Torque Nano-Oscillator as a Microwave Signal Source. *IEEE Magn. Lett.* **2,** 3000104–3000104 (2011).

257. Choi, H. S. *et al.* Spin nano-oscillator-based wireless communication. *Sci. Rep.* **4,** 5486 (2014).

258. Oh, I., Park, S., Kang, D.-H. & Park, C. S. Wireless Spintronics Modulation With a Spin Torque Nano-Oscillator (STNO) Array. *IEEE Microw. Wirel. Compon. Lett.* **24,** 502–504 (2014).

259. Muduli, P. K., Heinonen, O. G. & Åkerman, J. Bias dependence of perpendicular spin torque and of free- and fixed-layer eigenmodes in MgO-based nanopillars. *Phys. Rev. B* **83,** 184410 (2011).

260. Butler, W. H., Zhang, X.-G., Schulthess, T. C. & MacLaren, J. M. Spin-dependent tunneling conductance of Fe|MgO|Fe sandwiches. *Phys. Rev. B* **63,** 54416 (2001).

261. Ikeda, S. *et al.* A perpendicular-anisotropy CoFeB–MgO magnetic tunnel junction. *Nat. Mater.* **9,** 721–724 (2010).

262. Georges, B. *et al.* Origin of the spectral linewidth in nonlinear spin-transfer oscillators based on MgO tunnel junctions. *Phys. Rev. B* **80,** 60404 (2009).

263. Zeng, Z. *et al.* High-Power Coherent Microwave Emission from Magnetic Tunnel Junction Nano-oscillators with Perpendicular Anisotropy. *ACS Nano* **6,** 6115–6121 (2012).

264. Pozar, D. M. *Microwave Engineering, 4th Edition*. (Wiley Global Education, 2011).

265. Brown, R. W., Cheng, Y.-C. N., Haacke, E. M., Thompson, M. R. & Venkatesan, R. *Magnetic resonance imaging: physical principles and sequence design*. (John Wiley & Sons, 2014).

266. Zhu, J. *et al.* Voltage-Induced Ferromagnetic Resonance in Magnetic Tunnel Junctions. *Phys. Rev. Lett.* **108,** 197203 (2012).

267. Cheng, X., Boone, C. T., Zhu, J. & Krivorotov, I. N. Nonadiabatic Stochastic Resonance of a Nanomagnet Excited by Spin Torque. *Phys. Rev. Lett.* **105,** 47202 (2010).

268. Cheng, X., Katine, J. A., Rowlands, G. E. & Krivorotov, I. N. Nonlinear ferromagnetic resonance induced by spin torque in nanoscale magnetic tunnel junctions. *Appl. Phys. Lett.* **103,** 82402 (2013).

269. Maehara, H. *et al.* Large Emission Power over 2 μW with High *Q* Factor Obtained from Nanocontact Magnetic-Tunnel-Junction-Based Spin Torque Oscillator. *Appl. Phys. Express* **6,** 113005 (2013).

270. Rowlands, G. E. & Krivorotov, I. N. Magnetization dynamics in a dual free-layer spin-torque nano-oscillator. *Phys. Rev. B* **86,** 94425 (2012).

271. Yang, L. *et al.* Reduction of phase noise in nanowire spin orbit torque oscillators. *Sci. Rep.* **5,** 16942 (2015).

272. Kaka, S. *et al.* Mutual phase-locking of microwave spin torque nano-oscillators. *Nature* **437,** 389–392 (2005).

273. Tamaru, S., Kubota, H., Yakushiji, K., Yuasa, S. & Fukushima, A. Extremely Coherent Microwave Emission from Spin Torque Oscillator Stabilized by Phase Locked Loop. *Sci. Rep.* **5,** 18134 (2015).

274. Zhou, Y., Persson, J., Bonetti, S. & Åkerman, J. Tunable intrinsic phase of a spin torque oscillator. *Appl. Phys. Lett.* **92,** 92505 (2008).

275. Duan, Z. *et al.* Nanowire Spin Torque Oscillator Driven by Spin Orbit Torques. *Nat. Commun.* **5,** 5616 (2014).

276. Herberholz, J., Antonsen, B. L. & Edwards, D. H. A lateral excitatory network in the escape circuit of crayfish. *J. Neurosci. Off. J. Soc. Neurosci.* **22,** 9078–9085 (2002).

277. Ishibashi, S. *et al.* Large Diode Sensitivity of CoFeB/MgO/CoFeB Magnetic Tunnel Junctions. *Appl. Phys. Express* **3,** 73001 (2010).

278. Ladan, S. & Wu, K. High efficiency low-power microwave rectifier for wireless energy harvesting. in *Microwave Symposium Digest (IMS), 2013 IEEE MTT-S International* 1–4 (2013). doi:10.1109/MWSYM.2013.6697649

279. Cho, S. H., Cauller, L., Rosellini, W. & Lee, J. B. A MEMS-based fully-integrated wireless neurostimulator. in *2010 IEEE 23rd International Conference on Micro Electro Mechanical Systems (MEMS)* 300–303 (2010). doi:10.1109/MEMSYS.2010.5442507

280. Shire, D. B. *et al.* Development and Implantation of a Minimally Invasive Wireless Subretinal Neurostimulator. *IEEE Trans. Biomed. Eng.* **56,** 2502–2511 (2009).

281. Li, W. *et al.* Parylene-based integrated wireless single-channel neurostimulator. *Sens. Actuators Phys.* **166,** 193–200 (2011).

282. Georges, B. *et al.* Coupling Efficiency for Phase Locking of a Spin Transfer Nano-Oscillator to a Microwave Current. *Phys. Rev. Lett.* **101,** 17201 (2008).